The Design of Three-Dimensional Multicellular Liver Models Using Detachable, Nanoscale Polyelectrolyte Multilayers

Adam L. Larkin

Dissertation Submitted to the faculty of the Virginia Polytechnic Institute and State University in partial fulfillment of the requirements for the degree of

Doctor of Philosophy
in
Chemical Engineering

Padmavathy Rajagopalan, Co-Chair
Richey M. Davis, Co-chair
Eva Marand
Yong W. Lee

August 29, 2012
Blacksburg, VA

Keywords: polyelectrolyte multilayers, free-standing, liver mimic, multicellular

ABSTRACT

We report the design and assembly of three-dimensional (3D) multi-cellular liver models comprised of primary rat hepatocytes, liver sinusoidal endothelial cells (LSECs), and Kupffer cells (KCs). LSECs and KCs in the liver model were separated from hepatocytes by a nanoscale, detachable, optically transparent chitosan and hyaluronic acid (HA) polyelectrolyte multilayer (PEM) film. The properties of the PEM were tuned to mimic the Space of Disse found in liver. The thickness of the detachable PEM was 650 to 1000 nm under hydrated conditions. The Young's modulus of the PEM was approximately 42 kPa, well within the range of modulus values reported for bulk liver. The 3D liver models comprised of all three cell types and a detachable PEM exhibited stable urea production and increased albumin secretion over a 12 day culture period. Additionally, the 3D liver model maintained the phenotype of both LSECs and KCs over the 12 day culture period, verified by CD32b and CD163 staining, respectively. Additionally, CYP1A1 enzyme activity increased significantly in the 3D liver models. The number of hepatocytes in the 3D liver model increased by approximately 60% on day 16 of culture compared to day 4 indicating. Furthermore, only the 3D hepatic model maintained cellular compositions virtually identical to those found *in vivo*. DNA microarray measurements were conducted on the hepatocyte fractions of the 3D liver mimic to obtain insights into hepatic processes. Gene sets up-regulated in the 3D liver model were related to proliferation, migration, and deposition of extracellular matrix, all functions observed in regenerating hepatocytes. Taken together, these results suggest that inter-cellular signaling between the different cell types in the 3D liver model led to increased hepatic functions. To the best of our knowledge, this is the first study where three of the major hepatic cell types have been incorporated into a model that closely mimics the structure of the sinusoid. These studies demonstrate that the multi-cellular liver models are physiologically relevant. Such models are very promising to conduct detailed investigations into hepatic inter-cellular signaling.

ACKNOWLEDGEMENTS

I would like to thank my advisor, Dr. Padma Rajagopalan, for her great guidance throughout my graduate research career and her support for me to grow as an independent researcher. I am grateful for her patience and willingness to teach, lead, and listen throughout my four years at Virginia Tech. Additionally, her endless support of my research provided me opportunities to showcase research at national conferences on an annual basis. Without her support, the following research projects and goals could not have been accomplished. I am also very grateful to my co-advisor Dr. Richey M. Davis for his critical input and help with polyelectrolyte multilayers, their assembly, and their characterization. I would like to thank Dr. T. M. Murali for his invaluable help and assistance in the field of computational biology and analysis. I also thank Dr. Eva Marand and Dr. Yong Woo Lee for their valuable time and critical analysis of my research as well as their service on my graduate committee.

I am grateful to current and past graduate students and labmates Dr. Yeonhee Kim, Dr. Era Jain, Gaurav Jain, Richard Rodrigues, Brandon Veres, Lucas Vu, Cigdem Arca, Adedayo Adeniran, and Nathan Hale for their help and support inside and outside of the lab. Their friendship and hard work has been both inspiring and motivating for me. I would like to specially thank Dr. Yeonhee Kim for giving me the opportunity in Chapter 2 to work on her project. I would also like to thank Richard Rodrigues for taking time to perform the computational analysis reported in Chapter 4. I would also like to thank Reisha Parham for her assistance in designing detachable PEMs in Chapters 3 and 4. Additionally, I would like to thank the undergraduate students who have helped me throughout my research, Reisha Parham, Aruna Nagarajan, Karan Singh, and Ann-Marie Callsen.

I would like to thank my family for their love, support, and encouragement for me to pursue my dreams. Most importantly, I am forever indebted to my wife, Lindsay Larkin, for her unconditional love and support every day. Without out her positive attitude and undying support, none of this would have been possible.

I gratefully acknowledge the financial support provided by the National Institutes of Health, the National Science Foundation, and the Institute for Critical Technology and Science at Virginia Tech.

Table of Contents

Chapter 1. Introduction and Background

List of Figures

List of Tables

Chapter 1. INTRODUCTION AND BACKGROUND

1.1 INTRODUCTION TO THE LIVER

1.1.1 Liver Organization, Function and Structure

The liver is one of the largest and most important organs in the human body. It carries out a multitude of essential functions such as carbohydrate, lipid, and amino acid metabolism, plasma and protein biosynthesis, biotransformation of xenobiotics, drugs and toxins, and bile production. The liver is also capable of regeneration even when 70% of its mass has been removed (1). The liver stores excess glycogen, which can be converted to glucose for additional energy (2, 3). In addition to the synthesis of lipoproteins, the liver also plays an important role in cholesterol, steroid and fat-soluble vitamin metabolism (2, 3). Several plasma proteins such as albumin, globulin, fibrinogen, and prothrombin are synthesized in the liver (2, 3). In addition to deamination of amino acids, the liver can convert them into non-toxic urea (2). It is responsible for the metabolism of xenobiotics, drugs and toxins (2, 3). The liver also produces and secretes bile, which is necessary for the metabolism of cholesterol and the emulsification of fats (2, 3). Bilirubin, a product of aged erythrocytes, is excreted into the bile canaliculi along with bile secreted by hepatocytes and then carried out of the liver to the small intestine (2, 4). Bilirubin has been implicated in various diseases such as jaundice when it is produced at a concentration greater than what the liver can excrete (2, 4).

The microcirculatory unit of the liver, termed acinus, extends from the terminal portal venule and hepatic arteriole, delivering blood into the sinusoids and then to the central and hepatic veins (**Figure 1.1**) (5-8). The liver sinusoid is the microvasculature that delivers oxygen-rich blood to the parenchyma and non-parenchyma of the liver (2, 4). In the liver, zonation is characterized by the oxygen tension along the liver sinusoids from the portal vein (pO_2 = 60 – 70 mm Hg) to the central vein (pO_2 = 30 – 35 mm Hg) (5-8). The region around the terminal portal vein is called the periportal zone and the area around the central vein is known as the pericentral zone (5-8). Due to the oxygen tension between the periportal and pericentral zone, the changes in oxygen partial pressure create

differences in hepatic functions such as the asymmetric distribution of key enzymes of various metabolic pathways (5-8). For example, the capacity for energy metabolism, glucose formation, urea production, plasma protein biosynthesis, and bile formation is greater in the periportal region (higher pO_2) while glucose uptake, glutamine formation, and xenobiotic metabolism is higher in the pericentral region (lower pO_2) (5, 6, 8).

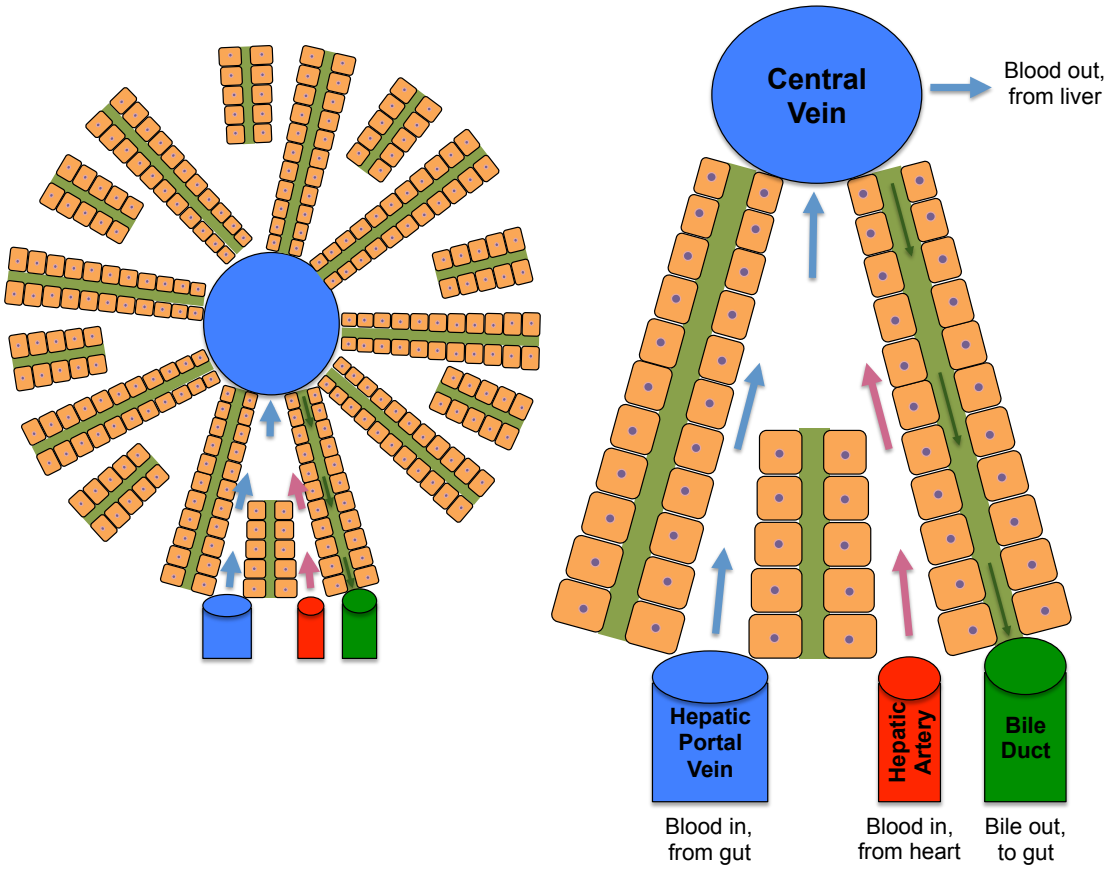

Figure 1.1 Schematic diagram of the lobular liver structure (left), zoomed in view (right).

The primary (parenchymal) cell type in the liver is the hepatocyte. Hepatocytes have three polarized domains: the apical domains forming bile canaliculi; the basal domain contacting the extracellular matrix (ECM); and the lateral domain where tight junctions exist with neighboring hepatocytes (2). The Space of Disse is the proteinaceous, interfacial region separating the hepatocytes from the liver sinusoids (**Figure 1.2**).

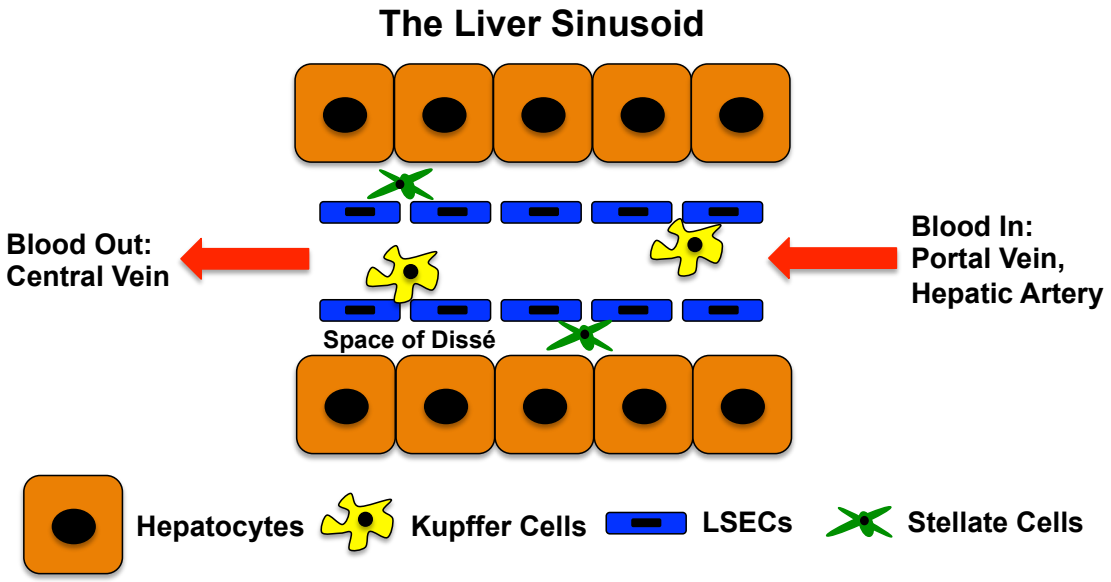

Figure 1.2 Schematic of the microvasculature of the liver known as the liver sinusoid.

The Space of Disse is a highly organized ECM consisting of proteins such as collagen types I, II, IV, and V; glycoproteins such as fibronectin, laminin, tenascin, and osteonectin; proteoglycans such as heparin and chondroitin sulfate; and glycosaminoglycans like hyaluronan (5). The liver sinusoids are lined with liver sinusoidal endothelial cells (LSECs) that possess fenestrae with pore sizes ranging from 100 – 200 nm (9, 10).

These pores play a crucial role in the passage of fluids, solutes and particles between the hepatocytes and the blood circulation. Additionally, the fenestrae also permit the passage of small molecules and metabolites to the hepatocytes effectively acting like a molecular sieve (9). The Kupffer cells reside within the sinusoid and are the resident macrophages of the liver. As the macrophage of the liver, Kupffer cells clear endotoxins and are responsible for the phagocytosis of foreign particles and bodies (11). The stellate cells, known as the fat-storing cells, contribute to remodeling of the ECM, the storage of retinoids, and secretion of cytokines (12-14).

1.1.2 Parenchymal and Non-Parenchymal Cell Types

1.1.2.1 Hepatocytes

Hepatocytes make up 60 – 80% of the liver by mass (2). They perform several liver-specific functions such as carbohydrate, lipid and amino acid metabolism, biotransformation of xenobiotics, drugs, and toxins. In addition to various metabolic functions, hepatocytes are involved in the biosynthesis of plasma proteins such as albumin and transferrin, the production of urea, and bile synthesis (2, 3). Hepatocytes are polarized, which is manifested at multiple levels such as their cell shape, cytoskeletal organization, and functionally defined domains in the cellular plasma membrane (2, 14). Hepatocytes are polygonal in morphology with f-actin localized in the cellular periphery (2). Additionally, cell polarity is critical in the maintenance of the hepatic phenotype and liver-specific functions (2, 3). Over the years, *in vitro* cultures have been developed to maintain cellular polarity and hepatic function *in vitro* (2, 3, 15, 16). Preservation of liver-specific function *in vitro* has been accomplished using ECM based substrates, adding soluble factors, and optimizing the cell-environment interactions (14-18).

1.1.2.2 Liver Sinusoidal Endothelial Cells

The second most abundant hepatic cell type (10 – 20% of the liver by mass), and most abundant non-parenchymal cell type, are LSECs (2, 9). The LSEC lining in the sinusoid behaves as a molecular sieve due to the fenestrae that are present. The pore size ranges from 100 – 200 nm and these pores can aggregate to form a dynamic and responsive filter (9, 10). The dynamic lining can contract or expand responding to various cues such as hormones, drugs and toxins. Additionally, the fenestrae permit or prevent the entry of metabolites, pathogens, and other circulating cell types found in the blood (9, 10). Through endocytosis and transcytosis, LSECs transport macromolecules from the bloodstream to the Space of Disse acting as a selective barrier (9).

LSECs are capable of receptor-mediated endocytosis (19) due to their high affinity endocytotic receptors enabling the endocytosis of collagen, hyaluronan, and cholesterol (10, 19-26). The receptor-mediated endocytosis of acetylated low-density lipoprotein (acLDL), a product of lipid metabolism, is a unique marker of LSEC phenotype (26, 27).

Additionally, the presence of the surface marker Cd32b (binding with sinusoidal endothelial 1 antibody) provides another method to non-invasively assess the maintenance of LSEC phenotype (28, 29). In addition to their selective properties, LSECs are a scavenger system that removes waste products from the bloodstream and liver.

1.1.2.3 Kupffer Cells

Kupffer cells serve as the resident macrophage of the liver and constitute 5% of the cell types found in the liver (2). In their role as a macrophage, these cells mediate acute and chronic responses of the liver and maintain hepatic homeostasis (30). The primary functions of these cells include phagocytosis of foreign bodies, removal of endotoxins, antigen presentation, production of pro-inflammatory cytokines, and the administration of the immune response (2, 31, 32). Pathogen-activated Kupffer cells release inflammatory cytokines such as TNF-α, chemokines, growth factors and reactive oxygen species such as nitric oxide and superoxide (31). When the liver is not inflamed, Kupffer cells release anti-inflammatory cytokines such as interleukin-10 (IL-10) and TGF-β which down-regulate T cell activation and receptor mediated antigen uptake (11, 31). Additionally, Kupffer cells can migrate throughout the liver sinusoid. In addition to administering an immune response, pro-inflammatory cytokines secreted by Kupffer cells have been shown to mediate glucose production (33) and cytochrome P450 enzyme activity in hepatocytes (34, 35).

1.1.2.4 Stellate Cells (Ito and Fat-Storing Cells)

Stellate cells, that comprise approximately 5% of the liver (11) are responsible for storage of fat-soluble vitamins such as retinoids which maintain cell proliferation and differentiation, a healthy immune system and vision (36). Additionally, stellate cells remodel the ECM by producing collagen (types I, II, IV, VI), fibronectin, laminin, proteoglycans, and matrix metalloproteinases (MMPs) (12). Stellate cells are involved in the production of growth factors such as TGF-β1 (involved in human hepatic fibrosis), cytokines such as platelet-derived growth factor (PDGF), and the contraction and expansion of the lumen in response to vasoconstrictors (13, 36). Stellate cells exist in two phenotypes, quiescent and activated. Quiescent stellate cells exhibit cytoplasmic lipid

droplets and dendritic-like prolongations that wrap the sinusoids (14, 36). Expression of α-smooth muscle actin, vimentin and desmin are markers for quiescent stellate cells (12). Activated stellate cells lack lipid droplets and display a proliferative myofibroblast-like morphology (12).

1.1.3 Hepatocyte Culture Systems

Freshly isolated hepatocytes cultured in conventional 2D cultures exhibit rapid loss of liver-specific functions such as urea production, albumin secretion and detoxification within 24 h (2, 3, 15, 16, 37). Efforts to mimic *in vivo* conditions have included controlling cell-ECM interactions (15-17), homotypic and heterotypic cell-cell interactions (37-45), and by adding hormones and other soluble factors (46).

The most common *in vitro* culture system consists of cellular monolayers on collagen or Matrigel^{TM} substrates and collagen sandwiches (15-17). Cellular monolayers cultured on ECM proteins are unstable and lose their phenotypic-specific functions rapidly (15-17). Upon addition of a secondary collagen layer on top of a hepatocyte monolayer, their morphology and liver-specific functions have been maintained for at least six weeks (47). Such cultures are called collagen sandwiches. When cultured on Matrigel^{TM}, a protein mixture of basement membrane extract from Engelbreth-Holm-Swarm (EHS) mouse sarcoma, hepatocytes form stable spheroids due to homotypic cell-cell interactions (15). All of these cultures are comprised solely of parenchymal cells, which do not closely resemble the complex 3D liver architecture found *in vivo*.

Recent studies have focused on stacking hepatocyte only cultures in 3D structures using self-assembling peptide nano-scaffolds (48), microporous biodegradable poly(D,L-lactide-*co*-glycolide) membranes (49), de-cellularized porcine ECM (50), and nanofibrous poly(L-lactic acid) scaffolds (51). While these cultures were 3D, the stacked hepatocytes demonstrated limited hepatic function and failed to recapitulate the multicellular nature found in the hepatic microenvironment.

Hepatocytes have been co-cultured with other cell types to promote heterotypic cell-cell interactions in 2D cultures. Hepatocytes have been cultured with non-hepatic cells such as embryonic murine 3T3 cells (44), rat dermal fibroblasts (52), human fibroblasts (53), and bovine aortic endothelial cells (18, 52). In addition to non-hepatic cells, liver-derived cells types such as epithelial cells (38, 54), sinusoidal endothelial cells (39, 40), rat hepatic stellate cells (55), and Kupffer cells (41, 42) have been co-cultured with hepatocytes. Despite these advances, these cultures are 2D and do not provide the 3D layered structure found *in vivo*.

Approaches to develop 3D layered hepatic constructs that more closely resemble the *in vivo* environment include the use of temperature-responsive polymers or magnetite particles (56-60). A thermo-responsive polymer, poly (*N*-isopropylacrylamide) (NiPAAM), has been used to culture cell monolayers. At 20 °C, NiPAAM depolymerizes and the cells cultured on this substrate can be harvested as a cell sheet. Human aortic endothelial cells (HAECs) were first cultured on NiPAAM, then, removed as a cell sheet and finally, placed directly above a layer of primary hepatocytes (56-58). Hepatocytes cultured in this manner maintained polygonal morphology and stable albumin expression compared to monolayers (56-58). In another approach, magnetite cationic liposomes (MCLs) were used to assemble HAECs above a hepatocyte monolayer (59, 60). HAECs were labeled with MCLs by electrostatic interactions between the particles and the cell membrane (60). MCL uptake studies revealed an accumulation of 38 pg of magnetite per cell within 8 h and labeled HAECs exhibited no difference in growth compared to unlabeled HAECs (60). Using a magnet, labeled HAECs were manipulated and placed directly above hepatocytes (60). After 2 days of culture, HAECs remained attached to the hepatocyte layer without the presence of a magnetic field (60). Albumin secretion was significantly enhanced in the layered constructs compared to hepatocyte-only and 3D co-cultures of hepatocytes with HAECs (60). However, both of these cell-layering approaches use potentially toxic monomers and particles with unknown long-term effects to assemble layered cell sheets. Additionally, the long-term stability and ease of handling such cell sheets are of concern for these methodologies.

Recently, March *et al*. used reconfigurable cell culture substrates to promote paracrine signaling between hepatocytes and LSECs while avoiding the use of potentially cytotoxic materials (28). Through the use of a micromechanical cell culture substrate, LSECs were cultured with hepatocytes in 'contact' or 'gap' mode (28). In the 'contact' mode, LSECs were cultured with hepatocytes to promote contact-mediated signaling between the two cell populations. In the 'gap' mode, LSECs were separated from hepatocytes by a 80 μm 'gap' whereby cells could only communicate by diffusible soluble signals. LSEC phenotype, as measured by CD32b (SE-1) expression and uptake of acLDL was only observed for LSECs in the 'gap' mode only indicating the need for the 3D separation of the two cell types (28).

In addition to separating the parenchymal cells from the non-parenchymal cells by an interface, Guzzardi *et al*. attempted to recapitulate the 3D structure by culturing hepatocytes with other cell types in a multi-compartmental modular bioreactor (MCmB) (61). The MCmB represents a system where hepatocytes were cultured with other tissue types, such as adipocytes, in different chambers that were connected by flow of culture-medium. The MCmB configuration promoted paracrine and endocrine signaling without direct contact between the different cell types. Simple diffusion and laminar flow conditions were investigated to determine the effect of hepatocyte/adipocyte cultures on metabolic regulation (61). Hepatocytes cultured in the MCmB with an adipocyte chamber exhibited enhanced metabolic functions such as urea production, albumin secretion, and glycogen/ fatty free acid homeostasis (61). These results coupled with the study by March *et al*. indicate the necessity of culturing hepatocytes with non-parenchymal cells while limiting direct contact between the two cell types. However, in both of these studies the overall distance of separation between the two cell types was at least 80-fold higher than the overall thickness of the Space of Disse *in vivo*, potentially limiting the non-contact interactions of the two cell types.

1.2 POLYELECTROLYTE MULTILAYERS (PEMs)

1.2.1 Introduction to the Layer-by-Layer (LbL) Assembly of Polyelectrolytes (PEs)

The LbL of PEs was pioneered by Decher *et al*. in the 1990s (62, 63). The self-assembly of alternately charged PEs results in the formation of PEMs. (**Figure 1.4**). The process of self-assembly is usually a result of electrostatic interactions (64). However, other interactions between polymers such as hydrogen bonding (65), complimentary base pairing (66), and click chemistry (67) have also been exploited to assemble PEMs. The ease of assembly and diversity of PEs has led to a multitude of biological applications including drug delivery, antibacterial coatings, and hepatic tissue engineering (68-72).

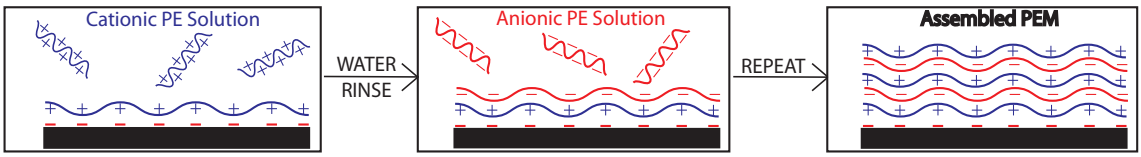

Figure 1.3 Schematic of PEM assembly. Reprinted with permission from (73).

The properties of PEMs can be wide ranging due the ability to choose from a wide range of cationic and anionic PEs, changing their solution properties and their deposition times. In addition, post-assembly modifications enable tuning the chemical and mechanical properties. The resulting PEMs are highly dependent on PE solution properties such as pH (74), ionic strength (75) and PE concentration (75-77). Additionally, the thickness can be directly controlled by choosing the number of bilayers in the multilayer (a bilayer consists of one cationic PE and one anionic PE) and through changes in the deposition conditions and the introduction of hydrogen bonding (64, 76). Post-assembly methods typically include crosslinking (78-83), changing the pH (74-77), or the addition of functional groups (84-87).

1.2.2 Methods for PE Deposition

The LbL buildup of PEs has been accomplished using various techniques. Virtually all PEMs first require a charged substrate. Dip coating has been extensively explored due to the relative ease of immersing a charged substrate into a PE solution (62-64, 75-77, 88). Substrates are immersed in PE solutions for a period of time (ranging from 30 seconds to

1 h), and then rinsed to remove any unbound PE. In addition to coating 2D surfaces, PEMs have been assembled on 3D substrates such as cellulose fibers and polystyrene latex particles (89, 90). More recently, spray coating has been used to reduce the need to remove excess PEs using a rinse step (91, 92). Spray coating PEs such as poly (allylamine hydrochloride) (PAH) and sulfonated polystyrene (SPS) resulted in 20 bilayer PEMs assembled in 4 min compared to dipping which required 40 min to achieve similar film properties (91). However, spray coating cannot be used to assemble PEMs on substrates with complex geometries, due to the limitation of directly spraying the PEs on the substrate (typically flat, 2D surfaces).

1.2.3 Chemical Composition of PEs

Both synthetic and naturally occurring PEs have been used to construct PEMs for various applications. PAH, poly (diallyldimethylammonium chloride) (PDAC), poly (acrylic acid) (PAA) and SPS are among the most widely used synthetic PEs (74, 93-95). In addition to these, other PEs such as poly (ethyleneimine) (PEI), azobenzene dyes, and poly (vinyl sulfate) have been used for bactericidal coatings, non-linear optical materials and glucose biosensors, respectively (69, 96, 97). PEMs have been constructed from naturally occurring PEs such as polypeptides, polysaccharides, DNA and proteins (72, 78-82, 93, 98-107). PEMs have also been assembled using a combination of synthetic and naturally occurring PEs.

1.2.4 Charge Compensation in PEMs

PEM properties such as the thickness, stiffness and swelling can be correlated to the presence of charged polymer species and the counterions (63, 88). Schlenoff *et al*. first described the effect of ions present in a PEM by investigating intrinsic and extrinsic charge compensation (88). Intrinsic charge compensation is defined by the interaction between a cationic and an anionic PE, whereas extrinsic charge compensation is the matching of a charged PE with a counterion (77). Typically, charge compensation in a PEM leads to a reversal of charge upon the adsorption of a subsequent, oppositely charged PE layer. The overall charge remains net neutral due to the presence of displaced counterions interacting with the PEM extrinsically (108). Thus if the ratio of

PEs in a PEM is 1:1, the PEM is intrinsically compensated, however any other ratio indicates the PEM is extrinsically compensated (108). Due to the ability to change the stoichiometry of the PEM by counterions, the overall charge and chemical composition of the PEM can be chosen for the desired application (109).

1.2.5 PEM Thickness

Self-assembling PEMs can grow either in a linear manner or through exponential growth (62-64, 78, 99, 104, 105). When PEMs are assembled using a combination of strong PEs, the thickness has been observed to increase linearly as a function of the number of bilayers (64, 76). For example, studies have shown that PEMs comprised of PAA and SPS exhibit such a growth mechanism (**Figure 1.5**) (64). This linear growth is attributed to the high charge density distributed along the backbone of these strong PEs (64, 76, 77). In addition to a linear growth, such PEMs often exhibit clearly defined layers due to intrinsic charge compensation negating PE diffusion (77).

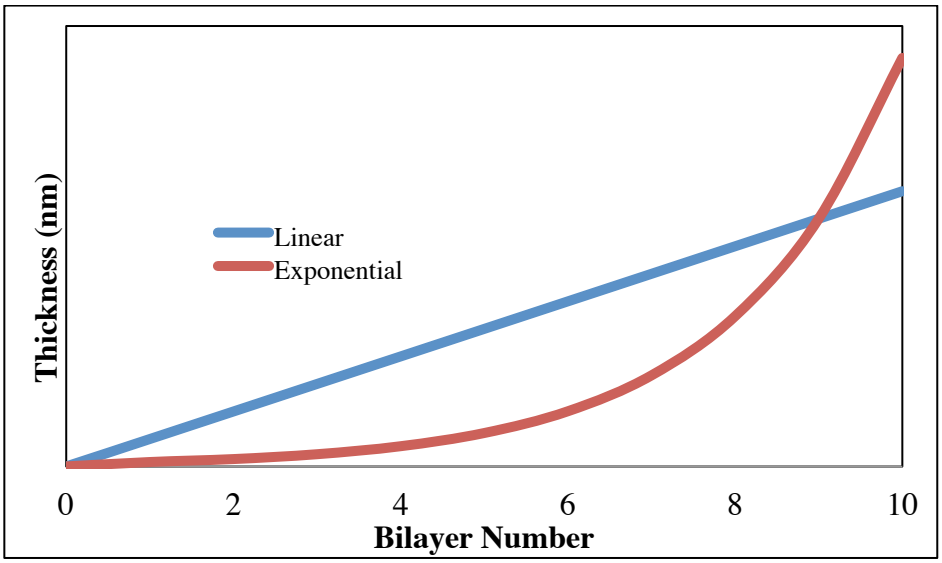

Figure 1.4 Linear and exponential growth of PEMs. Reprinted with permission from (73).

In contrast, multilayers assembled from weak PEs grow in an exponential fashion. Examples of weak PEs that can grow exponentially include PLL, (HA), and poly (L-glutamic acid) (PLGA) (**Figure 1.5**) (98, 99, 103, 110). Exponential growth is attributed

to the diffusion of PEs within the multilayer and hydrogen bonding (111, 112). Picart *et al*. described the exponential growth mechanism in a PLL/HA PEM. During contact of the PEM with the PLL solution, PLL chains diffused into the interior of the multilayer (103, 113). Upon immersion of the PEM in a HA solution, PLL chains diffused toward the surface resulting in the formation of aggregates and an exponential increase in the thickness of the resulting multilayer(103, 113).

Recently, multilayers have been assembled with a combination of both linear and exponential growth regimes to create PEM "compartments" (114). These "compartments" create regimes for promoting or preventing free diffusion of PEs within an exponential region and linear regions respectively (114). Garza *et al*. used exponential and linear growth modes to design multiple reservoirs within a PEM for applications in drug delivery (114). Impermeable layers of spray-deposited PLGA prevented direct cellular contact with drug-load reservoirs for up to 5 days (114).

1.2.6 Mechanical Properties of PEMs are a Function of Chemical Composition, Assembly Conditions and Post-Assembly Modifications

Through the incorporation of PEs such as carrageenan with different chemical structures, Schoeler *et al*. demonstrated the ability to modify the stiffness of a PEM (115). The film stiffness was three times higher for PEMs assembled with ι-carrageenan compared to λ-carrageenan due to the differences in chain conformations of the polysaccharides. ι-carrageenan exhibits a helical structure while λ-carrageenan exhibits a random coil conformation (115). Another method is through the incorporation of nanoparticles. The incorporation of poly (ferrocenylsilane) organometallics and single-wall nanotubes (SWNTs) has resulted in stiffness changes of up to two orders of magnitude (116-118). Upon incorporation of SWNTs into PDAC and PAA PEMs, the tensile strength increased from 200 kPa to 70 MPa due to the high strength properties of SWNTs (117).

The disassociation of functional groups in a PE is based upon the pH of the solution. When the pH of the solution is close to the pK_a of a PE, the PEs have a low charge density and adsorb in a thick and loopy conformation. If the pH of the PE solution is

several units from its pK_a, the chains are highly charged and adsorb in a thin, rod-like conformation (64, 76, 77). Mermut *et al*. demonstrated a reduction in in Young's modulus, from 6.5 to 0.1 MPa simply by increasing the pH from 5 to 9 for a PEM assembled from PAH and an azo-benzene PE (119). Additionally, changing the solution pH has led to changes in thickness, surface roughness and the hydrated film thickness of PEMs (120, 121).

When a PEM is assembled from strong PEs, changing the ionic concentration can be an effective method to tune its mechanical properties. Adding salts, such as NaCl, effectively screens electrostatic charges by reducing the Debye length (75, 76). The Debye length is the distance at which a charge is experienced, and the addition of salts reduces this distance, thereby, decreasing the effective charge density (75, 76). These changes in charge density have a similar effect to changes induced by pH. For example, increasing the ionic concentration of NaCl from 0 to 2 M led to film swelling and a reduction in rigidity for SPS/PDAC PEMs (75). These PEMs (10 bilayers) swelled from 10 nm to 350 nm upon the addition of 2M NaCl. (76).

Chemical crosslinking is a commonly used technique to create covalent bonds within the PEM to modulate degradation and mechanical properties. One of the simplest routes to chemical crosslinking is to heat multilayers that contain functional groups such as carboxyl and primary amines to promote amidization. The presence of amide bonds has been shown to prevent degradation and simultaneously increases the Young's modulus (122). Another commonly used approach is the use of crosslinking agents such as glutaraldehyde (GA). In the presence of primary amine groups, GA covalently binds to amines and creates inter- and intra-molecular crosslinks (123). GA crosslinking has been shown to result in a one- to two-fold increase in the Young's modulus (83). More elaborate crosslinking methods have been utilized such as the use of zero-length crosslinkers (i.e. no additional molecules added to final PEM structure) and the incorporation of UV-reactive moieties into the PEM functionality. The use of carbodiimide chemistry has opened up new avenues for the crosslinking of PEMs (78, 79,

124). By varying the concentration of carbodiimides present in post-assembly solutions, the degree of crosslinking can be modified (80).

1.3 PEMS AND CELLULAR INTERACTIONS

1.3.1 Assembly Conditions Modulate Cellular Adhesion

In order to elicit a specific cellular response, the mechanical properties of a PEM are often tailored (74, 78, 80-83, 105, 125). A property such as PEM thickness can be used to tune the stiffness and subsequent cellular adhesion. Richert *et al*. assembled PLL/HA PEMs at various thicknesses, ranging from 3 to 15 μm (79). When smooth muscle cells (SMCs) were cultured on PLL/HA PEMs, differences in the cellular spreading were observed and correlated inversely to the thickness of the multilayer (79). SMCs cultured on 3 μm thick PEMs exhibited areas of 1100 μm^2 compared to 800 μm^2 for 15 μm thick films (79). The Young's modulus of the PEMs varied from 90 kPa (3 μm) to 40 kPa 15 μm) indicating cellular adhesion and spreading were dictated by changes in rigidity as a function of the height of a multilayer. (79). Additional studies with human chondrosarcoma cells on PLL/PLGA PEMs have demonstrated decreases in cellular adhesion with increasing thickness (80).

Mendelsohn *et al*. demonstrated the ability to tune cellular adhesion of murine NR6WT fibroblasts by adjusting the pH during assembly. PAH/PAA PEMs assembled at pH 6.0 exhibited excellent cellular adhesion compared to multilayers assembled at pH 2.0 (74). Differences in cellular adhesion were attributed to increased rigidity and decreased hydration at pH 6.0 compared to PEMs assembled at a lower pH (74, 120).

Functional groups such as amines or carboxylic acids offer routes to introduce crosslinks inter- and intramolecularly (79, 123). Water-based crosslinking methods have been investigated using carbodiimide chemistry with zero-length EDC crosslinkers (79). Ren *et al*. modulated myoblast adhesion, differentiation and myotube formation by crosslinking PLL/HA PEMs using 1- ethyl -3-[3-dimethylaminopropyl] carbodiimide hydrochloride (EDC) (125). EDC concentrations ranging from 5 to 100 mg/mL were used with the highest concentration yielding a PEM modulus of 400 kPa (125). The stiffest PEMs exhibited excellent myoblast adhesion with well-defined focal adhesions and f-actin fibers (125). Additionally, myotube morphology was modulated by PEM

stiffness with the formation of thin, elongated tubes on the stiffest PEMs (125). GA has also been used to covalently bind free amines present in PEMs (83, 126). Larkin *et al*. crosslinked chitosan/HA PEMs by exposure to an 8 wt. % GA solution for either 1 or 2 minutes (83). PEM stability increased from complete degradation within 5 min (in phosphate buffered saline; 1X PBS) to at least 92 % weight retention over 7 days (83). Additionally, the Young's modulus increased to 310 and 480 MPa, for 1 min and 2 minute crosslinked PEMs respectively in comparison to 90 MPa for an unmodified film (83). When BALB/c 3T3 fibroblasts were cultured on the crosslinked chitosan/HA PEMs, the cells colonized the crosslinked PEM surface within 6 days and exhibited well-defined f-actin fibers (83).

Crosslinking that does involve exposure to possible cytotoxic crosslinkers have also been utilized to modulate the properties of PEMs. Moussallem *et al*. thermally crosslinked PAH/PAA PEMs by exposure to increased temperatures (127). Exposure to high temperatures (180 °C) led to the creation of amide crosslinks. Upon crosslinking, the hydrated Young's modulus increased to 8 GPa compared to 6 MPa for unmodified PEMs (127). Rat aortic SMCs cultured on these crosslinked PEMs expressed contractile phenotypic markers such as calponin and smooth muscle α-actin (127). SMCs cultured on unmodified PEMs did not express these markers, indicating that thermal crosslinking potentially directed their phenotype (127).

1.3.2 PEM Composition and Cellular Adhesion

In one of the first studies including biological PEs, Lvov *et al*. demonstrated that PEMs comprised of DNA and PAH could be assembled to potentially investigate template-dependent synthesis of polyamines by copying the natural principles of DNA packing. For example, the DNA/PAH PEMS could be used to study the interaction of negative charges of DNA phosphates with precisely spaced, positively charged amine groups (128). In biological applications, cellular response can be enhanced or inhibited depending on the PEs used. For example, Elbert *et al*. assembled PEMs comprised of the naturally occurring PEs, poly (L-lysine) (PLL) and alginate (ALG) (98). These PEMs were used to render surfaces biologically inert and block the adhesion of human

fibroblasts (98). Whereas, Berg *et al*. assembled PAA and arginine-glycine-aspartic acid (RGD) modified PAH multilayers that promoted murine wild-type NT6 fibroblast adhesion (121). The RGD peptide was chosen due to its ease of incorporation onto the PEM surface and its role in promoting cellular adhesion (121).

Richert *et al*. assembled PLL/PLGA PEMs and chose to make the final PE layer comprised of a polyanion or polycation. Therefore, the final PE layer (referred to as the terminating layer) was either PLL or PLGA. Human chondrosarcoma cells adherent on PEMs terminating in PLL exhibited 80 nN adhesion forces, 8-fold higher compared to PLGA-terminated films as determined by micropipetting (104). However, when the PEMs were sufficiently stiff, Thompson *et al*. observed that the terminating PE layer had no significant effect on microvascular endothelial cell (MVEC) proliferation (120). In some cases, the choice of the cationic PE is important since they can result in cytotoxicity. When polyethylenimine (PEI), a cationic PE was used to assemble a PEM, it resulted in the death of periodontal fibroblasts (129). Fischer *et al*. compared PEI, PLL and PDAC polycations and found that L929 mouse fibroblasts exhibited lower metabolic activity on PEI than PLL or PDAC (130). Similarly, the cytotoxicity of polyanions has been investigated. Polyanions such as dextran sulfate and derivatives of bovine serum albumin have demonstrated slight cytotoxic effects in primary brain microvessel endothelial cells and primary rat hepatocytes, however in comparison to polycations such as PLL, protamine, and histone, these effects were minimal (131).

1.3.3 PEM Surface Morphology Modulates Cellular Migration

Cells respond to various factors in their environment including topography which can range from the nano- to the microscale (132). Basement membranes *in vivo*, exhibit porosities that range from the micro to nanoscale (133, 134). These pores enable the diffusion of gases and nutrients to cells and are therefore an important component of PEM design (135). Mendelsohn *et al*. demonstrated that pores could be induced in PAA/PAH PEMs upon exposure to an acidic aqueous solution at a pH of 2.5. The average pore size ranged from 100 to 500 nm and the porosity was attributed to the cleavage of polymer chains and their subsequent reorganization (122). Further studies by

Hiller *et al*. revealed nanoscale porosities (15 to 80 nm) when the solution pH was further reduced to 1.8 (136). In both cases, the porosity was maintained by heating at 200°C to introduce thermal crosslinks (122, 136). Both of these studies outlined a new method for inducing porosity (**Figure 1.6**), however the effect of pore size on cellular response was not investigated. Recently, Hajicharalambous *et al*. showed that submicron and nanoporous PEMs exhibiting an average pore size of 100 to 600 nm can be used to mimic the basement membrane of the human cornea (133, 134). Human corneal epithelial cells (HCECs) were cultured on PAA/PAH PEMs with average porosities of 100 and 600 nm (137). PEMs with pore sizes of 100 nm exhibited two-fold higher migration speeds of approximately 30 μm/h when compared to 600 nm pore-sized PEMs (137). Porosity also affected cytoskeletal organization, with HCECs only exhibiting well-defined actin structure and vinculin focal adhesion on the nanoporous PEMs (137).

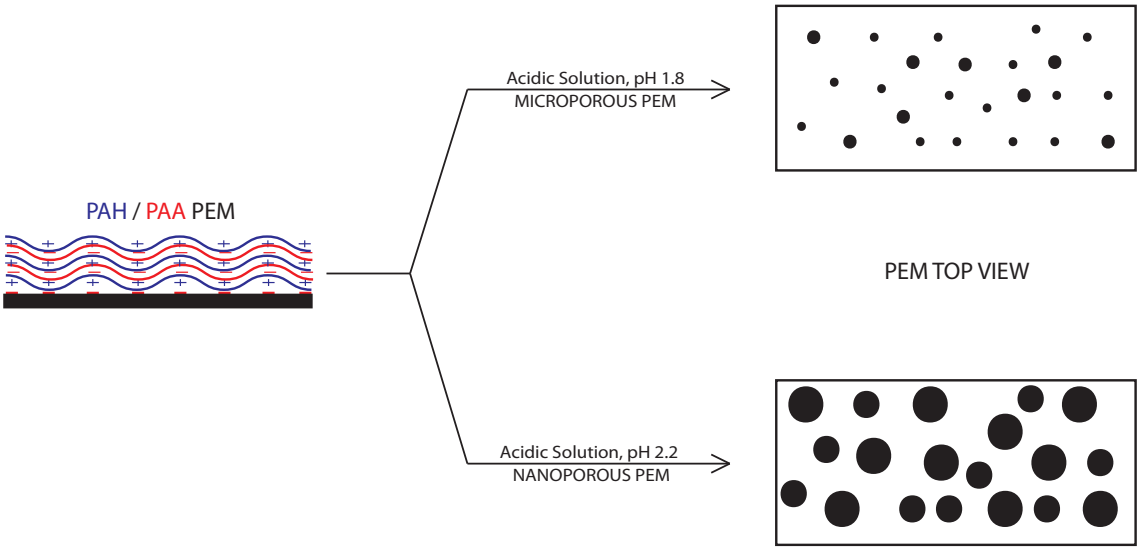

Figure 1.5 Schematic representation for the creation of nanoporous PEMs comprised of PAA and PAH. Reprinted with permission from (73).

1.4 PEMS USED FOR CULTURING PRIMARY HEPATOCYTES

PEMs have previously been used as a planar substrate for the culture of primary hepatocytes. Kidambi *et al*. used PDAC as the cationic PE and SPS, PVS, or PAS as the anionic PEs (138). Primary hepatocytes attached and spread on all PEMs over a 7-day culture period (138). The terminating PE layer was varied between PDAC, SPS, PVS, and PAS to investigate the effect on hepatic functions. Both urea production and albumin secretion were significantly higher than collagen-coated tissue culture polystyrene for all terminating PE layers, however both functions decreased over the culture period (138).

More recently, Chen *et al*. investigated the effect of both mechanical compliance and ligand presentation of synthetic PEMs for increasing cell adhesion and liver-specific functions of primary rat hepatocytes (139). Synthetic PEMs comprised of PAH and PAA exhibited elastic moduli that ranged from 200 kPa to 142 MPa. Negligible hepatocyte attachment was observed on the most compliant 200 kPa PEM while 100% attachment was observed on the most compliant, 142 MPa, PEM (139). Decorin and collagen were used to promote cell adhesion and liver-specific functions of hepatocytes on the PEMs. Urea production, albumin secretion, and CYP1A activity was increased in primary hepatocytes cultured on PAH/PAA PEMs coated with collagen compared to tissue culture flasks coated with collagen (139).

In addition to cultures of primary hepatocytes, patterned co-cultures of primary hepatocytes and fibroblasts using PEMs have also been investigated. Kidambi *et al*. used PDAC/SPS PEMs that were patterned with SPS using microcontact printing. Primary hepatocytes demonstrated a preferential attachment on the SPS compared to PDAC. In contrast, fibroblasts were adherent to both SPS and PDAC. Patterned PEM cultures of primary hepatocytes exhibited lower urea production and albumin secretion over a 7-day culture period. However, upon introduction of fibroblasts, albumin production increased 6-fold over the 7-day culture (140). While these studies highlight the ability to use PEMs for culturing primary hepatocytes, all of these cultures are 2D in nature and do not recapitulate the 3D hepatic microenvironment.

1.5 THE 3D LIVER MIMIC

In an effort to more closely mimic the key physiological, spatial and geometrical characteristics of the hepatic environment *in vivo*, our research group has assembled a 3D liver mimic (**Figure 1.4**) (70-72).

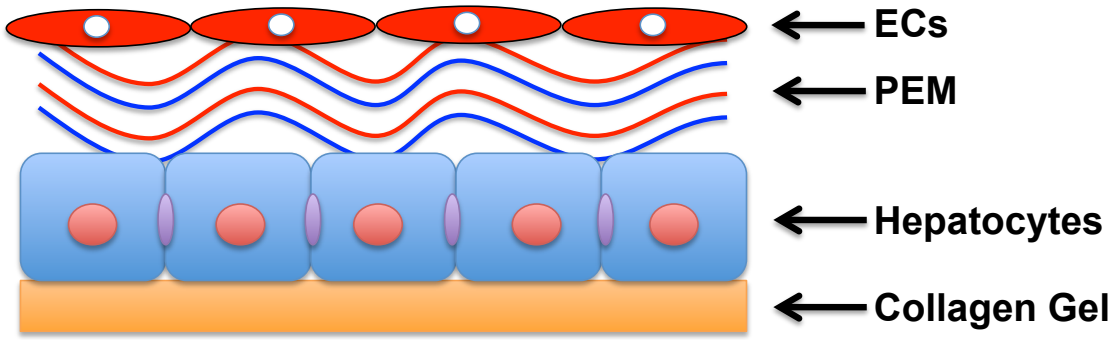

Figure 1.6 A schematic of a general 3D liver mimic containing endothelial cells (ECs), a PEM and hepatocytes.

Initially, the 3D liver mimic was comprised of primary rat hepatocytes, human umbilical vein endothelial cells (HUVECs) and an intermediary PEM. Henceforth, this combination is referred to as HEP+PEM+HUVEC (72). The intermediary PEM layer was assembled directly on live hepatocytes using chitosan and DNA. Chitosan and DNA served as the cationic and anionic PEs, respectively. These PEs were chosen for their compatibility with endothelial cells and hepatocytes (85, 141-144). The intermediate PEM provided a cell-adhesive surface for culturing a second layer of cells (72). By incorporating the PEM, optimal hepatic function was obtained for HEP+PEM+HUVEC constructs compared to hepatocyte monolayer cultures. Additionally, the presence of the PEM maintained the classic polygonal hepatocyte morphology (72). However, the PEM was assembled directly above hepatocytes limiting further modifications. Another concern was the use of DNA, which is susceptible to enzymatic degradation. Although the presence of HUVECs significantly enhanced hepatic function they are not the resident endothelial cells of the liver.

More recently, a 3D liver mimic was assembled using primary rat hepatocytes and human LSECs (the combination is referred to as HEP+PEM+hLSEC) (70). The intermediate

PEM was comprised of chitosan and hyaluronic acid (HA). Chitosan/HA PEM properties were measured using a quartz crystal microbalance (QCM) with dissipation monitoring. The thickness of the hydrated PEMs was found to range between 30 to 55 nm for 5 and 15 layer PEMs, respectively (70). The shear modulus was approximately 100 kPa and the PEMs had a viscosity similar to that of water (~ 2 mPa s) indicating these PEMs were highly hydrated (70).

Primary hepatocytes cultured in a hepatocyte monolayer (HM) and collagen sandwich configuration (CS) served as the negative and positive controls, respectively. In the CS configuration, where a second layer of collagen gel is placed above the hepatocytes, have demonstrated maintenance of urea production, albumin secretion, and cellular morphology for up to 4 to 6 weeks (16, 17, 47). The presence of a chitosan/HA PEM maintained cellular morphology in HEP+PEM constructs. This was demonstrated through actin localization around the periphery compared to stress fibers observed in the HM cultures (70). Additionally, hLSEC phenotype was maintained in the HEP+PEM+hLSEC construct as indicated by the receptor-mediated endocytosis of acLDL (70). Furthermore, liver-specific functions such as urea production and albumin secretion were statistically higher in HEP+PEM+hLSEC constructs compared to HM on day 7 (70). An important feature of differentiated hepatocytes is the presence of bile canaliculi. Well-defined bile canaliculi were observed in the HEP+PEM+hLSEC and CS cultures whereas HMs exhibited diffuse fluorescence indicating the absence of the canaliculi (70). Additionally, CYP1A1/2 activity in HEP+PEM+hLSEC constructs exhibited a 4 to 16-fold increase compared to a 2-fold in the CS. (70)

In our most recent study using the 3D liver mimic, primary rat LSECs (rLSECs) were incorporated to determine if the dedifferentiation of both cell types could be prevented. In this study, rLSECs were seeded on chitosan/HA PEMs that had been deposited above a layer of hepatocytes (71). Adhesion and proliferation of rLSECs were only observed in HEP+PEM+rLSEC cultures (71). Additionally, LSEC phenotype was verified by immunostaining for sinusoidal endothelial 1 (SE-1) antibody, indicating the presence of the cell-surface marker identified as Cd32b (71). At days 4 and 12, maintenance of

rLSEC phenotype was verified in the HEP+PEM+rLSEC constructs whereas rLSEC monolayers exhibited only weak fluorescence indicating dedifferentiation (71). Urea and albumin production, and the presence of well-defined bile canaliculi confirmed maintenance of hepatic function in the HEP+PEM+rLSEC cultures (71). Additionally, CYP1A1 and CYP3A enzyme activities exhibited a 3 to 7-fold increase in the HEP+PEM+rLSEC constructs over 12 days (71). These results indicated that incorporating primary rat hepatocytes and rLSECs in a physiologically relevant model can maintain the differentiated state of both cell types. However, the assembly of the 3D liver mimic directly on live hepatocytes has several disadvantages. For example, cells are deprived of media for up to 45 min during the LbL deposition of the PEM. Additionally, tuning the properties of the PEM after deposition is virtually impossible. Perhaps the biggest disadvantage of directly assembling PEMs on live cells is the loss of the ability to perform subsequent chemistries on the PEMs, such as introducing cell-adhesive ligands.

1.6 GENOME-WIDE GENE EXPRESSION PROFILING

Genome-wide gene expression analysis can provide extensive information on the cellular processes and phenotype at the transcriptional level. Gene expression analysis can also yield information related to the presence and relative concentrations of functional gene products. Typically, gene expression comparisons are done between two culture conditions such as treated *vs*. untreated (145), cancerous *vs*. benign (146), or for a cell type exposed to different culture conditions (147). Gene expression is traditionally measured using microarray-based technologies. The basic operational principle of microarray technology is that mRNA from a cell is used to generate complimentary DNA (cDNA), which is hybridized to DNA sequences immobilized on a substrate in an ordered array (148). Each spot or probe on the array is a well-defined DNA sequence, generated from a library for the particular species of interest, and printed onto a substrate (149). The size of the probes range from 100 to 300 nm and are spaced at a similar distance from other probes. Upon introduction of the fluorescently labeled cDNA, hybridization, via complementary DNA binding, to the probe occurs (149). Each location on the microarray is examined using a laser to determine the level of fluorescence, which relates directly to the amount of cDNA hybridized to the probe (150). The fluorescence intensity for each hybridized probe can be compared to standards on the array or across contrasts to determine if a particular gene is up- or down-regulated (150). Microarrays can contain more than 30,000 probe sets. For example, the Affymetrix Genechip® Rat Genome 2.0 microarray consists of more than 31,000 probe sets, corresponding to 30,000 transcripts of 28,000 rat genes.

1.6.1 Genome-Wide Transcriptional Profiles of Commonly Used Hepatocyte Cultures

Recently, the transcriptional profiles of primary rat hepatocytes in HM and CS cultures were investigated over an 8-day period using the Affymetrix GeneChip® Rat Genome 2.0 microarray (147). Gene set enrichment analysis (GSEA) was used to summarize the temporal differences between the HM and CS at the level of predefined biological pathways, i.e. summarizing differential expression at the level of gene sets. The phenotype of the HM compared to the CS is well known to diverge in less than 24 h for

processes such as cytochrome P450 enzyme activity (151). The results of the this study revealed a significant up-regulation of liver-related functions such as bile acid synthesis as well as lipid, amino acid, alcohol, and carbohydrate metabolism in the CS compared to the HM (147). Additionally, liver-specific gene sets became increasingly significant over the culture period indicating a divergence in the phenotype of these two culture systems, correlating well with previous reports in the literature (147). These findings highlight the utility of using microarrays as a tool to assess the genome-wide gene expression profiles for hepatic model systems.

1.6.2 Gene Expression Profiles in Hepatic Multicellular Cultures

The number of literature reports investigating primary hepatocyte gene expression in multicellular cultures (e.g. hepatocytes cultured with non-parenchymal cells) is limited. Recently, March *et al*. cultured hepatocytes and LSECs together using a micromechanical substrate previously described in section 1.1.3 (28). In addition to investigating the effect of co-culture on hepatocyte and LSEC phenotype, gene expression analysis was performed on mRNA from primary hepatocytes. Spent medium obtained from LSEC cultures was used to provide soluble factors to hepatocytes. From this experiment, March *et al*. revealed that pleiotrophin, IGF-I, and angiotensin expression in hepatocytes most likely contributed to the maintenance of LSEC phenotype (28). While the presence of soluble factors in the LSEC conditioned medium most likely contributed to hepatocyte gene expression profiles and subsequent regulation of LSEC phenotype, this does not truly represent the contributions of both cell types. Reports of multicellular hepatic cultures highlight the importance of cellular signaling in the maintenance of phenotypic functions and the powerful tool that gene expression profiling can be for understanding these complex biological processes.

1.7 RESEARCH OBJECTIVES

The research objectives of this thesis are motivated by the need to design 3D hepatic cellular models that closely recapitulate the geometric, spatial and physiological features found *in vivo*. To date, no culture system has accurately captured the height of the Space of Disse. Additionally, no system has included the three most common hepatic cell types into one model at physiologically relevant *in vivo* ratios. Cellular models that mimic the hepatic architecture can be used to systematically study a wide range of cues and stimuli. We have designed nanoscale detachable, and biocompatible PEMs comprised of chitosan and HA that serve as a substitute for the Space of Disse. The use of detachable PEMs whose properties can be modulated to those found in the liver are highly desirable. Additionally, Kupffer cells, the resident macrophage of the liver, were incorporated into the 3D liver mimic. The inclusion of Kupffer cells should provide additional communications and soluble signals between parenchymal and non-parenchymal cells. The performance of 3D liver mimics were compared to HM, CS, and 2D co-cultures. The ability for each of the three cell types in the 3D model, to maintain their differentiated state was studied.

1.7.1 3D Design Criteria for 3D Liver Models

In vivo, hepatic parenchymal cells are separated from non-parenchymal cells by a protein-rich interface named the Space of Disse. The thickness of the Space of Disse ranges from 0.5 – 1 μm (2). Detachable PEMs comprised of HA and chitosan were designed to mimic the height of the Space of Disse. The design considerations for the detachable PEMs and the 3D liver mimic were as follows:

1. The detachable PEM should be comprised of biocompatible PEs that are compatible with all cell types to be incorporated into the 3D liver models.
2. The detachable PEM should be similar to the thickness of the Space of Disse and be stable in aqueous medium to prevent degradation. The detachable PEM should have similar mechanical properties to that of the liver in vivo. Since there are no reports of the mechanical properties for the Space of Disse, mechanical properties

previously obtained for bulk liver will be our goal. Previously reported measurements for bulk liver modulus range from 40 to 200 kPa (152, 153).

3. The 3D liver mimic should include the main cell types found in the liver.

1.7.2 Stated Research Objectives

The research objectives of this thesis are:

1. Assemble biocompatible, detachable PEM comprised of chitosan and HA.
2. Tune the properties of the detachable PEM (e.g. thickness and modulus) to more closely mimic the Space of Disse.
3. Investigate hepatic functions and the ability of all three cell types to maintain their differentiated state over the culture period.
4. Conduct genome-wide gene expression studies of hepatocytes to identify key hepatic cell processes that are upregulated in the 3D liver models.

1.8 EXPERIMENTAL PLAN

1.8.1 Aim 1: Design and Assemble 3D Liver Sinusoidal Mimics (Specific Contribution: Measuring PEM Properties)

The first objective of this research project was to measure the mechanical properties of PEMs used to mimic the Space of Disse *in vitro*. The PEMs were assembled using HA and chitosan. The PEM viscosity, shear modulus, and hydrated thickness were measured using a QCM-D. The frequency and dissipation data were modeled using a Voigt model for a viscoelastic thin film layer.

1.8.2 Aim 2: Design Detachable and Biocompatible PEMs

One of the primary goals of this thesis was to assemble detachable PEMs comprised of HA and chitosan for mimicking the Space of Disse. The optimal PE concentration, bilayer number, and solution pH for assembling detachable PEMs were determined. The detachable PEMs were characterized using x-ray photoelectron spectroscopy, FTIR, stability measurements, profilometry, UV/vis spectroscopy, and atomic force microscopy. The biocompatibility of the PEMs was assessed using 3T3 BALB/c fibroblasts. The proliferation and cytoskeletal organization of adherent 3T3 BALB/c fibroblasts was used to determine the biocompatibility of the PEMs.

1.8.3 Aim 3: Design Detachable PEMs that Mimic the Space of Disse

After designing 3 micron detachable HA and chitosan PEMs, the next goal was to reduce their thickness to mimic the Space of Disse. This was achieved by varying the PE concentration, solution pH, and the number of bilayers. The PEM properties were characterized using atomic force microscopy, stability studies, UV/vis spectroscopy, and profilometry.

1.8.4 Aim 4: Incorporating Detachable PEMs into a Multicellular 3D Liver Mimic

The final objective of this thesis was to incorporate detachable PEMs that mimicked the Space of Disse into a multicellular 3D liver model. Detachable PEMs comprised of 12.5 bilayers of chitosan and hyaluronic acid (thickness of 600 nm under hydration) were used

to mimic the Space of Disse *in vitro*. The 3D liver mimics were assembled by layering LSECs and Kupffer cells on PEMs placed above hepatocytes. The 3D liver mimics were maintained for 12 days. The phenotype of hepatocytes, LSECs, and Kupffer cells was monitored over the culture period. Hepatocyte function was monitored by measuring urea production, albumin secretion, and CYP1A1 isoenzyme activity. LSEC phenotype was monitored by sinusoidal endothelial-1 surface receptor activity on days 4 and 12. Kupffer cell phenotype was monitored by CD163 surface receptor (ED-2) activity on days 4 and 12. The number of hepatocytes, LSECs, and Kupffer cells were counted on days 4 and 12 to determine the extent of proliferation and *in vitro* cellular ratios. Gene expression analysis of the 3D liver mimics was conducted to determine the effect of intercellular signaling on maintaining hepatic phenotype. These studies also enabled the identification of molecules that potentially played a role in upregulated hepatic processes.

Chapter 2. Published in Tissue Engineering.

Kim Y, Larkin AL, Davis RM, Rajagopalan P. The Design of In Vitro Liver Sinusoid Mimics Using Chitosan-Hyaluronic Acid Polyelectrolyte Multilayers. Tissue Eng Pt A 2010; 16 (9): 2731-41. *Reprinted with permission from Mary Ann Liebert Publishing*.

Specific Contribution: Measurement of Chitosan-HA PEM properties using a QCM-D

Chapter 2. The Design of *In Vitro* Liver Sinusoid Mimics using Chitosan-Hyaluronic Acid Polyelectrolyte Multilayers

2.1 INTRODUCTION

The liver is one of the largest organs in our bodies and performs a multitude of functions such as metabolism, detoxification, and plays a major role in the body's complex defense mechanisms. The deterioration in any one of the liver's functions can cause serious, life-threatening health problems. The liver is comprised of ~70% hepatocytes (parenchymal cells) and the remainder is made up of non-parenchymal (liver sinusoidal endothelial, Kupffer, and hepatic stellate) cells (2). Liver sinusoids *in vivo* contain layers of hepatocytes and endothelial cells separated by the Space of Disse comprised primarily of collagen fibers (2).

In general, the lack of organ donors, the rising cost of organ transplant surgeries, and the complications related to immune response are issues that confront patients. The use of extra-corporeal liver-assist devices also known as bio-artificial livers, have the potential to enable the recovery of patients with injured livers or function as a bridge to transplantation (154).

The design of extracorporeal liver assist devices can be accelerated if three-dimensional (3-D) liver mimics are available to systematically test cellular response to a variety of stimuli. In addition, the testing of drugs and pharmaceuticals are conducted on monolayers of hepatocytes or on animals. Hepatocyte monolayers do not present a physiologically relevant model and animal models can be very expensive and complex to analyze. Although two-dimensional (2-D) cell cultures and co-cultures are used extensively as model systems (16, 17, 37, 44, 45, 155-157), they do not recapitulate key spatial, geometric, and physiological characteristics of cellular architectures found *in vivo*. The complex heterotypic interactions between parenchymal (hepatocytes) and non-parenchymal (LSEC) cells in the liver are responsible for optimal hepatic function. Recent reports in the literature have shown that even at the embryonic stage, interactions

between endothelial cells and hepatic progenitor cells are critical for normal liver development (158-160). Since interactions between the parenchymal and non-parenchymal cells of the liver are critical in maintaining optimal hepatic function (40, 161, 162), efforts to layer these cells to emulate liver architecture *in vivo* are ongoing. Recently, new approaches to form layered 3-D liver-like tissues have been reported (57, 60, 163-165). Temperature-responsive culture dishes, magnetic liposome technology, and organ-printing techniques have been utilized to form layered cell sheets. Although, these methodologies offer new avenues to assemble liver mimics, issues related to long-term stability and ease in handling and assembly are of concern.

The distance of separation between hepatocytes and endothelial cells in the liver, the Space of Disse, is a critical factor in assembling liver-mimetic tissues (72). *In vitro*, the presence of an interfacial region has been shown to play a significant role in the assembly and performance of liver mimics. In a previous report, hepatocytes and human umbilical vein endothelial cells (HUVECs) were assembled in stratified layers by incorporating a chitosan/DNA PEM between the cell layers (72). This study demonstrated the need for an interface between hepatocytes and HUVECs to obtain optimal hepatic phenotypic function and showed that PEMs to could potentially mimic and function as the Space of Disse *in vitro*. Some of the drawbacks in this study were the use of DNA as the polyanion and HUVECs. DNA is susceptible to enzymatic degradation and HUVECs exhibit significantly different phenotypic characteristics in comparison to LSECs.

We report the assembly of liver mimetic architectures comprised of primary rat hepatocytes and human LSECs with an intermediate PEM comprised of chitosan and hyaluronic acid (HA). Chitosan was selected as the cationic PE due to its compatibility with hepatocytes (85, 141, 142). HA is found in the basal membranes of connective tissues is utilized to modify surfaces for the culture of endothelial cells (143, 144). We have measured the shear modulus and viscosity of the hydrated chitosan/HA PEM and have conducted studies that demonstrate that liver-specific functions such as urea and albumin secretion, as well as cytochrome P450 (CYP1A1/2) enzymatic activity are maintained and enhanced in the liver mimetic cellular architectures.

2.2 MATERIALS AND METHODS

2.2.1 Materials

Dulbecco's Modified Eagle Medium (DMEM) containing 4.5 g/L glucose, phosphate-buffered saline (PBS), Earle's balanced salt solution (EBSS), ethoxy resorufin, penicillin, streptomycin, and trypsin-EDTA was obtained from Invitrogen Life Technologies (Carlsbad, CA). Type IV collagenase, HEPES (4-(2-hydroxyethyl) piperazine-1-ethanesulfonic acid), glucagon, hydrocortisone, ammonia, dicumarol, sodium dodecyl sulfate (SDS), and hydrogen peroxide were obtained from Sigma-Aldrich (St. Louis, MO). Human LSECs and endothelial cell growth medium and supplements were obtained from ScienCell Research Laboratories (San Diego, CA). Unless noted, all other chemicals were obtained and used as received from Fisher Scientific (Pittsburgh, PA).

2.2.2 Hepatocyte Isolation and Culture

Primary rat hepatocytes were harvested from female Lewis rats (Harlan, Indianapolis, IN) that weighed between 170-200g. A two-step *in situ* collagenase perfusion method was utilized (16, 17). Briefly, animals were anesthetized with 3 L/min of a gas mixture of 3% (v/v) isofluorane/97% oxygen (Veterinary Anesthesia Systems Co., Bend, OR). The liver was perfused through the portal vein with Krebs Ringer Buffer (KRB; 7.13 g/L sodium chloride, 2.1 g/L sodium bicarbonate, 1 g/L glucose, 4.76 g/L HEPES and 0.42 g/L potassium chloride) that contained 1mM EDTA (ethylene diamine tetra acetic acid), followed by serial perfusion with a 0.075% w/v and a 0.1% w/v collagenase (Sigma, Type IV) in KRB containing 5 mM calcium chloride. Cell suspensions were filtered through nylon meshes with porosity ranging from 250-62 μm (Small Parts, Inc., Miramar, FL). Hepatocytes were separated using a Percoll (Sigma-Aldrich) density centrifugation technique. Cell viability was determined by trypan blue exclusion. Hepatocytes were cultured on collagen-coated 6-well sterile tissue culture plates (Becton Dickinson Labware, Franklin Lakes, NJ) and were maintained in culture medium that consisted of DMEM supplemented with 10% heat-inactivated fetal bovine serum (Hyclone, UT) 200 U/mL penicillin, 200 μg/mL streptomycin, 20 ng/mL epidermal growth factor (BD Biosciences, San Jose, CA) 0.5 U/mL insulin (USP, Rockville MD) , 14 ng/mL glucagon

and 7.5 µg/mL hydrocortisone. A collagen gelling solution was prepared by mixing 9 parts of type I collagen (BD Biosciences) solution and 1 part of 10X DMEM. Sterile 6-well tissue culture plates were coated with 0.5 ml of the gelling solution and incubated at 37^{o}C for 1h to promote gel formation. Isolated hepatocytes were suspended in hepatocyte culture medium at a concentration of 1x10^{6} cells/ml and seeded on the collagen-coated wells at a density of 1 million cells/well. Collagen sandwich cultures were formed by the deposition of a second layer of collagen 24h later. Hepatocytes maintained in stable collagen sandwich and in unstable confluent monolayer cultures served as positive and negative controls, respectively. Hepatocyte cultures were maintained at 37°C in a humidified gas mixture of 90% air/10% CO_2. The culture medium was replaced every 24h and medium samples were stored until further analysis.

2.2.3 Assembly of Polyelectrolyte Multilayers (PEMs) on Hepatocytes

Chitosan (200-300kDa M.W., Sigma-Aldrich) and hyaluronic acid (HA; > 1 million M.W., Acros Organics, Fairlawn NJ) were used as the cationic and anionic PEs, respectively. Chitosan (0.01%w/v) solutions were prepared by dissolving the polymer in a 1% v/v acetic acid solution and maintained at pH values ranging from 6.1-6.3. HA (0.01%w/v) solutions were prepared by diluting in PBS and adjusted to a pH range of 7.2-7.3. PEMs were assembled on hepatocytes by first depositing a cationic PE on the cell layer followed by the anionic PE. The exposure time for each PE solution was approximately 1-2 minutes. The desired number of bilayers was obtained through the sequential and alternate deposition of PE layers. At the end of the deposition procedure, the samples were rinsed in 1X PBS and subsequently maintained in cell-culture medium at 37^{o}C.

2.2.4 Hepatocyte-LSEC Cellular Constructs

Human LSECs were maintained in medium supplemented with 5% (v/v) fetal bovine serum, 1% (v/v) endothelial cell growth supplement, 100 U/mL penicillin and 100 µg/mL streptomycin at 37ºC under a humidified gas mixture of 95% air/5% CO_2. Primary hepatocytes were first seeded on collagen-gel coated surfaces and allowed to spread up to 48-72h to form a confluent layer of cells. Thereafter, a PEM consisting of alternately

charged chitosan and HA was deposited, followed immediately by seeding a layer of LSECs. LSECs were plated at a low cell density of 5000 or 10,000 cells per sample since they proliferated over time. Non-adherent LSECs were removed 1h later. In experiments where the hepatocyte-LSEC constructs were imaged, the LSECs were tagged with a non-toxic, fluorescent, membrane-permeable dye (PKH 26 Red and Green Fluorescence Cell Linker Kit; Sigma-Aldrich) prior to seeding. Hepatocyte-LSEC cellular constructs were maintained for up to 10 days in hepatocyte culture medium. The culture medium was changed every 24h and medium samples were stored at 4**S**°C until further analysis.

2.2.5 Measurement of the Physical Properties of the PEM

The self-assembly of hydrated PEMs was monitored *in situ* using a quartz crystal microbalance with dissipation monitoring (QCM-D E4, Q-Sense, Sweden). The AT-cut quartz crystal coated (Q-Sense) with gold electrodes was cleaned with a 5:1:1 mixture of ammonia, hydrogen peroxide and 18 MΩ cm PicoPure water (Molecular Devices, Sunnyvale CA) respectively. The quartz crystal was excited to its fundamental frequency at approximately 5MHz in the QCM-D open module chamber. The PE solution was placed directly on the crystal sensor. The deposition procedures were similar to conditions used to assemble PEMs on live hepatocytes. The change in resonant frequency and the decay time of the vibration relaxations were recorded. The PEM thickness was estimated using the Sauerbrey equation (166).

$$\Delta f = -\frac{C}{n}\Delta m \qquad (1)$$

Δf = change in the resonant frequency (Hz)

Δm = change in mass per unit area ($ng.cm^{-2}$)

C= sensitivity factor ($17.7\ Hz.cm^2.ng^{-1}$)

n = overtone number

Since HA and chitosan can also exhibit viscoelastic behavior, the Voigt model (a simple spring and dashpot in parallel operating with no-slip) was applied to the QCM-D response (167). The change in resonant frequency and change in dissipation factor for a viscoelastic film are related to changes in the resonant frequency and dissipation using equations 2-4.

$$\Delta f \approx -\frac{1}{2\pi\rho_0 h_0} h\rho\omega\left(1+\frac{2h^2\chi}{3\delta^2(1+\chi^2)}\right) \qquad (2)$$

$$\Delta D \approx \frac{2h^3\rho\omega}{3\pi f\rho_0 h_0}.\frac{1}{\delta^2(1+\chi^2)} \qquad (3)$$

where ω = angular frequency, h_0 = thickness of the quartz crystal, ρ_0 = density of the quartz crystal, δ = viscous penetration depth, χ = the viscoelastic ratio (ratio of storage to loss moduli) and h and ρ are the thickness and density of the PEM, respectively. The viscoelastic ratio is defined as:

$$\chi = \frac{\mu}{\eta\omega} \qquad (4)$$

where μ = shear modulus, and η is the film viscosity. The viscoelastic ratio and thickness were varied as the change in frequency and change in dissipation data were fitted using a mean squared error (MSE) method (168, 169). Qtools software (QSense) was used to predict the layer thickness, shear modulus, and viscosity, on the assumption that the density of a PE layer is 1.1 g cm^{-3} (72).

2.2.6 Measurement of Urea Production and Albumin Secretion

Medium samples were analyzed for rat albumin concentration by an enzyme-linked immunosorbent assay (ELISA), in triplicate, utilizing a polyclonal antibody to rat albumin (Cappel Laboratories, Aurora, OH) (72). Urea concentration was determined, via its specific reaction with diacetyl monoxime using a commercially available assay kit (BUN Assay Kit Stanbio Laboratory; Boerne TX) with volumes scaled down for use in 96-well plates. The absorbance was measured on a SpectraMax M2 microplate reader (Molecular Devices). Standard curves were generated using purified rat albumin or urea diluted in culture medium.

2.2.7 Actin Cytoskeletal Staining

Hepatocyte cultures were fixed in a 2% glutaraldehyde (Electron Microscopy Sciences, Hatfield, PA) solution in PBS at room temperature for 20 min. The cultures were

exposed to a 0.1% Triton X-100 solution to render the membranes permeable and subsequently incubated with rhodamine-phalloidin (Molecular Probes) diluted in a 1% bovine serum albumin (BSA) in PBS. Actin cytoskeletal structure was imaged using an inverted Zeiss LSM510 confocal microscope (Carl Zeiss Inc.).

2.2.8 Microscopy

Cells were observed and imaged using an inverted Nikon TE-2000 (Nikon USA) microscope with 10X, and 20X objectives. Phase-contrast and fluorescent images of the cells were collected using a Hamamatsu CCD camera (Hamamatsu City, Japan) and analyzed using Nikon's Imaging Software (NIS- Elements).

2.2.9 Uptake of Acetylated Low Density Lipoprotein (acLdL) by LSECs

Hepatocyte-LSEC cultures were incubated for 3h with 20 μg/mL of Alexa Fluoro® 3,3'-dioctadecylindocarbocyanine (DiI) acLdL (Invitrogen) diluted in serum-free hepatocyte culture medium. To remove non-specifically bound acLdL, the cultures were rinsed and maintained in phenol-red free DMEM. Imaging was conducted on a Nikon TE-2000 microscope.

2.2.10 Di-peptyl Peptidase IV (DPP IV) Immunostaining to Image Bile Canaliculi

Cells were fixed in a 2% glutaraldehyde/PBS solution, followed by permeabilization for in a 0.1% Triton X-100 solution. The cultures were incubated overnight at 4^{o}C in a 3% goat serum (Chemicon) solution. The samples were incubated with a mouse monoclonal antibody to rat DPP IV (Cell Sciences, Canton, MA) and a secondary FITC-conjugated rabbit anti-mouse IgG antibody (Sigma-Aldrich) and imaged using an inverted Zeiss LSM510 confocal microscope.

2.2.11 Measurement of Cytochrome P450 (CYP1A1/2) Activity

Cytochrome P450 (CYP1A1/2) activity was induced by adding 3 methyl cholanthrene (3MC, Sigma, 2μM) to the hepatocyte cultures, 48h prior to conducting measurements. Cytochrome-P450 dependent ethoxy-(EROD) resorufin o-dealkylase detoxification was measured using ethoxyresorufin as the substrate. The incubation mixture contained the

resorufin substrate (5μM) and 80μM dicumarol diluted in EBSS (Invitrogen) (170). Aliquots (100μL) were taken at 5, 15, 25, and 35 minutes after adding the resorufin mixture, transferred to a 96-well plate and the fluorescence intensity was measured using a SpectraMax M2 microplate reader (excitation wavelength = 530 nm and emission wavelength = 580 nm). Fluorescence intensity was converted to values of concentration by comparison to a standard curve for resorufin fluorescence with concentrations ranging from 0-1000 nM. The rate of resorufin formation (nM/min) was calculated from the early linear increase in the fluorescence curve and defined as cytochrome P450 isoenzyme activity.

2.2.12 Separation of Hepatocytes and LSECs

The cultures were incubated with a 0.1% w/v collagenase solution. The cell suspensions were incubated with Dynabeads (Dynabeads® CD31 Endothelial Cell; Invitrogen) for 20 min at 4°C in an orbital shaker. Dynabead-bound cells (LSEC fractions) were collected by a magnet (DynaMag™-15; Invitrogen) and the supernatants (hepatocyte fractions) were transferred to a new tube. Purity of cell populations was observed to be > 97%. Hepatocyte fractions were centrifuged and diluted in a 0.1% sodium dodecyl sulfate (SDS) solution for measurement of DNA content.

2.2.13 Measurement of DNA Content

Cells were harvested by treatment with a 0.1% collagenase solution and subsequently lysed in a 0.1% sodium dodecyl sulfate (SDS; BioRad, Hercules, CA) solution and stored at −20^{o}C until further analysis. For DNA measurements, aliquots of cell suspensions were treated with a fluorescent DNA-binding dye (Hoechst 33258, pentahydrate-bis-benzimide, Invitrogen). Fluorescence intensity was measured using a SpectraMax M2 microplate reader plate reader (excitation and emission wavelengths were 355 nm and 460 nm, respectively). Fluorescence intensity was converted to DNA concentration by comparison to a standard curve for calf thymus DNA (Sigma-Aldrich) fluorescence with concentrations ranging from 0-40 μg/ml.

2.2.14 Statistical Analysis

All data are reported as mean ± standard deviation. T-tests were conducted to detect differences in the mean values (α =0.05).

2.3 RESULTS

PEMs comprised of 5 up to 30 alternating layers of chitosan and HA were assembled above a confluent layer of primary hepatocytes. The height of the hydrated PEM as well as its modulus and viscosity were determined by QCM-D measurements (166, 168, 169). The film thickness, shear modulus and viscosity of each layer were modeled by following an iterative method using the Voigt model approximation (167), **Table 2.1.** The thickness was found to be approximately 6 nm/PE layer for a PEM consisting of 5 layers. The thickness per PE layer reached a maximum value of 5.2 nm/layer for a PEM of 10 layers. While the reason for the sub-linear growth of film thickness with layer number in the present case is not completely clear, it may be due to the fact that the chitosan was not highly charged at the pH at which it was deposited. The values for shear modulus were initially high due to substrate effects (95.7 ± 66.3 kPa for 5 layers) but decreased as more layers were deposited before increasing again to reach a maximum value (104.5 ± 13.6 kPa) for a PEM comprised of 15 bilayers. The PEM exhibited viscoelastic characteristics and was found to be less rigid as more layers were deposited. The PEM film viscosity values were close to those reported for water indicating a high degree of hydration.

Table 2.1 Thickness, shear modulus and viscosity values for hydrated chitosan/HA PEMs.

Layer	Thickness (nm)	Shear Modulus (kPa)	Film Viscosity (m Pa s)
5	**30.82 ± 6.71**	**95.7 ± 66.3**	**1.69 ± 0.18**
10	**52.27 ± 5.25**	**56.6 ± 17.8**	**1.78 ± 0.09**
15	**55.50 ± 4.18**	**104.5 ± 13.6**	**2.12 ± 0.09**

In the first step towards assembling 3D liver mimics, hepatocyte-PEM cultures were investigated. Urea production and albumin secretion were measured to evaluate the phenotypic function and the results were compared to collagen sandwich cultures (positive control) and hepatocyte monolayers (negative control) (**Figure 2.1**). Over a 7 day period, urea production decreased by 64% and 33% for hepatocyte monolayer and

collagen sandwich cultures respectively. However, urea production increased over the same time period for hepatocytes cultured in the presence of a PEM scaffold. The increase in urea production was found to be 12% and 48% for hepatocyte cultures that had either 5 or 15 PE layers respectively. The values for urea production on day 7 were higher and statistically significant ($p<0.05$) in hepatocyte cultures with 5 (49.1±4.4 $\mu g/10^6$ hepatocytes) or 15 (45.7±3.3 $\mu g/10^6$ hepatocytes) PE layers in comparison to hepatocyte monolayer (36.8±4.6 $\mu g/10^6$ hepatocytes) and were similar and statistically insignificant ($p>0.05$) in comparison to values measured for collagen sandwich (46.7±9.1$\mu g/10^6$ hepatocytes) cultures. In stable hepatocyte cultures, albumin secretion has been shown to increase with time (16, 17). Over a 7-day period, albumin secretion increase by 71% in collagen sandwich cultures and decreased by 50% in monolayer cultures (**Figure 2.2**). Albumin secretion in hepatocyte-PE cultures increased over the 7 day observation period. In hepatocyte cultures with 5 or 15 PE layers, albumin secretion increased by approximately 36% or 7% respectively. Cultures with PEM consisting of 30 or 45 PE layers did not exhibit satisfactory urea or albumin production and were not included in further analyses. The values for albumin secretion on day 7 were higher and statistically significant ($p<0.05$) in hepatocyte cultures with 5 (5.2±1.6 $\mu g/10^6$ hepatocytes) or 15 PE layers (2.8±0.3 $\mu g/10^6$ hepatocytes) in comparison to hepatocyte monolayers (1.8±0.7 $\mu g/10^6$ hepatocytes) and were similar and statistically insignificant ($p>0.05$) in comparison to values measured for collagen sandwich (6.1±0.9 $\mu g/10^6$ hepatocytes) cultures.

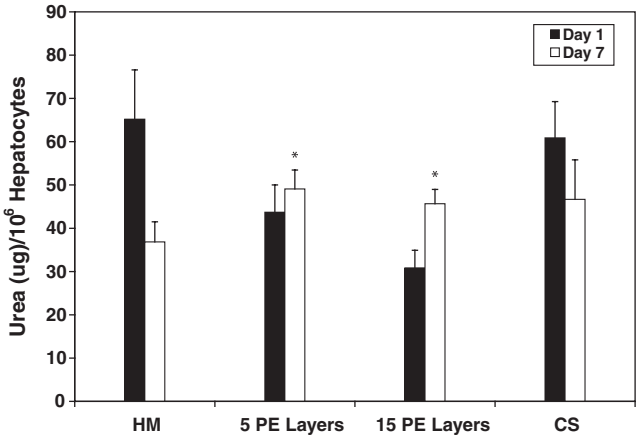

Figure 2.1 Urea production measured over a 7-day period for HM (n = 6), with 5 PE layers (5 PE layers, n = 6), with 15 PE layers (15 PE layers, n = 6), and in a CS (n = 6). *p<0.05 when compared to hepatocyte monolayers on day 7. CS, collagen sandwich; HM, hepatocytes cultured as monolayer.

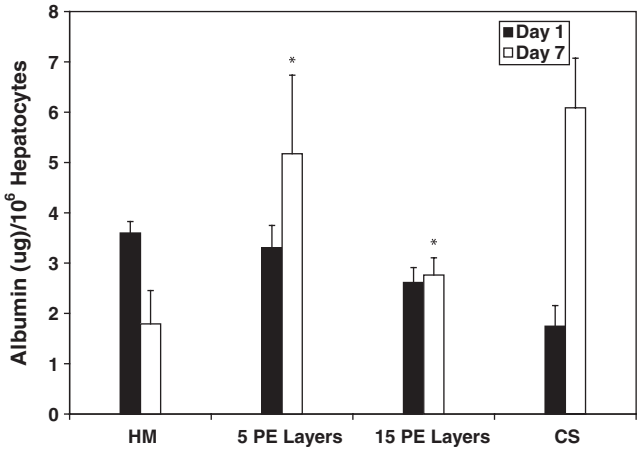

Figure 2.2 Albumin production measured over a 7-day period for HM (n = 6), with 5 PE layers (5 PE layers, n = 6), with 15 PE layers (15 PE layers, n = 6), and in a CS (n = 6). *p<0.05 when compared to hepatocyte monolayers on day 7.

The actin cytoskeletal organization revealed significant differences between hepatocyte monolayers and hepatocyte-PEM cultures. In the absence of rhodamine phalloidin, fluorescence was not observed in hepatocytes, and this was defined as the negative control (**Figure 2.3 A**). Hepatocyte monolayer cultures exhibited a mesh-like network of f-actin through the entire cross-section of the cell (**Figure 2.3 B**). The cytoskeletal organization in hepatocyte-PEM samples was observed to be very similar to hepatocytes cultured in a CS culture (**Figure 2.3 C**). In these cells, f-actin was observed to be

localized only along the peripheral regions of the cell similar to hepatocytes cultured in a CS.

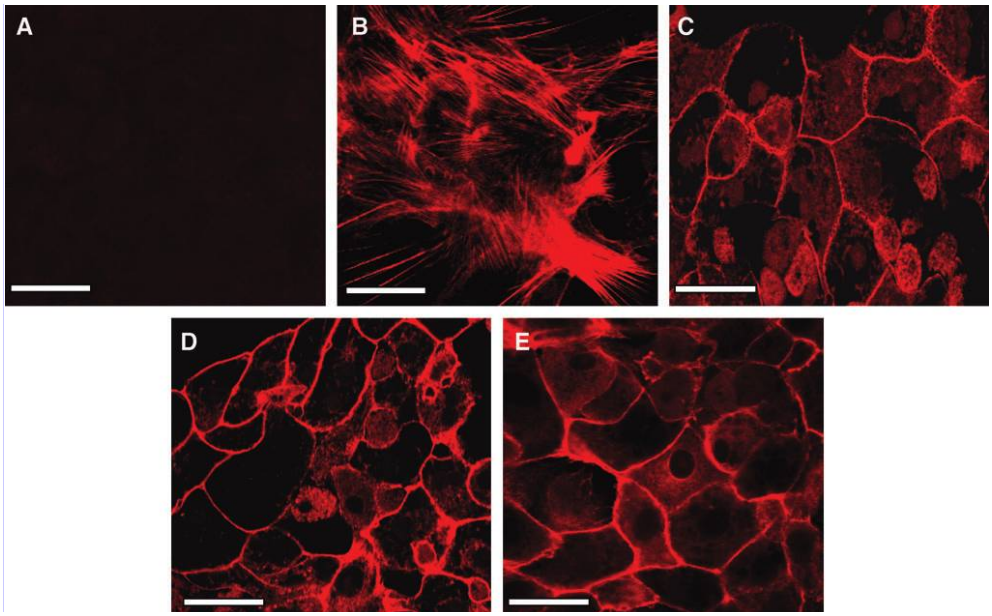

Figure 2.3 Actin cytoskeletal organization in (A) Hepatocyte monolayer without the addition of rhodamine phalloidin (negative control), (B) Hepatocyte monolayer, (C) CS culture, (D) Hepatocytes-5 PE layers, and (E) Hepatocytes-15 PE Layers. Scale bar = 50 µm.

A second layer of LSECs was deposited on hepatocyte-PEM cultures as well as on hepatocyte monolayers (**Figure 2.4**). Images taken 2h post-LSEC seeding indicated that in the absence of an intermediate PE scaffold, LSECs were non-adherent (**Figure 2.4 A**). However, in the presence of the chitosan/HA PEM, LSECs were adherent (**Figure 2.4 B).** These trends prevailed over longer culture periods as well suggesting that the PEM provides a biocompatible surface for LSECs to adhere and proliferate. On day 7, in the absence of the chitosan/HA scaffold, LSECs were not observed above hepatocytes (**Figure 2.4 C**), whereas high concentrations of LSECs were observed on hepatocyte/PE/LSEC constructs **(Figure 2.4 D-F**). It is significant to note that LSECs were adherent only above hepatocytes and were not found in regions between adjacent hepatocyte aggregates (**Figures 2.4 D-F**).

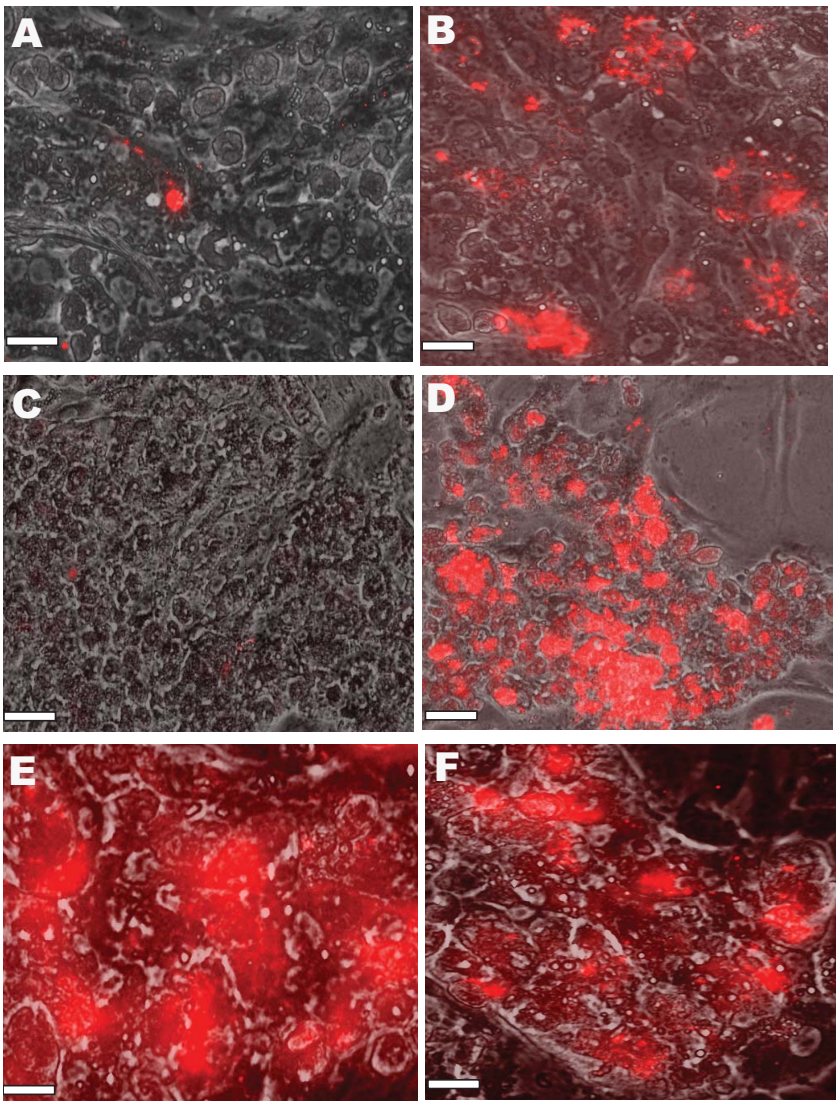

Figure 2.4 Merged phase-contrast (hepatocytes) and red-fluorescent LSECs. Images taken 2 h post-LSEC seeding. (A) Hepatocytes-LSECs and (B) Hepatocytes-5 PE Layers-5000 LSECs. Merged phase-contrast (hepatocytes) and fluorescent (LSECs) images taken 7 days post-LSEC seeding. (C) Hepatocytes-LSECs, (D) Hepatocytes-5 PE Layers-5000 LSECs, (E) Hepatocytes-5 PE Layers-10,000 LSECs, and (F) Hepatocytes-15 PE Layers-5000 LSECs. Scale bar = 100 µm.

The maintenance of LSEC phenotype was assessed by fluorescent imaging of the receptor-mediated uptake of ac-LdL. Since hepatocytes do not have this receptor, these cells did not exhibit any fluorescence **(Figures 2.5 A and B**) as well as LSECs cultured on hepatocytes in the absence of a PEM (**Figure 2.5 C and D**). However, LSECs adherent on hepatocyte-PEM samples exhibited fluorescence thereby, indicating the

endocytosis of the low density lipoprotein (**Figure 2.5 E - H**). These results indicate that LSEC phenotype is maintained in the 3-D constructs.

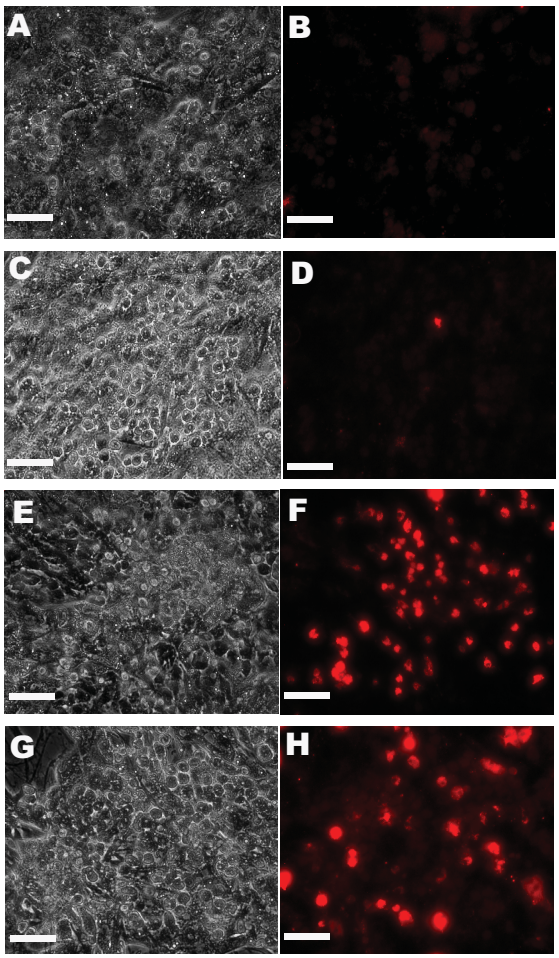

Figure 2.5 Phase-contrast images of (A) LSECs, (C) Hepatocytes, (E) Hepatocyte-LSECs, (G) Hepatocytes-5 PE Layers-5000 LSECs, and (I) Hepatocytes-15 PE Layers-5000 LSECs. Fluorescent images of acetylated low density lipoprotein uptake for (B) LSECs (negative control, in the absence of acetylated low-density lipoprotein), (D) Hepatocytes, (F) Hepatocytes-LSECs, (H) Hepatocytes-5 PE Layers-5000 LSECs, and (J) Hepatocytes-15 PE Layers-5000 LSECs.

On day 7, (**Figure 2.6 A**), albumin secretion in hepatocyte-PEM-LSEC cultures was statistically higher ($p<0.05$) in comparison to hepatocyte monolayers. The p-values for hepatocyte-5L-5000 LSECs, hepatocyte-5L-10,000 LSECs, and hepatocyte-15L-5000 LSECs were found to be 0.04, 0.006, and 0.015, respectively. Samples containing LSECs in the presence of a PE interface exhibited statistically higher albumin secretion compared with hepatocyte-LSEC cultures. The p-values for hepatocyte-5L-10,000 LSECs and hepatocyte-15L-5000 LSECs were found to be 0.039 and 0.03, respectively,

when compared to albumin production in the absence of a PE multilayer. However, the albumin secretion for all 3D liver mimics was found to be similar to CS cultures and the values were statistically insignificant. Urea production decreased over the 7-day period for all samples. Hepatocytes cultured as a monolayer sample exhibited ~70% decrease in urea production over a 7-day period (**Figure 2.6 B**). The decrease in the hepatocyte-PEM-LSEC samples was ~40%-45% and similar to the decrease observed in CS cultures.

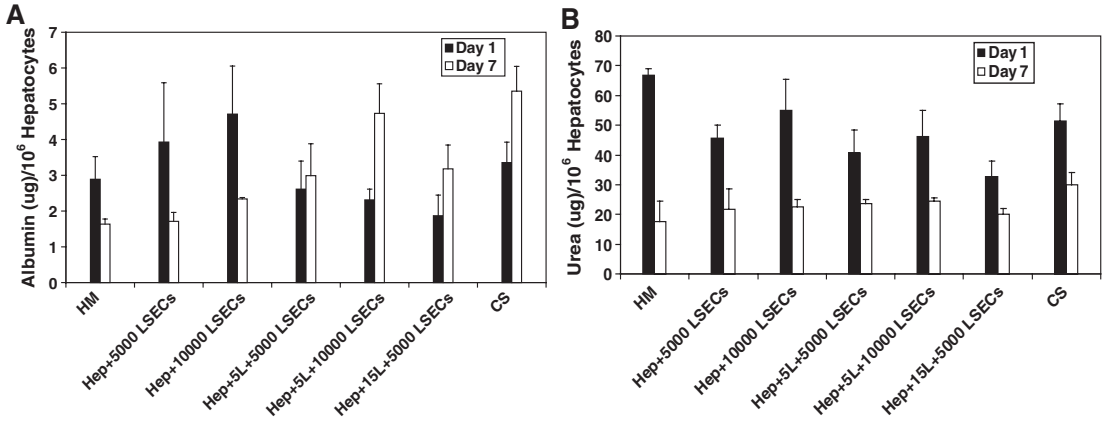

Figure 2.6 Albumin secretion (A) and urea production (B) measured over a 7-day period for HM, with LSECs in the absence of a PEM (Hep+5000 LSECs and Hep+10,000 LSECs), with LSECs in the presence of a PEM (Hep+5L+5000 LSECs, Hep+5L+10,000 LSECs, and Hep+15L+5000 LSECs) and in a CS (n = 3 for all conditions.

An important differentiated function of hepatocytes is the presence of bile canaliculi, the channels through which bile acids are transported from the liver (171, 172). The presence of canaliculi was determined through the localization of a fluorescent DPP IV enzyme. These structures were not present in hepatocyte monolayers and hepatocyte-LSEC cultures (**Figures 2.7 A and C**). These structures were better defined in hepatocyte-PEM cultures (**Figure 2.7 D**). However, well defined bile canaliculi were observed in hepatocyte-PEM-LSEC (**Figures 2.7 E, F**) and collagen sandwich cultures (**Figure 2.7 B)**. These results suggest that the PEM plays an important role in maintaining cellular polarity and in modulating the heterotypic interactions between hepatocytes and LSECs.

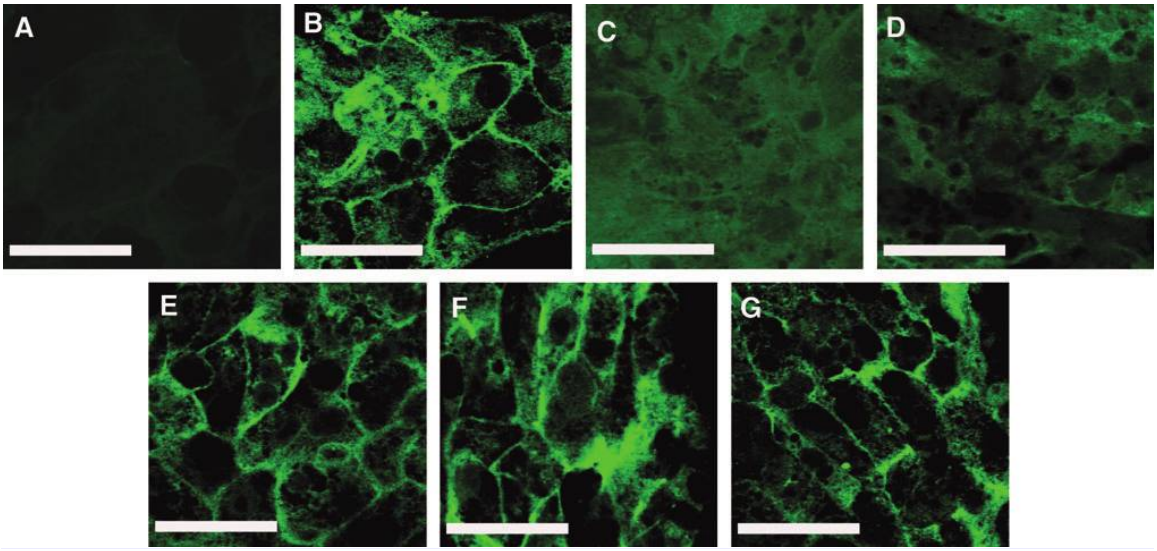

Figure 2.7 Di-peptyl peptidase IV immunostaining for bile canaliculi measured 3 days post-LSEC seeding. (A) Negative control (CS culture in the absence of antibodies), (B) CS culture, (C) Hepatocyte monolayer, (D) Hepatocytes+5000 LSECs, (E) Hepatocytes+15 PE Layers, (F) Hepatocytes+15 PE+5000 LSECs, and (G) Hepatocytes+15 PE+10,000 LSECs. Scale bar = 50 µm.

CYP1A1/2 isoenzyme activity was monitored over a 7-day period since the metabolism of toxins, an important phenotypic function of hepatocytes, is mediated through the CYP class of microsomal enzymes. CYP1A1/2 activity remained stable in hepatocyte-PEM samples and exhibited a 2-fold increase in collagen sandwich cultures. A significant increase was observed only in hepatocyte-PEM-LSEC constructs where the fold increase over the observation period ranged from 4-fold up to 16-fold (**Figure 2.8**). 3-D liver mimics that contained 10,000 of LSECs exhibited either 7.5-fold (hepatocyte-5 PE Layers-10000 LSECs) or a 16-fold increase (hepatocyte-15 PE Layers-10000 LSECs. These trends suggest that the communications and interactions between these two cells types are critical for enhancing the detoxification capability of hepatocytes *in vitro*.

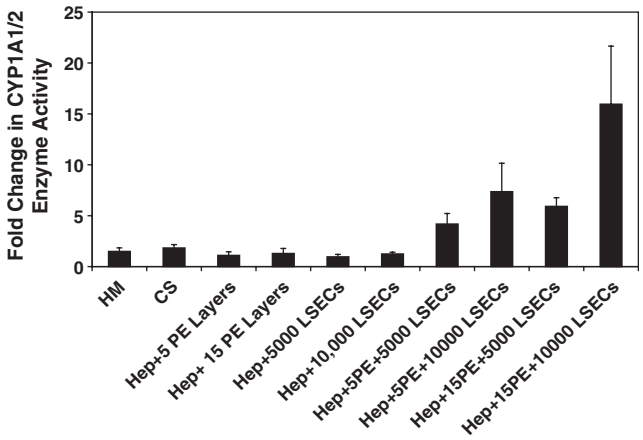

Figure 2.8 Fold change in CYP1A1/2 enzyme activity for HM and CS, with PEMs only, with LSECs only, and in three-dimensional liver mimics (n = 3 for all conditions).

2.4 DISCUSSION AND CONCLUSIONS

The design of 3-D structures of hepatic parenchymal and non-parenchymal cells using PE scaffolds is an innovative approach to mimic liver sinusoidal structure found *in vivo*. Although hepatocytes cultured in a collagen sandwich configuration are stable over extended periods of time, they do not resemble liver architecture *in vivo*. Additionally, the presence of thick collagen gels prevents the assembly of 3-D stratified cellular constructs. LSECs have been shown to function as a scavenger system *in vivo*, by playing a vital role in the balance of lipids, cholesterol and vitamins (19, 21, 25, 173, 174). Through blood clearance LSECs can remove waste macromolecules that are either soluble or colloidal in nature. Several components of connective tissue are eliminated rapidly from the blood through receptor-mediated endocytosis in LSECs.

Chitosan-HA PEMs exhibited shear modulus values that are in the range reported for the bulk modulus values of the liver (152, 153). PEMs exhibiting elastic moduli in the 100kPa range have been shown to maintain and modulate hepatic phenotype suggesting that the shear modulus values reported in this study are suitable for the assembly of liver sinusoidal mimics (139). The films are well hydrated, thereby, promoting the diffusion of small molecules such as cytokine and other signaling molecules. Hepatocyte-PEM cultures with either 5 or 15 PE layers were found to exhibit urea and albumin production similar to collagen sandwich cultures. This is of importance, since the height of the PEM ranges from 30-55nm, which is significantly lower than the thickness of a collagen gel (in the mm range). It is hypothesized that that height of the PEM decreases slightly due to the formation of chitosan aggregates (175, 176). These data suggest that cellular polarization, an important feature of hepatocytes cultured in collagen sandwich cultures, occurs even in the presence of a nano-scale PEM. Furthermore, the nano-scale dimensions of the PEM offer the potential to promote and control homotypic and heterotypic cellular interactions.

The chitosan-HA PEM provides a surface for LSECs to adhere and proliferate. LSECs were found to adhere only on hepatocytes in the presence of a PEM and were non-

adherent in the absence of PEMs or in regions adjacent to hepatocyte aggregates. Hepatic phenotypic features such as bile canaliculi were well defined in hepatocyte-PEM-LSEC samples in comparison to hepatocyte monolayers or hepatocyte-LSEC cultures, thereby suggesting enhanced autocrine/paracrine signaling through the PEM. Cytochrome P450, CYP1A1/2 activity was enhanced up to 16-fold over a 7 day period in hepatocyte-PEM-LSEC cultures. These observations suggest that the hepatocyte-PEM-LSEC constructs could provide a more physiologically relevant model system to study the metabolism of drugs and toxins. In the future, our goal is to investigate the enzyme kinetics of CYP3A which accounts for the metabolism of approximately 50% of pharmaceuticals available today (177, 178) as well as the CYP2B and CYP2C family of enzymes, implicated in the metabolism of amphetamines and anti-inflammatory agents (179, 180). The modes through which hepatic parenchymal and non-parenchymal cells communicate remain cryptic. Through detailed studies on profiling cytokine levels as well through gene expression studies, our future goals are to unearth molecular signatures and the key signaling molecules that enhance cell-cell communications in hepatic architectures.

Some alternate approaches to design hepatic structures are the use of a temperature-responsive polymer such as N-isopropyl acrylamide (57, 163, 181), the use of cationic magnetic liposome (164), and the use of laser guided writing techniques (40, 162). In the first two approaches, issues related to working with cell sheets and the long-term effects of magnetic liposomes pose problems. Although laser-guided writing techniques are a promising approach, the design of large 3D liver models could potentially be time consuming. More recently, studies on perfused cocultures of primary hepatocytes and LSECs reveal that such systems can maintain LSEC phenotype (174). Our approach to design 3D liver mimics through the incorporation of PEMs and hepatic cells is a simple and effective methodology. The PEMs used in this study are biocompatible and biodegradable and do not affect hepatic phenotype. In the future, the PEMs can be modified with hepatocyte-specific adhesive ligands to promote receptor-mediated adhesion. Cellular constructs that mimic liver sinusoidal structure in vivo could aid in the design of liver-assist devices and provide accurate models for applications in toxicity and drug testing. Since LSECs are the first barrier to blood-borne pathogens in the liver,

tissue mimics that incorporate these cells could play a vital role in advancing our knowledge on the communications and signaling between hepatic parenchymal and non-parenchymal cells.

Chapter 3. Published in Biomacromolecules.

Larkin AL, Davis RM, Rajagopalan P. Biocompatible, Detachable, and Free-Standing Polyelectrolyte Multilayer Films. Biomacromolecules 2010; 11 (10): 2788-96. *Reprinted with permission from Biomacromolecules*.

Chapter 3. Biocompatible, Detachable, and Free-standing Polyelectrolyte Multilayer Films

3.1 INTRODUCTION

Polyelectrolyte multilayers (PEMs) have gained tremendous popularity due to the ease and versatility in assembling such films (63, 64, 98, 182-185). Due to the precise control that can be exerted over film properties, PEMs have been investigated for a multitude of different uses including drug delivery, nano-fluidic devices, modulating cellular adhesion, anti-bacterial coatings and hepatic tissue engineering (68, 69, 72, 74, 120, 121, 137, 186-191). To date, most PEMs that have been assembled, are adherent on an underlying substrate and cannot be detached. In a majority of the reports in the literature, the substrate on which the PEM is deposited is designed to interact *via* ionic bonding with the cationic or anionic polyelectrolyte (PE). Therefore, the self-assembled multilayer cannot be detached without significantly rupturing or degrading the film. This prevents the use of PEMs in applications that necessitate free-standing films such as biomaterials (192), biomimetic membranes (193), scaffolds for tissue engineering (117), and drug delivery (194). Since PEMs can be assembled from virtually any combination of oppositely charged PEs, are inherently versatile, and exhibit several properties that are applicable to diverse research foci, there is a critical need to design robust, stable, non-degrading, free-standing detachable films. In addition, to enhance the use of detachable PEMs as biomaterials, they must be designed to be compatible with live cells.

Despite their myriad applications, fabricating free-standing self-assembled multilayers has proven to be difficult (95, 116, 194-204). Approaches used to design detachable PEMs include the presence of sacrificial layers, the dissolution of initial layers in the self-assembled multilayer, and through the neutralization of charged layers (95, 116, 195-201). Some potential disadvantages of these approaches are the changes, both chemical and physical, that the films undergo during the post-processing steps in order to separate the film from the underlying substrate. These include the introduction of defects, increasing surface roughness, and tears into the PEMs. More recently, the use of hydrophobic substrates to assemble free-standing PEMs was reported (202, 203). In this study, free-standing films comprised of poly (ethylene oxide) and poly (acrylic acid)

were deposited on hydrophobic substrates such as Teflon™ and poly (propylene). Due to the weak van der Waal's interactions between the polymer multilayers and the substrate, as well as hydrogen bonding mediated between poly (ethylene oxide) and poly (acrylic acid), the films could be peeled easily and were observed to be free of defects. Free-standing nanoporous films have also been assembled using a combination of spin-coating and hydrophobic substrates (194, 204). However, these reports have not investigated properties of the PEMs that are critical in their use as biomaterials, such as long-term stability in aqueous solutions, optical transparency, and cellular response. Detachable and free-standing PEMs exhibit significant potential for use in tissue engineering applications, specifically, in the design of scaffolds and biomimetic membranes (137, 205). Since we can modify the chemical and physical properties of the PEMs prior to bringing them in contact with cells, detachable PEMs can be used with a wide range of reaction chemistries.

We report a simple and versatile approach for the fabrication of novel, biocompatible, free-standing PEMs obtained through the sequential and alternate deposition of anionic (hyaluronic acid, HA) and cationic (chitosan) PEs on an inert, hydrophobic poly(propylene) substrate. *To the best of our knowledge, this is the first report on the fabrication of detachable and free-standing PEMs that are biocompatible, composed purely of polyelectrolytes, optically transparent, stable in aqueous solutions and do not require post-assembly modifications to enable detachment*. These PEMs are biocompatible since they are comprised of chitosan and HA, which are PEs derived from polysaccharides, used in cell and tissue engineering applications (70, 85, 86, 141, 143, 144, 206, 207). HA is found in the basal membrane of connective tissues and has been used as a surface to support cell-cultures (70, 86, 144). Chitosan is obtained from the shells of crustaceans and has been used in cell-based applications due to its compatibility with a variety of cell types (85, 141, 206, 207).

In the present study, detachable and free-standing PEMs comprised of HA and chitosan were obtained ranging in thickness from 1.8 to 3.6 μm. The long-term stability of the PEMs under physiologically relevant conditions was monitored to determine their

efficacy in biological applications. The physical and chemical properties of the PEMs were systematically investigated to obtain comprehensive information on the surface and bulk chemical composition of the PEMs, their surface topography, and their mechanical properties. Measurement of the optical properties of the PEMs in the 400–900 nm range demonstrated their transparency. The interactions between cells and the free-standing detachable PEMs were determined through a combination of studies such as cell viability, proliferation, and cytoskeletal organization.

3.2 MATERIALS AND METHODS

3.2.1 Materials

Chitosan (Mw ≈ 350 kDa), bovine serum albumin, and glutaraldehyde (GA) were obtained from Sigma-Aldrich (St. Louis, MO). Hyaluronic acid (HA, Mw ≈ 750kDa), and acetic acid were obtained from Fluka (St. Louis, MO). Phosphate buffered saline (PBS; 137 mM NaCl, 2.7 mM KCl, 10mM Na_2HPO_4, 1.76 mM KH_2PO_4), Dulbecco's Modified Eagle Medium (DMEM), and Penicillin-Streptomycin (Pen-Strep), were obtained from Invitrogen Life Technologies (Carlsbad, CA). Bovine calf serum (BCS) was obtained from Hyclone (Logan, UT). Unless noted otherwise, all other chemicals were obtained and used as received from Fisher Scientific (Pittsburgh, PA).

3.2.2 Fabrication of Detachable and Free-standing PEMs

HA and chitosan were used as the anionic and cationic polyelectrolytes (PEs) in order to assemble the detachable polyelectrolyte multilayers (PEMs). HA solutions were prepared in 18 MΩ cm Picopure water (Hydro, Raleigh NC) and chitosan solutions were prepared in 1 % v/v acetic acid. Solution concentrations ranged from 1 to 5 mM (based on repeat unit molecular weight of the polymer, i.e. 340.3 g mol^{-1} and 874.7 g mol^{-1} for chitosan and HA respectively). The solutions were filtered through 0.45 μm polyethersulfone filters (Nalgene, Rochester NY). The pH of HA and chitosan solutions was maintained at 4.0 and 5.0 respectively. HA-chitosan PEM films were assembled on inert, hydrophobic poly (propylene) (PP, McMaster-Carr, Princeton, NJ) substrates using a robotic deposition system (NanoStrata, Gainesville, FL). The PP substrates were cleaned by sonication in acetone. The hydrophobicity was determined using static water contact angle measurements (KSV Instruments, Helsinki, Finland). Clean PP substrates exhibited an average water contact angle of 103.2 ± 2.8° (averaged over fifteen measurements per sample). In order to vary PEM properties, the deposition time per PE was varied from 10 to 20 min. PEMs were assembled by first depositing an anionic PE (HA) followed by the cationic PE (chitosan). The desired number of bilayers, ranging from 20-50, was obtained through the sequential and alternate deposition of PE layers. A bilayer (BL) is defined as one cationic and one anionic PE. The PEM assemblies were

rinsed for 4 min in a water bath adjusted to pH 4.5 between PE depositions. The typical assembly time for a 50 BL HA-chitosan film was 40 h. Prior to PEM detachment, the films were dried overnight in air and peeled from the underlying hydrophobic substrate using tweezers. Films reported as detachable peeled with ease and were found to be free of defects. Films which exhibited delamination and stress-cracking, with little to no control over detachability, were noted as detachable but not reproducible or robust. Films that did not detach from their substrate were noted as non-detachable. In order to promote the stability of the PEMs in solution, the films were lightly cross-linked before detachment by exposure to a solution containing 8 % w/v GA (124, 208). The exposure time to the crosslinker, was varied from 1 to 2 minutes to vary the degree of crosslinking. The PEM films were subsequently air-dried and stored at room temperature until further use.

3.2.3 Film Stability

Detachable HA-chitosan PEM films were placed in PBS at 37ºC and monitored over a 7 day period. On day 7, the PEMs were dried under vacuum at 50°C for 24h. The weight of the detachable PEMs was measured prior to and subsequent to exposure to PBS to determine the extent of degradation or loss in weight.

3.2.4 Profilometry

A Veeco Dektak 150 (Veeco Metrology, Santa Barbara CA) profiler was used to determine the dry and hydrated thickness of the detachable PEMs. Scan lengths for each sample were maintained at 1000 μm. The thickness values reported were averaged over 7 to 15 measurements per sample. For measurements under hydrated conditions, PEMs were maintained in 1X PBS for 24h, the excess water was wicked from the sample and measurements were performed within five minutes to prevent dehydration.

3.2.5 Optical Properties

The optical transmission in the 400-900 nm range was measured on a UV/vis spectrophotometer (Perkin Elmer Lambda 25, Downers Grove IL). Optical transparency was measured for both dry and hydrated HA-chitosan films. For hydrated PEM

measurements, PEMs were maintained in 1X PBS for 24 h prior to measurement, the excess water was wicked from the sample and measurements were performed within five minutes to prevent dehydration.

3.2.6 Atomic Force Microscopy (AFM)

The surface topography of the detachable PEMs was measured on an AFM (Veeco Multimode AFM, Santa Barbara CA). Surface roughness of dry unmodified and cross-linked PEMs was determined using silicon nitride DNP tips with a spring constant of 0.12 N/m (Veeco, Santa Barbara CA) in contact mode at a scanning rate of 2 Hz. Surface features, specifically, peak to valley heights were measured using Nanoscope® software (Veeco).

3.2.7 Nano-indentation

The Young's modulus of unmodified and cross-linked PEMs was measured using a nano-indenter (Triboindenter, Hysitron Inc., Minneapolis MN) equipped with a 90° cono-spherical indenter tip. The tip was non-imaging with a radius of approximately 10 μm. The nano-indenter was operated under a controlled load while sensing tip displacement. The measured tip drift rate was observed to be less than 0.40 nm/s. Indentation tests were performed on the HA side of the detachable films for both crosslinked and unmodified films. The PEMs were fixed to an aluminum substrate with carbon tape. For each film, nine indentations were performed with a peak load of 300 μN. Measurements were performed under ambient conditions.

Force is denoted as P and displacement by h. Force-displacement ($P - h$) curves were generated by nano-indentation using a programmed load function. The load function was increased linearly from 0 μN to 300 μN over 10s then decreased back to 0 μN. The retraction of the tip from the material was used to calculate the mechanical properties of the sample according the method proposed by Oliver and Pharr (209). The reduced modulus, E_r, and sample hardness, H, were defined by the following equations.

$$\frac{1}{E_r} = \frac{(1-\upsilon^2)}{E} + \frac{(1-\upsilon_t^{\,2})}{E_t} \qquad (1)$$

$$H = \frac{P_{\max}}{A} \qquad (2)$$

E and υ are defined as the Young's modulus and Poisson's ratio of the sample. E_t and υ_t are the Young's modulus and Poisson's ratio of the indenter tip. These values, E_t = 1140 GPa and υ_t = 0.07 were supplied by the manufacturer. In a previous study, where nano-indentation was utilized to determine the properties of dry and rigid poly (allylamine hydrochloride)-poly (styrenesulfonate) PEMs, the Poisson's ratio υ was assumed to be 0.33 in equation (1) (210). The peak indentation load and projected area at the peak indentation load were denoted as P_{max} and A respectively. The experimental stiffness, S, was defined as the slope of the retraction curve at the maximum displacement, and was related to the reduced modulus by equation (3).

$$S = \frac{dP}{dH} = \frac{2}{\sqrt{\pi}} E_r \beta \sqrt{A} \qquad (3)$$

Equation (3) was derived for a half-space (211). In order to prevent substrate effects, the each indentation was conducted carefully to ensure that the depth was significantly lower than the overall thickness of the PEM (211, 212). Reduced indentation depths prevented stress fields generated during indentation from reaching the underlying substrate (211-213). In our studies the indentation depth was maintained at approximately 10% of dry PEM thickness for crosslinked films and up to 20% for the unmodified samples. Cohen et al. indented poly (allylamine hydrochloride)/poly(acrylic acid) PEMs of varying thicknesses, ranging from 80 nm to 6 microns (212). The reduced modulus exhibited negligible substrate effects at contact depths up to 40% of the overall film thickness (212).

In equation (3), β was a prefactor assumed to be 1 (212). Triboscan 8 software (Hysitron) was used to calculate S from the unloading segment of the $P - h$ curves. The area of contact was determined by calibration of the tip with a known fused quartz reference. To determine A, the contact depth, h_c, was related to A by the tip calibration function in equation (4).

$$A = C_0 h_c^{\,2} + C_1 h_c + C_2 \sqrt{h_c} \qquad (4)$$

The values of C_0, C_1 and C_2 were determined empirically using $P - h$ curves generated by the nano-indentation of a fused quartz reference and h_c is defined in equation (5).

$$h_c = h_{\max} - \varepsilon \frac{P_{\max}}{S} \qquad (5)$$

ε is the geometric constant for the indenter tip which was taken as 0.75 (210, 212). After substitution and rearrangement of equations 1-5, the Young's modulus, E, of the sample was related to the E_r by equation (6) where B_1 and B_2 are constants.

$$E = \frac{B_1}{\frac{1}{E_r} - B_2} \qquad (6)$$

3.2.8 Cell Culture

Cross-linked PEMs were rinsed for a total period of 48h to remove any residual glutaraldehyde. In the first 24h period, the PEMs were rinsed with 1X PBS and the solution was changed every 4h. On the second day, the samples were rinsed in fibroblast culture medium and the solution was changed every 4h. Subsequent to rinsing they were sterilized under germicidal UV radiation for 1 hour, and maintained in fibroblast culture medium until used. BALB/c 3T3 mouse embryo fibroblasts (American Type Cell Culture, Manassas VA) were maintained in DMEM supplemented with 10% v/v BCS and 5% v/v Penn-Strep. Fibroblast cultures were maintained in T-75 flasks (BD Biosciences, San Jose CA) at 37°C in a humidified gas mixture of 95% air/ 5% CO_2.

3.2.9 Cell Viability

Fibroblasts cultured on detachable PEMs were rinsed in warm 1X PBS and exposed to a mixture of calcein-AM and ethidium bromide (Live Dead Cytotoxicity kit, Invitrogen Life Technologies). The cells were imaged on a Nikon TE-2000 (Nikon, USA) inverted microscope equipped with 4x, 10x, 20x and 40x phase objectives and a motorized stage (Prior Scientific, USA). Phase-contrast and fluorescent images were collected using a Hamamatsu CCD camera (Hamamatsu City, Japan) and Nikon Elements© (Nikon, USA) software. Fibroblasts that fluoresced red (due to the incorporation of ethidium bromide)

were scored as dead and green fluorescent cells (due to the incorporation of calcein-AM) were scored as live.

3.2.10 Cellular Proliferation Studies

Fibroblasts were seeded on PEMs at an initial density of 200,000 cells per cm^2. Cell proliferation was measured with a non-destructive imaging method. Phase-contrast microscopy was used at 10x magnification to capture images of the cells. For each sample, a minimum of fifteen random locations were imaged every 24 h up to six days, to analyze the degree of proliferation.

3.2.11 Actin Cytoskeletal Imaging

A 0.8% glutaraldehyde (v/v, Electron Microscopy Sciences, Hatfield PA) solution in PBS was used to fix fibroblasts cultured on PEM surfaces 24h after cell seeding. Cells were exposed to this solution for approximately fifteen minutes. A 0.1% Triton X-100 (Sigma-Aldrich) solution was added for five minutes to permeabilize the cell membrane. Next, rhodamine phalloidin (Invitrogen Life Technologies) diluted in a 1% (w/v) bovine serum albumin solution in PBS was added and samples were incubated at 37ºC for a 3h period.

3.2.12 Statistical Analysis

Statistical significance and p values for cell proliferation between sample groups were determined by t-test analysis with alpha set to 0.05. All data are reported as mean ± standard deviation. n denotes sample size.

3.3 RESULTS

HA (anionic) and chitosan (cationic), both weak PEs, were sequentially adsorbed on inert, hydrophobic PP substrates to assemble HA-chitosan PEMs that were detachable and free-standing. Negatively charged HA was initially adsorbed to the hydrophobic substrate through van der Waals interactions followed by the adsorption of cationic chitosan. The alternate and sequential deposition of HA and chitosan solutions resulted in the formation of highly interdigitated PE layers bound by electrostatic interactions [1] (**Figure 3.1 A**). The weak nature of the forces between the initial HA layer and the hydrophobic PP substrate, enabled the detachment of the PEMs (202, 203). The ease of detachment as well as the quality of HA-chitosan PEMs were investigated as a function of the number of bilayers and the deposition conditions. The parameters that were investigated were the deposition time per PE as well the concentration of the PE solutions (**Table 3.1**). At lower numbers of bilayers (ranging from 20-25), the PEMs were not detachable resulting in significantly ruptured films. PEMs comprised of 30 bilayers or more, resulted in free-standing films. However, at lower values of PE deposition time (10 minutes) these films were not free of defects or tears. Free standing PEMs comprised of 30 or 50 bilayers were obtained only when the PE deposition time was maintained at 20 minutes per PE layer and at 1mM PE solution concentration. Under these conditions, the average thickness of air-dried films was found to be 1804 ± 199 nm (n = 13, 30 bilayers) or 561 ± 272 nm (n = 15, 50 bilayers). When the free-standing PEMs were assembled from 30 bilayers, they were not very robust and were difficult to handle in subsequent experimentation. In contrast, detachable PEMs comprised of 50 bilayers were easy to handle and, therefore, used in further studies (**Figure 3.1 B** and **C**).

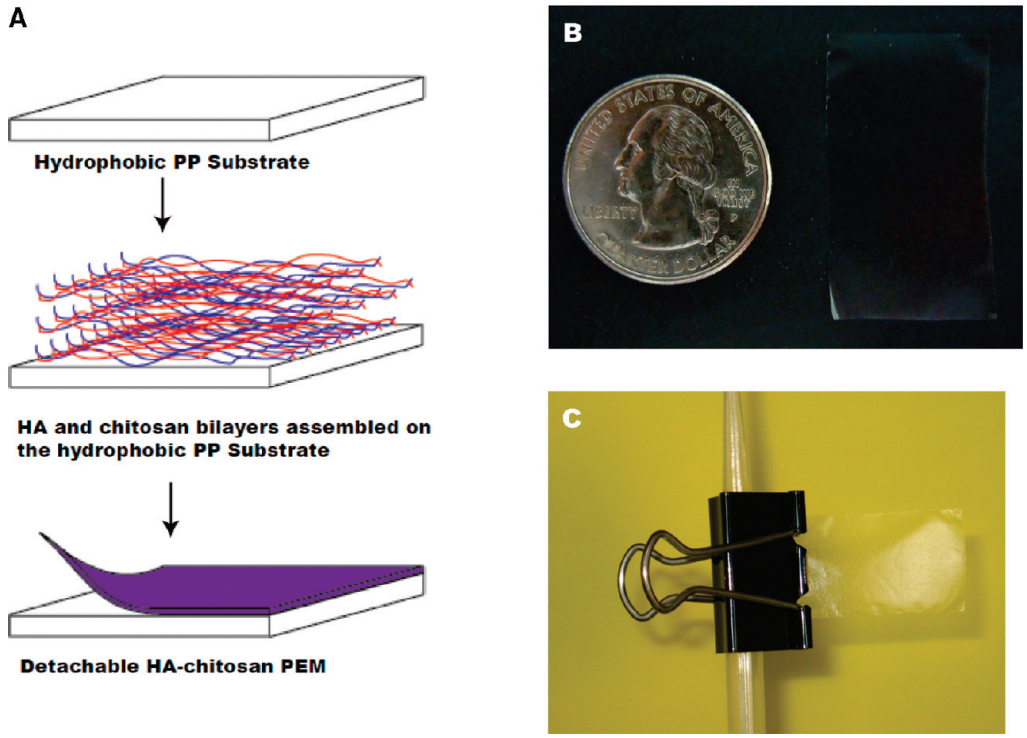

Figure 3.1 (A) Schematic for the fabrication of detachable, free-standing HA-chitosan PEMs. (B) Detachable 50BL chitosan-HA PEM. (C) Detachable 50BL chitosan-HA PEM.

Table 3.1 Deposition conditions varied in the fabrication of detachable, free-standing HA-chitosan PEMs and the quality of the resultant PEMs.

Number of Bilayers	PE Deposition Time (min)	[PE] mM	Detachability
20	20	1	No
25	20	1	No
30	20	1	Yes, Not Robust
50	10	1	No
50	10	2.5	Yes, Not Robust
50	10	5	Yes, Not Robust
50	15	1	Yes, Not Robust
50	20	1	Yes, Robust

An important feature of the free-standing PEMs, which is essential for biological applications, is their stability when exposed to aqueous solutions. When PEMs comprised of 50 bilayers were placed in PBS, they rapidly disintegrated and exhibited greater than 90% loss in weight within 5 minutes. To improve their stability, the films were cross-linked with glutaraldehyde (GA). This approach offered a simple route to covalently crosslink amine groups in the HA-chitosan PEMs (123, 124, 208). The PEMs were crosslinked upon exposure to a GA solution (8% w/v) for 1 and 2 minute periods prior to detachment. Cross-linking with GA did not affect detachability under any of the conditions listed in **Table 3.1**. PEMs that were neither robust nor detachable when unmodified exhibited identical behavior upon cross-linking. When the cross-linked PEMs were placed in PBS at 37°C, the weight loss over a seven-day period was observed to be less than 8% (**Figure 3.2**). Specifically, the retention in weight was found to be 92.2 ± 5.9% (n = 3) and 96.0 ± 2.9% (n = 3) for the 1 and 2 minute cross-linked PEMs respectively.

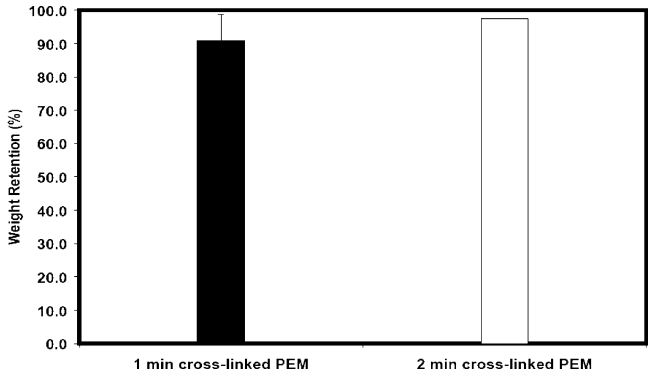

Figure 3.2 Retention in weight for cross-linked PEMs maintained at 37 °C and in PBS over a seven-day period.

The thickness of the unmodified and cross-linked PEMs under dry and hydrated conditions was measured using profilometry. Under hydrated conditions, the film thickness was found to increase 2-fold (**Table 3.2**). Crosslinking PEMs with glutaraldehyde resulted in no major changes in the bulk composition of the PEM (**Figure 3.8**). An imine vibration band near 1635 cm^{-1} indicated successful cross-linking of amine groups within the PEM (214). XPS studies revealed no significant changes in the surface composition between unmodified and cross-linked PEMs (**Figure 3.9**).

Table 3.2 Thickness of dry and hydrated HA-chitosan PEMs.

	Unmodified PEM	**Cross-linked PEM (1 minute)**	**Cross-linked PEM (2 minutes)**
Dry	3561 ± 272 nm (n = 15)	3437 ± 272 nm (n = 15)	3542 ± 141 nm (n = 10)
Hydrated	N/A	8280 ± 307 nm (n = 7)	7947 ± 245 nm (n = 7)

An important property of the detachable HA-chitosan PEMs for incorporating them as biomaterials and in tissue-engineered constructs is their ability to transmit light. When PEMs are used as substrates for cell culture, the transmission of light is critical for imaging and fluorescence microscopy. The transmission of visible light (400 to 900 nm) under dry and hydrated conditions was measured for unmodified, and cross-linked HA-chitosan PEM films (**Figure 3.3**). In the dry state, for the unmodified PEMs, the transmission was found to range between 47 to 58%. Due to the rapid degradation of the unmodified films in the presence of aqueous solutions, their optical properties under hydration could not be measured. Similar values were obtained for the dry cross-linked PEMs. In contrast, under hydrated conditions, the detachable PEMs were virtually transparent. For example, a PEM cross-linked for one minute exhibited 51-62% transmission in the dry state and 92-98% under hydrated conditions (**Figure 3.3A**). Virtually identical trends were observed for PEMs cross-linked for 2 minutes (**Figure 3.3B**). At lower wavelengths, the small decrease in percent transmission was attributed to scattering (**Figure 3.3A** and **B**).

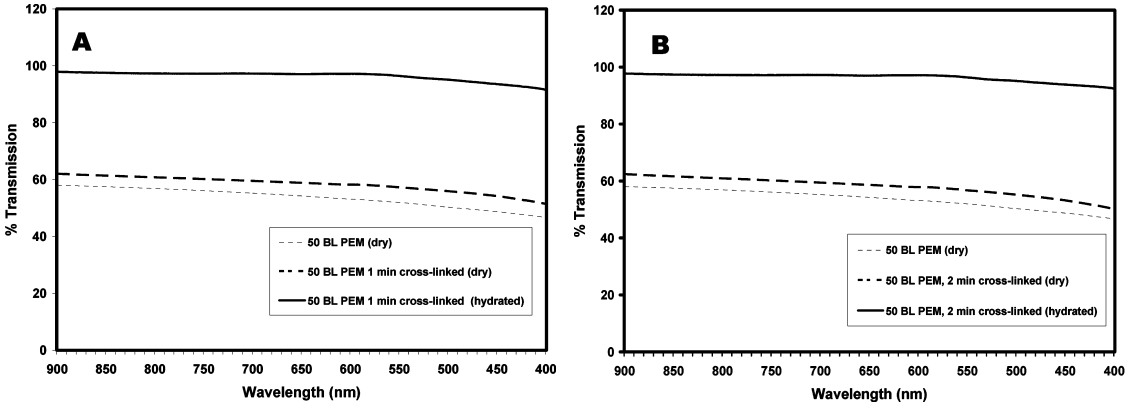

Figure 3.3 Optical transmission in the 400 – 900 nm range for dry 50BL HA-chitosan and hydrated 50BL HA-chitosan PEMs: (A) cross-linked for 1 min; (B) cross-linked for 2 min.

The surface topography of unmodified and cross-linked PEMs was measured since cross-linking can potentially impart roughness to a PEM surface (82, 215, 216). It is well known that surface roughness can play a role in modulating cellular response (137, 217, 218). The surface topography of the unmodified, and cross-linked free-standing PEMs was investigated using AFM in contact mode. The unmodified PEM surface was smooth with nanoscale surface features that exhibited an average peak to valley height of 5.55 ± 1.02 nm (**Figure 3.4A**). The peak to valley height or the average surface roughness increased to 6.17 ± 1.01 nm for a PEM cross-linked for 1 minute (**Figure 3.4B**) and to 7.84 ± 1.36 nm for a PEM cross-linked for 2 minutes (**Figure 3.4C**).

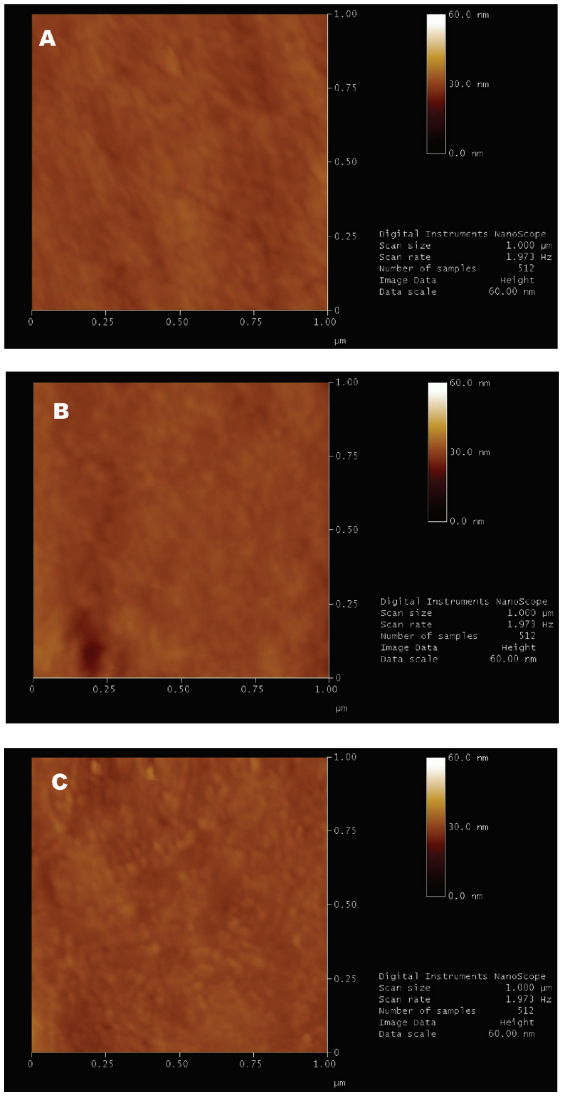

Figure 3.4 AFM Images (1 x 1 µm) of a 50BL HA-chitosan PEM: (A) unmodified, (B) cross-linked for 1 min, and (C) cross-linked for 2 min.

Nano-indentation was used to study the mechanical properties, specifically, the Young's modulus, of the unmodified and cross-linked PEMs. Each sample was probed at nine different locations and the average modulus was calculated. A set of representative force-displacement curves for unmodified, 1 minute and 2 minute cross-linked PEMs are shown in **Figure 3.5**. These trends demonstrate the changes in modulus upon cross-linking. Unmodified PEMs exhibited an average Young's modulus value of 90.9 ± 38.3 MPa (**Table 3.3**). The Young's modulus values increased to 309.7 ± 42.6 MPa and 477.7 ± 33.3 MPa for 1 and 2 minute cross-linked PEMs respectively. These trends and values

were similar to prior studies conducted on PEMs comprised of poly (acrylic acid) and poly(allylamine hydrochloride) (212).

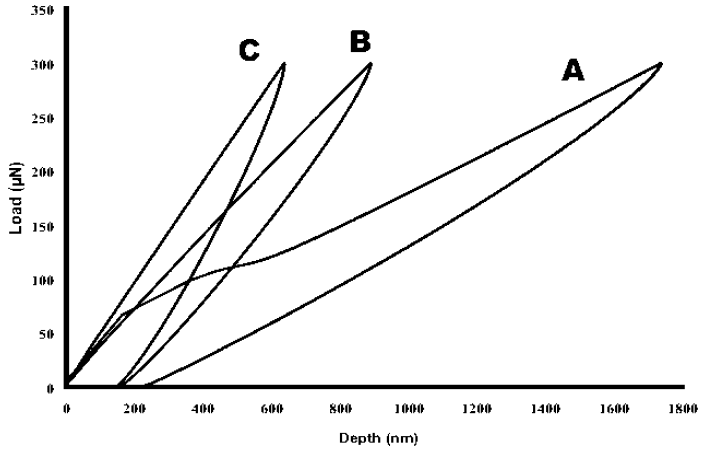

Figure 3.5 Representative P-h curves for a 50BL HA-chitosan PEM: (A) unmodified, (B) cross-linked for 1 min, and (C) cross-linked for 2 min.

Table 3.3 Peak load and Young's modulus values for unmodified and cross-linked HA-chitosan PEMs, n = 9.

	Unmodified PEM	**Cross-linked PEM (1 minute)**	**Cross-linked PEM (2 minutes)**
Peak Load (μN)	300	300	300
Young's Modulus (MPa)	90.9 ± 38.3	309.7 ± 42.6	477.7 ± 33.3

When BALB/c 3T3 fibroblasts were cultured on the detachable PEMs, cell viability remained unaffected. Cells cultured on 1 minute and 2 minute cross-linked PEMs for a period of 24h exhibited greater than 96% viability demonstrating that the free-standing PEMs were biocompatible and could be incorporated into cell culture applications.

Cellular proliferation studies were conducted over a six day period. The cell density on the 1 and 2 minute cross-linked PEMs measured 24h post-seeding, was found to be statistically insignificant ($p > 0.05$). Fibroblasts proliferated on both substrates and their density increased 1.5 -1.7 fold over a three day period (**Figure 3.6**). The differences between the values for cell density measured three days post-seeding and those obtained after 24h were found to be statistically significant. The p-values for day three in comparison to day one in culture were calculated to be 2.3×10^{-6}, and 4.4×10^{-6} for the 1

and 2 minute PEMs respectively. By the fifth day in culture, the cell density increased approximately four-fold. The p-values for cell density on day five in comparison to day one in culture were calculated to be 1.9 $x10^{-35}$, and 1.03 x 10^{-37} for the 1 and 2 minute PEMs respectively. Comparisons on cell density between the 1 and 2 minute PEMs did not reveal significant differences during early time points. The cell density up to the fourth day in culture on the 1 and 2 minute cross-linked PEMs was found to be statistically insignificant ($p > 0.05$). However, on day five, the cell density on the 1 minute cross-linked PEM was found to be statistically higher than the 2 minute cross-linked substrate ($p = 0.004$). By day six in culture, due to extensive cellular proliferation, the entire surface area was covered.

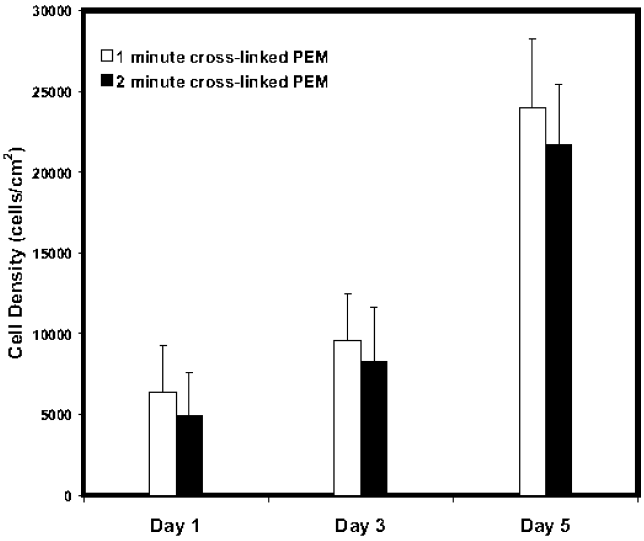

Figure 3.6 Cellular proliferation measured over a five day period for 1 and 2 min cross-linked PEMs; n = 3.

The actin cytoskeletal organization was found to be similar for cells cultured on the PEM substrates (**Figure 3.7**). Fibroblasts adherent on 1 and 2 minute cross-linked PEM, exhibited well-defined actin stress fibers, in the peripheral as well as the interior regions of the cell. These results suggest that the cells are well adhered on the underlying cross-linked PEM.

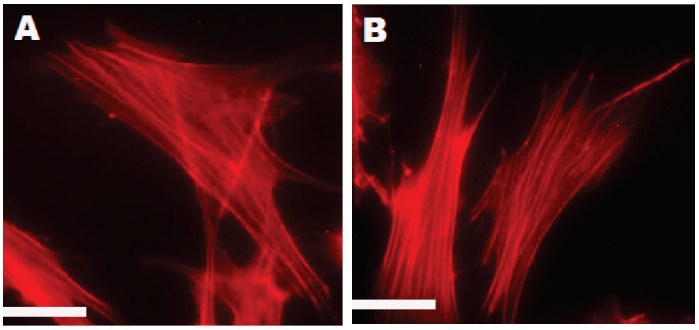

Figure 3.7 Actin cytoskeletal organization imaged 1 day after cell-seeding on (A) 1 min and (B) 2 min cross-linked PEM. Scale bar = 50 µm.

3.4 DISCUSSION

Detachable and free-standing chitosan-HA PEMs were fabricated by depositing the multilayers on an inert hydrophobic poly (propylene) surface. This fabrication methodology is simple, versatile and does not require any post-assembly processing, such as, the dissolution of a sacrificial layer to obtain detachable and free-standing films (95, 116, 133, 195-201). This approach enables the construction of detachable PEMs that can incorporate reaction chemistries incompatible with live cells. In the future, such chemical flexibility will make it possible to build into the films several unique features, such as, the ability to finely tune both the chemical and mechanical properties. An additional advantage of these PEMs is that they can be chemically modified to incorporate cell-specific functional groups, which offer enormous potential in tailoring them for specific cell-types.

Free-standing, cross-linked PEMs comprised of 50 bilayers exhibited virtually no degradation when maintained at 37°C in 1X PBS over a seven day period. These results clearly demonstrate that these PEMs can be used in biological applications that require long-term exposure to aqueous solutions. Furthermore, cross-linking with glutaraldehyde did not result in significant changes in either the bulk or the surface chemistry of the PEMs. A unique feature of the free-standing PEMs is their virtual transparency in the 400 - 900 nm range under hydrated conditions. Since these free-standing PEMs were designed for applications as biomaterials, optical transparency is a highly desirable property. In the future, this unique property will promote the use of hydrated HA-chitosan PEMs as biomaterial scaffolds.

Unmodified and cross-linked PEMs exhibited smooth surfaces, with peak to valley heights less than 10 nm. The values of Young's modulus ranged from 300-400 MPa, rendering these PEMs ideal for culturing different cell types. Furthermore, the mechanical properties can be easily modulated by simply changing the cross-linking conditions or by changing the number of bilayers. For example, if lower values of Young's modulus are desirable, then a reduction in the number of bilayers and cross-linking times can be explored. PEMs cross-linked with glutaraldehyde exhibited

excellent compatibility with BALB/c 3T3 fibroblasts and the surfaces were colonized within six days. These results clearly indicate the tremendous potential that detachable chitosan-HA PEMs exhibit for future applications in tissue engineering and biomaterials. *In vivo*, several tissues and organs exhibit a lattice-like, stratified architecture. However, mimicking such structures *in vitro* is non-trivial. A major focus in the field of tissue engineering is the use of tissue-like, three dimensional cellular structures (57, 163, 181, 219, 220). However, the assembly of such tissue mimics necessitates the design of biomimetic basement membranes to support each cell layer (132, 137). Furthermore, such membranes would have to closely match the physical and chemical environment within a specific tissue. For example, in previous reports, charged PEs such as chitosan, HA, or DNA were deposited above a layer of live hepatocytes (the primary cell-type found in the liver) (70, 72). Once the PEM was deposited above live cells, a second layer of endothelial cells was deposited in an effort to design liver tissue mimics. However, the presence of live cells during the deposition limited the ability to modulate the chemical and mechanical properties of the resulting PEM. In contrast, detachable, free-standing and biocompatible PEMs offer a new route in the design of such tissue-specific membranes for the assembly of layered tissue-like structures. Since all the modifications can be performed prior to cellular exposure, the use of harsh, non-physiological fabrication and reaction conditions as well as toxic solvents is feasible.

In the future, the introduction of porosity into the PEMs would further advance the role of free-standing PEMs in tissue engineering applications (137). Porosity plays a significant role in controlling the diffusion of gases and nutrients to cells. Basal membranes exhibit porosity form the micro- to the nano-scale (132). In a recent report, it was observed that human corneal epithelial cells exhibited an optimal response only when cultured on porous, supported PEMs with pore diameters measuring approximately 100 nm, similar to the porosity found *in vivo* (137). A potential route to introduce and control the size of pores would be to use a spin-coating approach (194, 204). Future investigations will focus upon tuning the chemistry of the PEMs, the introduction of specific cell-adhesive ligands, varying the mechanical properties, and studying the cellular response when the PEMs are incorporated into layered tissue mimics.

3.5 CONCLUSIONS

We have reported the fabrication of detachable, free-standing and biocompatible PEMs comprised of chitosan and hyaluronic acid. In this study, the PEMs were assembled on a flat, inert and hydrophobic substrate. However, PEMs can be assembled on hydrophobic substrates that exhibit a range of geometries and topographies, and this procedure, can be extended to design detachable films with varying shapes and structures. The assembly of detachable, biocompatible PEMs offers unprecedented control over film architecture, chemistry and mechanical properties. A long-term objective of our research is the incorporation of the free standing PEMs into three-dimensional layered, functional tissue mimics (70, 72). In the future, the inherent versatility and simplicity of fabricating free-standing, detachable PEMs with tunable chemical and mechanical properties will be extremely beneficial in the rational design of biomaterials and scaffolds.

3.6 PUBLISHED SUPPORTING INFORMATION

3.6.1 Fourier Transform Infrared Spectroscopy (FTIR)

FTIR spectra were obtained to determine the chemical composition of the unmodified and crosslinked films. Spectra were obtained on a Varian spectrometer (Palo Alto, CA). FT-IR spectra were obtained at wavelengths ranging from 700 cm^{-1} to 4000 cm^{-1}. Spectra were obtained for unmodified and crosslinked PEMs in transmission mode and averaged over a hundred scans. PEMs were mounted in between two clean CaF_2 windows. The CaF_2 windows were cleaned using ethanol, rinsed with HydroPure water and dried under a stream of nitrogen gas. The CaF_2-PEM samples were placed in the IR beam path and the sample chamber was purged using nitrogen gas until the presence of CO_2 was not observed.

FT-IR spectra of unmodified and crosslinked HA-chistoan films were similar in the 700-4000 cm^{-1} range. In addition, several vibration modes that appear in either pure chitosan or HA were observed in the detachable PEMs (221) (**Figure 3.8**). The C-O stretching mode appeared at 1052 cm^{-1}, the band at 1554 cm^{-1} is assigned to the amide II vibrational mode, the CH3 symmetric stretching mode at 2931 cm^{-1}, and the broad band centered at approximately 3200 cm^{-1} is assigned to NH2 vibrations. An imine vibration mode was present in the crosslinked HA-chitsoan film at 1655 cm^{-1} which was not present in the unmodified film (214). These spectra indicate that crosslinking with glutaraldehyde led to the creation of imine bonds in the crosslinked HA-chitosan films. Comparison of unmodified and crosslinked HA-chitosan film spectra indicated only slight changes in bulk chemistry due to glutaraldehyde crosslinking.

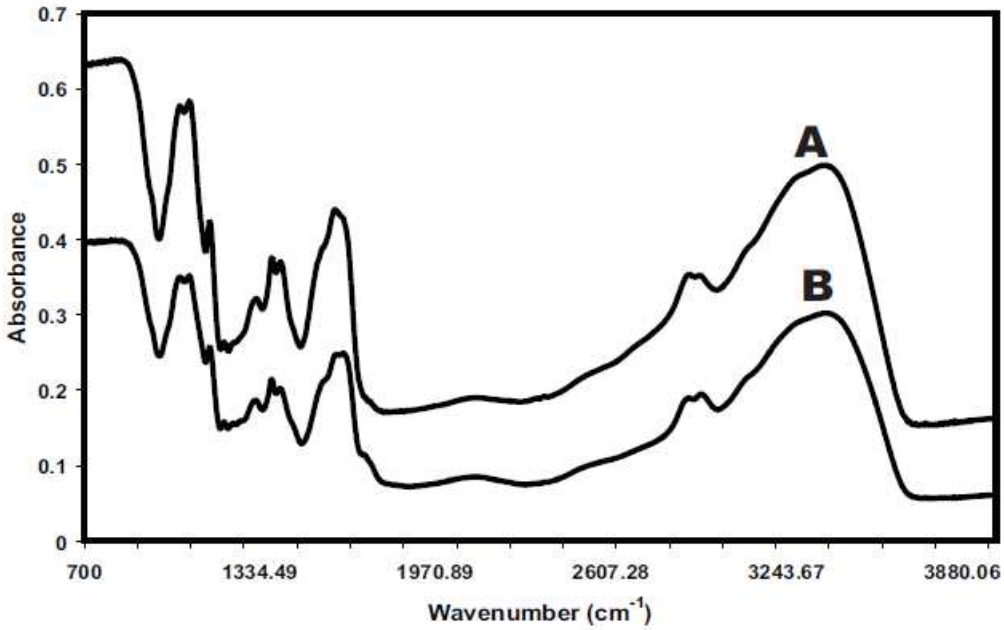

Figure 3.8. FT-IR spectra in the 700-4000 cm^{-1} range for (A) unmodified and (B) Crosslinked HA-chitosan PEM (50 bilayers).

3.6.2 X-ray Photoelectron Spectroscopy (XPS)

XPS studies were performed to determine the surface composition of unmodified and crosslinked detachable PEMs. A Quantera SXM (Physical Electronics, Chanhassen MN) was used with a monochromatic highly focused (<9 μm) Al Kα x-ray beam. Measurements were performed at 45° take-off angle. Survey scans were measured from 0 to 1100 eV followed by high resolution scans in the C_{1s}, N_{1s}, and O_{1s} regions. Residual charging was corrected by referencing the C_{1s} peak to 285.0 eV. Casa XPSTM software with a Voigt approximation was used to analyze the peak positions and areas. The atomic compositions of C_{1s}, N_{1s}, and O_{1s} were calculated using sensitivity factors provided by the manufacturer.

XPS studies were performed to measure elemental composition of the unmodified and crosslinked PEMs at the surface and to determine if crosslinking with glutaraldehyde resulted in a change in surface chemistry. The surface of the PEM adherent on the PP substrate prior to detachment was analyzed. This surface was chosen since cells were cultured on this side of the PEM in subsequent experiments. The C_{1s} peaks were observed at 285 eV (-C-C-, -C-H), and 286 eV (-C-N) (84, 222), the O_{1s} was observed at

532 eV and the N_{1s} peak was observed as a single band at 400 eV (**Figure 3.9**). Elemental compositions were measured at a 45° take-off angle and the depth probed under this condition was approximately 30Å (223). These measurements provided information on carbon/nitrogen (C/N), carbon/oxygen (C/O), and nitrogen/oxygen (N/O) atomic ratios at the surface (**Table 3.4**). The C/N ratio was chosen as a marker to monitor changes in the surface composition since the presence of adventitious oxygen could contribute to the observed changes in the C/O and N/O ratios. The experimental C/O atomic ratios for the unmodified and crosslinked PEMs were found to be 0.8 and 1.2 respectively. The experimental C/N ratios for the unmodified and crosslinked PEMs were 6.99 and 7.3 respectively and the values for N/O were similar as well. Since the difference in the C/N ratio for the unmodified and crosslinked PEMs was less than 5%, these data suggest that the elemental composition at the surface did not change significantly upon crosslinking. The C/N ratio closely matched the theoretical values calculated for chitosan, suggesting that the surface is enriched with this PE. Slight differences in C/N and C/O ratios between unmodified and crosslinked HA-chitosan PEM were observed due to the incorporation of GA. Since GA contains C atoms, covalent crosslinking increased the C/O and C/N ratios. Since HA was the first PE to be deposited on the PP substrate, this indicated that significant mixing of the two PEs occurred during the early stages of deposition, a phenomenon that has been widely observed and reported (64).

Table 3.4. The surface elemental composition of unmodified and crosslinked HA-chitosan PEMs.

	C/N	**C/O**	**N/O**
Chitosan (theoretical values)	6.3	1.98	0.31
HA (theoretical values)	14	1.24	0.09
Unmodified PEM	6.9	0.8	0.11
Crosslinked PEM (1 min)	7.3	1.25	0.17

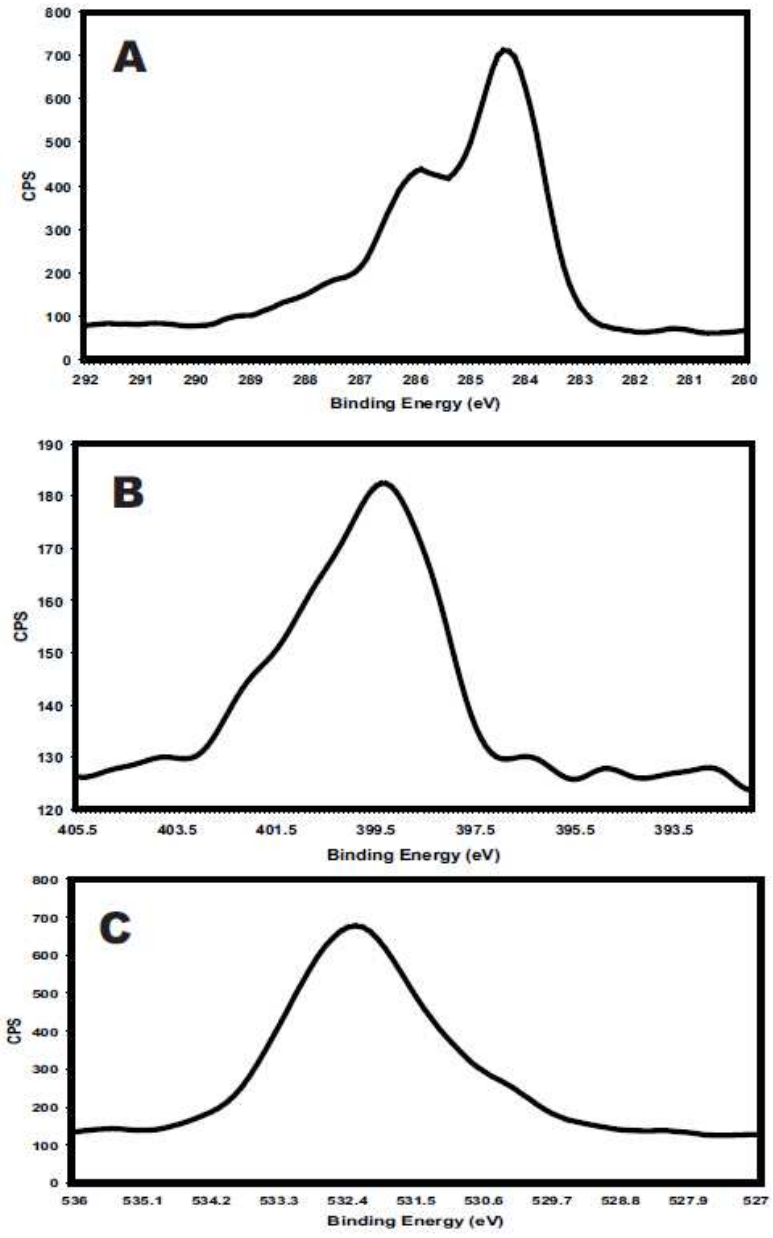

Figure 3.9. Representative high-resolution XPS scans for a crosslinked 50BL HA-chitosan PEM, (A) C_{1s}, (B) N_{1s}, and (C) O_{1s}.

Chapter 4. Mimicking the Multi-cellular Hepatic Microenvironment with Detachable, Nanoscale Self Assembled Multilayers

Larkin AL, Rodrigues R, Murali TM, Rajagopalan P. In preparation.

Chapter 4. Mimicking the Multi-cellular Hepatic Microenvironment with Detachable, Nanoscale Self Assembled Multilayers

4.1 INTRODUCTION

It has been well established over the past several decades that eliciting and maintaining the function and phenotype of hepatic cells in cultures is a very difficult problem (2). Hepatocytes (parenchymal cells) cultured in monolayers (HMs) lose their phenotypic functions and suffer from mRNA degradation within 24hrs of their removal from the liver (16, 17, 151). Monolayers of liver sinusoidal endothelial cells (LSECs) (224) and Kupffer cells (KCs) (41, 42) also rapidly dedifferentiate within a few days *in vitro*. Collagen sandwich (CS) and 2D co-cultures are widely used to maintain the function of hepatocytes. Although hepatocytes cultured in a CS or in 2D co-cultures have been shown to exhibit stable expression of hepatic markers up to six weeks (15-17, 37, 45, 47, 156), these cultures do not emulate hepatic architecture *in vivo*. CS cultures do not incorporate hepatic non-parenchymal cells, which are critical in maintaining liver homeostasis (2), while 2D co-cultures fail to capture the stratified cellular arrangement found in the liver (2).

Hepatocytes, LSECs, and KCs carry out several important and complementary functions in the liver including metabolic and detoxification functions (hepatocytes) (2), clearance of toxins and waste from the blood stream (LSECs) (10, 225, 226), and production of cytokines and phagocytosis (KCs) (2, 34). Together, these three cells constitute approximately 85% of the liver by volume. These facts underscore the need to design new *in vitro* hepatic microenvironments that can simultaneously maintain the phenotype of all hepatic cells.

There is a growing recognition that such hepatic microenvironments should mimic the *in vivo* structure of the liver (28, 71). *In vivo*, hepatic parenchymal cells are separated from non-parenchymal cells by an interfacial region known as the Space of Disse (2, 225). This protein-enriched interface exhibits a thickness in the 0.5–1 μm range and plays a critical role in the transfer of signaling molecules and nutrients between parenchymal and non-parenchymal hepatic cells (2, 225). Efforts to recapitulate this three-dimensional

(3D) structure include the use of reconfigurable cell culture substrates (28), multi-compartmental co-cultures (61), the use of magnetic beads (60), and thermally responsive polymers (57). Through the use of micromechanical substrates, March *et al*. demonstrated that LSEC phenotype was maintained only when the parenchymal and non-parenchymal cells were separated by a distance of 80 μm.

To mimic the *in vivo* spatial structure between hepatic cells, we have demonstrated that polyelectrolyte multilayers (PEMs) can serve as a substitute for the Space of Disse (70-72). PEMs were self-assembled above a confluent layer of primary hepatocytes providing an adhesive substrate for an additional layer of cells. Using this approach, we have assembled layered hepatic cellular structures comprised of primary hepatocytes and LSECS that exhibited significantly enhanced protein secretion, detoxification and bile acid homeostasis (70-72, 227). Although this approach was a significant improvement over 2D cultures, the deposition of a PEM on hepatocytes constrained the ability to tune the properties to the Space of Disse.

We report the design of a novel 3D hepatic microenvironment assembled with three different hepatic cell types (hepatocytes, LSECs and KCs) and a detachable PEM that mimics the Space of Disse. The 400–600 nm detachable and transparent PEMs were obtained by deposition on a hydrophobic substrate. The thickness and mechanical properties were optimized to values reported *in vivo*. This liver model maintained the phenotype of all three cell types over a 12 day period. The unique hepatic microenvironment promoted the proliferation of every cell type in such a manner that they maintained *in vivo* parenchymal to non-parenchymal cell ratios. This significant and novel finding demonstrates the ability of the tri-cellular model to provide a hepatic microenvironment that elicits cell proliferation and maintenance of *in vivo*-like cellular ratios. Furthermore, a hepatic model that exhibits *in vivo* like cellular ratios can be used to systematically study liver functions. Notably, we did not observe these trends in 2D co-cultures of any combination of the three cell types. Analysis of genome-wide gene expression data taken from hepatocytes suggested that multi-cellular 3D models

communicated with each other, resulting in cellular proliferation and phenotypic functions.

4.2 MATERIALS AND METHODS

4.2.1 Materials

Dulbecco's modified Eagle's medium (DMEM) with glucose, phosphate-buffered saline (PBS), Hank's buffered salt solution, Earle's Balanced Salt Solution, penicillin, streptomycin, human plasma fibronectin, and trypsin-ethylenediaminetetraacetic acid were obtained from Invitrogen Life Technologies (Carlsbad, CA). Type IV collagenase, HEPES (4-[2-hydroxyethyl] piperazine-1-ethanesulfonic acid), glucagon, calcium chloride, hydrocortisone, sodium dodecyl sulfate (SDS), hydrogen peroxide, glutaraldehyde, dicumarol, 3-methylcholanthrene, Percoll, calf thymus DNA, chitosan, and hyaluronic acid (HA) were purchased from Sigma-Aldrich (St. Louis, MO). All other chemicals, unless otherwise noted, were used as received from Fisher Scientific (Pittsburgh, PA).

4.2.2 Assembly of Detachable PEMs

Chitosan (cationic PE) and HA (anionic PE) were used to assemble detachable PEMs. Chitosan solution was prepared by dissolving the PE in 1% v/v acetic acid. HA solution was prepared by dissolving the PE in 18 MΩ cm water (Hydro, Raleigh, NC). PE solution concentrations ranged from 1 to 5 mM based on repeat unit molecular weight (340.3 g/mol and 874.7 g/mol for chitosan and HA, respectively). The pH of the PE solutions was maintained at 4.0 and 5.0 for chitosan and HA, respectively. HA and chitosan PEMs were assembled on inert, hydrophobic polytetrafluoroethylene (PTFE, McMaster-Carr, Atlanta, GA) substrates using a robotic deposition system (NanoStrata, Tallahassee, FL). Prior to assembly, PTFE substrates were cleaned by sonication in toluene for 1 h. Water contact angle values (KSV Instruments, Helsinki, Finland) on clean PTFE substrates ranged from 111.9 ± 4.2 (n = 15). The assembly conditions of PEMs such as the number of bilayers (BLs, 7.5 – 20) and the deposition time (20 to 40 minutes) were varied to optimize detachability. Between the deposition of each PE layer, the PEMs were rinsed in 18 MΩ cm water maintained at a pH of 4.5 for 4 minutes. The PEMs were crosslinked with glutaraldehyde (8% w/v), air-dried and subsequently tested for detachability. Prior to cell-culture, the PEMs were sterilized under a germicidal UV

source up to 1h. The stability of PEMs in aqueous solutions was determined by placing PEMs in 1X PBS and monitoring the change in mass over a ten day period.

4.2.3 Profilometry and Optical Properties

A Veeco Dektak 150 (Bruker AXS, Tucson, AZ) profiler was used to determine the dry and hydrated thickness of free-standing PEMs. The scan length was maintained at 1000 μm. Thickness values reported were measured at three different locations per sample over three different samples. The transmission of light in the 400 to 900 nm range was measured using a UV/vis spectrophotometer (Perkin-Elmer Lambda 25, Downers Grove, IL) for dry and hydrated PEMs. Hydrated measurements were performed on PEMs maintained in PBS for 24 h prior to the measurement, excess water wicked away and measurements performed within 5 min to prevent dehydration.

4.2.4 AFM Measurements on Surface Topography and Young's Modulus

The surface topography of detachable HA/chitosan PEMs was measured through atomic force microscopy (AFM; Bruker ACS, Santa Barbara, CA). The measurements were conducted using a conical silicon nitride DNP tip with a spring constant of 0.06 N/m (Veeco, Santa Barbara, CA) in contact mode at a scanning rate of 1 Hz and the surface roughness was analyzed using Nanoscope™ software (Bruker AXS).

The Young's modulus of dried PEMs was obtained in contact mode using a pyramidal-tipped silicon nitride cantilever blunted with a half open angle of 36° with a spring constant of 0.24 N/m (Bruker AXS). Force curves were obtained at a scan rate of 2 Hz. A Hertz cone model was used to calculate the elastic modulus for indentations up to 5% of the overall PEM thickness. The force applied, F, during indentation was calculated using Hooke's Law (eq. 1).

$$F = k(d - d_0) \qquad \text{(eq. 1)}$$

where k is the spring constant of the cantilever, d is the deflection of the cantilever, and d_0 is the deflection point during contact. The force applied can be related to the Young's modulus of the indented material through the Hertz model (eq. 2).

$$F = \frac{2\tan\alpha}{\pi}\left[\frac{E}{1-\nu^2}\right]\delta^2 \quad \text{(eq. 2)}$$

The force was correlated to the Young's modulus using the Hertz model (eq 2), where α is the half open angle of the tip = 36°, E is the Young's modulus of the material, ν is the Poisson's ratio (maintained at 0.35) (210), and δ is the indentation. PEMs were dried up to 48h at 50ºC and rehydrated with PBS to obtain measurements under dry and hydrated conditions respectively.

4.2.5 Isolation and Culture of Heps and LSECs and KCs

Primary hepatocytes were isolated from female Lewis rats (Harlan, Dublin, VA, weighing 175-199g) utilizing a two-step *in situ* collagenase perfusion method (16, 17, 70-72, 147). Animal care and surgical procedures were conducted in accordance with Virginia Tech's Institutional Animal Care and Use Committee. Liver perfusion and surgical excision were conducted as per previously reported methods (70-72, 147). Hepatocytes were separated from other hepatic cell types using a Percoll density centrifugation technique and their viability was determined using trypan blue exclusion (typical viability 90-95%, yield 150-200 x 10^6 cells).

LSECs were separated from other non-parenchymal hepatic cells using differential adhesion and were subsequently cultured on human plasma fibronectin coated flasks (71). Cryopreserved primary rat KCs (Invitrogen Life Technologies) were maintained in DMEM supplemented with 10% (v/v) heat-inactivated fetal bovine serum, 100 U/mL penicillin, 100 μg/mL streptomycin, 10 μg/mL insulin, and 100 μM β-mercaptoethanol.

4.2.6 Assembly of Multi-cellular Hepatic Cultures

Hepatocytes were initially cultured as monolayers up to 72 h (70, 71). For 2D multi-cellular cultures, LSECs, KCs or both were seeded thereafter. For the 3D liver models, UV-sterilized detachable PEMs (12.5 or 15 BL) were placed above the layer of hepatocytes. The PEMs were hydrated in the presence of hepatocyte culture medium for 1h. Thereafter, either 12,500 (denoted as 12.5K) or 25, 000 (denoted as 25K) LSECs were seeded on the PEM. In cultures containing KCs, initially 50,000 cells were seeded on the PEM or to the 2D culture to obtain an initial ratio of 10:1 hepatocytes:KCs to emulate healthy livers (34). All multi-cellular cultures (2D and 3D) were subsequently

maintained in hepatocyte culture medium. Hepatocyte cultures containing more than one cell type are noted as **H/XBL/Y/Z** where **H** denotes hepatocytes, **X** denotes the number of bilayers in the PEM (12.5 or 15 BL), **Y** is the number of LSECs, and **Z** is the number of KCs. For example a 2D co-culture of hepatocytes and LSECs is denoted by **H/0BL/25K/0K**. A 3D culture containing only hepatocytes and LSECs is denoted as **H/12.5BL/25K/0K** and **H/12.5BL/25K/50K** upon the addition of KCs.

4.2.7 Urea Production and Albumin Secretion

Urea concentration was measured by a colorimetric reaction with diacetyl monoxime using a commercially available BUN assay kit (Stanbio Laboratory, Boerne, TX)(70-72). Albumin concentration was measured using an enzyme-linked immunosorbent assay (ELISA), utilizing a polyclonal antibody to rat albumin (Cappel Laboratories, Aurora, OH). The sample absorbance was measured on a SpectraMax M2 plate reader (Molecular Devices, Sunnyvale, CA). The data were normalized to the DNA content of hepatocytes.

4.2.8 Measurement of DNA Content

Hepatocytes were lysed in a 0.1% SDS solution and the lysates were treated with a fluorescent DNA-binding dye (Hoechst 33258, pentahydrate-bis-benzimide, Sigma Aldrich). Fluorescence intensity was measured using a SpectraMax M2 plate reader (excitation and emission wavelengths were set to 355 nm and 460 nm, respectively). Absorbance was converted to DNA concentration by comparison to a standard curve for calf thymus DNA.

4.2.9 CYP1A1 Enzyme Activity

CYP 1A1/2 dependent exthoxyresorufin o-dealkylase (EROD) activity was induced by the addition of 3-methylcholanthrene (3-MC, 2μM) to cultures 48h before taking measurements. Cultures were incubated with a mixture of ethoxyresorufin (5μM) and dicumarol (80μM) diluted in Earle's Balanced Salt Solution (EBSS)(70-72). Aliquots were transferred at 5, 15, 25, and 35 minutes to a 96-well plate and fluorescence intensity was measured using a SpectraMax M2 plate reader (excitation and emission wavelengths

were set to 530 nm and 580 nm, respectively). Fluorescence intensity was converted to resorufin concentration using a standard curve. The rate of resorufin formation in nM/min was calculated from the early linear increase in the fluorescence intensity, normalized to hepatocyte DNA, and taken as the CYP1A1 enzyme activity. The day 12 enzyme activity values were divided by the day 4 activity values to obtain values of fold change.

4.2.10 Imaging LSECs, KCs and Hepatic Stellate Cells

Hepatic cultures containing LSECs and KCs were fixed in glutaraldehyde/PBS (2% (v/v) for 30 min at room temperature, exposed to 0.1% Triton X-100, and placed in a 1% (w/v) BSA/PBS blocking solution overnight at 4°C. First, the cultures were exposed to the mouse anti-rat primary SE-1 antibody (ImmunoBiological Laboratories, Minneapolis, MN) and the incubated with a TRITC-conjugated secondary rabbit anti-mouse IgG antibody (Sigma-Aldrich). Thereafter, the cultures were incubated with a mouse anti-rat ED-2 FITC-conjugated antibody to identify KCs. The presence of hepatic stellate cells was verified by the incorporation of Oil Red O (0.2%, Sigma-Aldrich). Imaging was conducted on a Zeiss LSM confocal microscope.

4.2.11 Separation of Hepatic Cells in 2D and 3D Cultures

Multi-cellular hepatic cultures (2D and 3D) were exposed to SE-1 and ED-2 antibody conjugated Dynabeads® (CELLection™ Pan Mouse IgG Kit; Invitrogen Life Technologies). Briefly, cell suspensions were incubated with SE-1 and/or ED-2 conjugated Dynabeads® for 20 min at 4°C (228). LSECs and KCs were collected using a magnet (DynaMag™; Invitrogen Life Technologies) and the supernatant contained the hepatocyte-enriched fraction.

4.2.12 Western Immunoblotting of T-cadherin (Cdh13)

The hepatocyte fraction from the HM, CS, **H/12.5BL/25K/0K** and **H/12.5BL/25K/50K** cultures were lysed in a buffer solution that contained the following: 0.1% Triton-X 100, 0.01% SDS, 0.02% sodium vanadate (Sigma), and 0.02% sodium azide (Sigma) along with the a protease inhibitor cocktail (Sigma) containing the following: aprotinin (40

nM), bestatin (2 μM), E-64 (0.7 μM), leupeptin (1 μM), pepstatin A (0.75 μM), and 4-(2-aminoethyl) benzenesulfonyl fluoride hydrochloride (52 μM). Total protein in each sample was measured using a BCA protein assay (Thermo Scientific). The volume of each sample was normalized to contain 10 μg of protein total across all samples. Proteins were separated using a 10% Tris-glycine gel (Invitrogen) and then transferred to a polyvinylidene difluoride (PVDF) membrane (Invitrogen) at 100 mA. After transfer, the membranes were blocked in a solution containing 0.05% Triton X-100, 0.02% SDS, and 2% bovine serum albumin (BSA) in Tris-buffered saline (TBS) for 24 h. Cdh13 was detected by exposing the membrane to the primary antibody for Cdh13 (rabbit polyclonal anti-T-cadherin; Santa Cruz Biotechnology, Santa Cruz, CA) and subsequent exposure to a secondary horseradish peroxidase (HRP)-conjugated antibody (anti-rabbit IgG; Bio-Rad, Hercules, CA). The Cdh13 protein was detected by developing the membrane using a chemiluminscent HRP substrate (Immun-Star™ WesternC™, Bio-Rad). The membrane was scanned using the Chemidoc™ XRS+ system (Bio-Rad and analyzed using Image Lab™ software (Bio-Rad).

4.2.13 Statistical Analysis

The urea and albumin assays are non-destructive. Therefore, measurements could be taken from the same sample on day 4 and on day 12, enabling the computation of the fold change for each sample. Since assays were done in triplicate, three fold change values were available for both the urea and albumin assays, allowing the use of the *t*-test to compare any pair of culture conditions. Since the CYP1A1 assay is destructive, measurements were taken from different samples on day 4 and on day 12. For each culture system, the average of the three measurements on day 12 were compared to those obtained on day 4 to compute the fold change, with the *t*-test used to compute the significance of the fold change. Different culture conditions were contrasted by qualitative comparison of the resulting *p*-values. Bonferroni's correction was applied to adjust for multiple hypotheses testing.

4.2.14 Total RNA Extraction

Total RNA was extracted from hepatocytes using an RNeasy mini kit (QIAGEN, Valencia, CA). Samples in triplicate were labeled according to the Affymetrix Standard Target labeling process, hybridized to the GeneChip Rat Genome 230 2.0 (Affymetrix, Santa Clara, CA), and scanned as recommended by the manufacturer. Complementary RNA (cRNA) synthesis, hybridization, and GeneChip scanning were performed at the Virginia Bioinformatics Institute Core Laboratory facility (147).

4.2.15 Gene Expression Analysis

Gene expression data were obtained and analyzed for HM, CS, **H/0BL/25K/0K**, **H/0BL/25K/50K**, **H/12.5BL/25K/0K**, and **H/12.5BL/25K/50K** on day 12. For each sample, three replicates were analyzed. All samples passed the quality controls imposed by the Simpleaffy package (229). The samples were normalized using the GeneChip RMA (GCRMA) method (230).

4.2.16 Computing Enriched Functions

For each of the contrasts functional enrichment was performed on the normalized data using the Gene Set Enrichment Analysis (GSEA) package (231, 232). GSEA computed the differential expression of each gene in each contrast using the signal-to-noise ratio. GSEA uses the gene sets from the Molecular Signature Database (MSigDB) v 3.0. MSigDB gene sets are divided into different categories. To enable the detection of perturbed biological processes and pathways, C2:CP and C5 gene sets were included in the analysis. The C2:CP collection contained pathways taken from databases such as Biocarta, KEGG, and Reactome, publications in PubMed, and knowledge of experts from the domain. C5 gene sets corresponded to annotations to Gene Ontology (GO) terms (233). Gene sets from NetPath (234), a curated resource for signal transduction pathways were also included. For each pathway, NetPath provides three gene sets: (i) the genes in the pathway, (ii) the genes transcriptionally up-regulated by the pathway, and (iii) the gene transcriptionally down-regulated by the pathway. Taken together, 75 gene sets were used. To obtain the null distribution of *p*-values, GSEA permuted gene sets 5000 times. GSEA estimated the false discovery rate (*q*-value) using the method of Benjamin and

Hochberg (235). Gene sets with FDR q-value < 0.05 were considered to be significant. For each enriched gene set, GSEA also listed the leading edge, which was the subset of the genes in that set that contributed to the enrichment of the gene set. The most highly up-regulated or the most highly down-regulated genes in the set comprise the leading edge. Genes participating in leading edges and their relevance to hepatocytes and the liver, as evidenced by the literature, have been discussed in the results.

Some of the enriched gene sets identified by GSEA were themselves very broad, e.g., they contained genes from numerous processes or pathways. The leading edges of such gene sets were further analyzed using FuncAssociate (236), a functional enrichment tool, that given a set of genes, uses the Fisher's Exact Test to identify GO terms that are enriched among these genes. FuncAssociate uses empirical resampling to correct for multiple hypotheses testing.

Since multiple sources of gene sets were included in the analysis and due to the hierarchical structure of GO, some of the gene sets reported by GSEA and FuncAssociate as being enriched were very similar in terms of their gene content. Enriched gene sets were selected for further evaluation and discussion after manual examination.

4.3 RESULTS

4.3.1 Assembly of Detachable, Nanoscale PEMs

PEMs comprised of HA and chitosan were assembled on chemically inert, hydrophobic PTFE substrates. Anionic HA was initially deposited on PTFE followed by chitosan. The successful detachment of the PEM was facilitated by the weak interactions between the initial PE layers and the underlying hydrophobic substrate (83, 202). The detachability and the robustness of the final PEMs were tested as a function of the number of BLs, PE concentration, and adsorption time. The assembly of detachable HA-chitosan PEMs whose thickness ranged between 3.5 to 8 μm has been previously reported(83). However, the use of thick PEMS would prevent emulating *in vivo* hepatic structure. Therefore, in order to obtain PEMs whose thickness would mimic that of the Space of Disse (0.5-1 μm) the number of BLs was decreased while increasing the solution concentration and deposition times (**Table 4.1**). Using this approach, 400-600 nm thick PEMs were obtained. The thinnest robust, free-standing PEMs were obtained at 12.5 and 15 bilayers with 40 min PE deposition times and 5 mM PE concentrations. The corresponding thickness for dry 12.5 and 15 BL PEMs was 400 ± 29.7 nm (n = 6) and 654 ± 17.5 nm (n = 6), respectively (**Table 4.2**). Both 12.5 and 15 BL detachable, free-standing HA/chitosan PEMs were robust, and could be manipulated for further experimentation (**Figure 4.1A**).

Table 4.1. Deposition conditions to assemble detachable HA/chitosan PEMs

Number of BLs	Deposition Time (min)	[PE] (mM)	Detachability
10	20	1	*Not detachable*
10	40	1	*Not detachable*
10	60	1	*Not detachable*
10	80	1	*Not detachable*
10	40	5	Detachable, fragile
12.5	40	5	Detachable,
15	40	1	*Not detachable*
15	40	5	Detachable
20	40	5	Detachable

Table 4.2. Thickness and Young's modulus values measured for dry and hydrated free-standing HA/chitosan PEMs.

	12.5 BL PEM	**15 BL PEM**
Thickness (n = 6)		
Dry	400 ± 30 nm	751 ± 29 nm
Hydrated	654 ± 18 nm	1023 ± 46 nm
Young's Modulus (n = 3)		
Dry - Unmodified	52.16 ± 14.31 MPa	49.01 ± 16.67 MPa
Dry - Crosslinked	98.79 ± 19.35 MPa	93.02 ± 17.65 MPa
Hydrated - Unmodified	-	-
Hydrated - Crosslinked	41.79 ± 3.65 kPa	38.15 ± 2.62 kPa

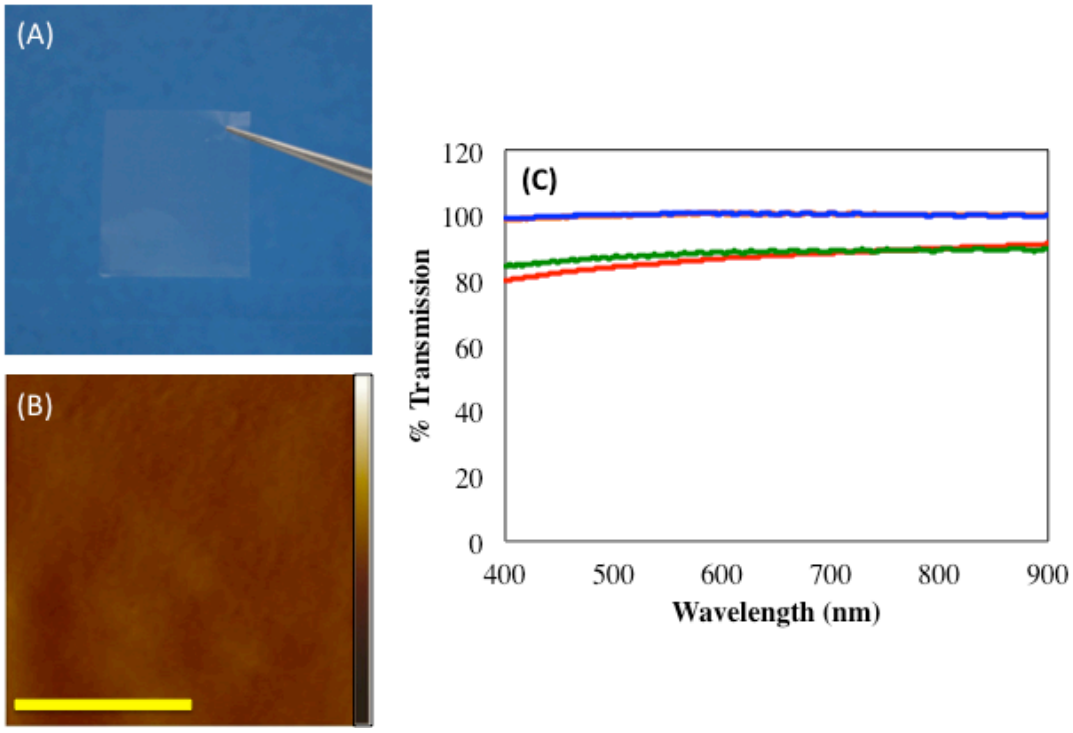

Figure 4.1. (A) Detachable 12.5 BL HA/chitosan PEM, (B) representative AFM micrograph of a crosslinked 12.5 BL HA/chitosan PEM, and (C) transmission of visible light through dry 12.5 (red) and 15 bilayer PEMs (green) and hydrated 12.5 (orange) and 15 bilayer PEMs (blue). Scale bar = 0.5 µm. Z axis scale bar = 30 nm.

Due to the ionic nature of PEMs, they dissolved within 5 min when exposed to aqueous solutions. To increase their stability in aqueous solutions and to make them compatible with cell-culture, the PEMs were briefly cross-linked with 8% w/v GA (124, 208). The PEMs were washed repeatedly and no cytotoxicity (83) nor changes in hepatic function

were observed as a result of this cross-linking chemistry. Upon cross-linking the retention in mass was greater than 85%. In the present study the surface roughness did not vary significantly. The surfaces were found to be essentially smooth for both unmodified and crosslinked 12.5 and 15 BL PEMs. The average surface roughness for unmodified and cross-linked 12.5BL PEMs ranged from 7.9 ± 1.2 nm (n = 3), to 9.2 ± 1.4 nm (n = 3), and 7.2 ± 0.9 and 8.8 ±1.5 nm (n = 3), for 15BL PEMs (**Figure 4.1B**). Under hydrated conditions, cross-linked 12.5 and 15 BL PEMs exhibited thicknesses of 751 ± 29 nm (n = 6) and 1023 ± 46 nm (n= 6), respectively. The thickness of the PEMs increased approximately two-fold under hydration (83) resulting in a polymeric interface whose height was virtually identical to that of the Space of Disse (2, 9, 225).

An important design criterion was to ensure the transparency of the polymeric Space of Disse. This was critical in order to visually inspect and image layers of hepatic cells above and below the PEM. The transmission of visible light was approximately 85% for dried PEMs but under hydrated conditions, the PEMs were virtually transparent with transmission values greater than 99% (**Figure 1C**). Another critical parameter was tuning the mechanical properties of the PEM to match those reported for bulk liver (152, 153). The modulus of bulk liver has been shown to lie in the 40 to 200 kPa range (152, 153). The Young's modulus of dry and hydrated PEMs was measured using an AFM in force-distance mode (**Table 4.2**). For unmodified dry 12.5 and 15 BL PEMs, the Young's modulus ranged between 52.16 ± 14.31 to 49.01 ± 16.67 MPa respectively. Upon crosslinking, the Young's modulus of dry PEMs increased approximately 2-fold to 98.79 ± 19.35 MPa and 93.02 ± 17.65 MPa for 12.5 and 15 bilayer HA/chitosan PEMs, respectively. Upon hydration the modulus decreased to 41.79 ± 3.65 kPa (12.5 BL) and 38.15 ± 2.62 kPa (15 BL), resulting in PEMs whose mechanical properties matched those of liver tissue. The Young's modulus of a hydrated collagen gel was also measured (as a comparison between liver models and CS cultures) and was found to be 94.42 ± 1.54 kPa.

4.3.2 Assembly of 2D and 3D Multicellular Cultures

Urea production and albumin secretion were measured over a 12-day culture period to determine the optimal cell numbers (2D and 3D cultures) as well as the number of BLs

(3D cultures). Initial results indicated that 12.5 BL PEMs performed better than 15 bilayer PEMs with respect to urea production and albumin secretion (**Figure 4.2A and B**). Additionally, **H/12.5BL/25K/0K** performed better than **H/12.5BL/12.5K/0K** and **H/12.5BL/50K/0K** (**Figure 4.2A and B**). Therefore, subsequent investigations were focused upon cultures that contained 500,000 hepatocytes, 25K LSECs, 50K KCs and 12.5 BL HA/chitosan PEMs.

(A)

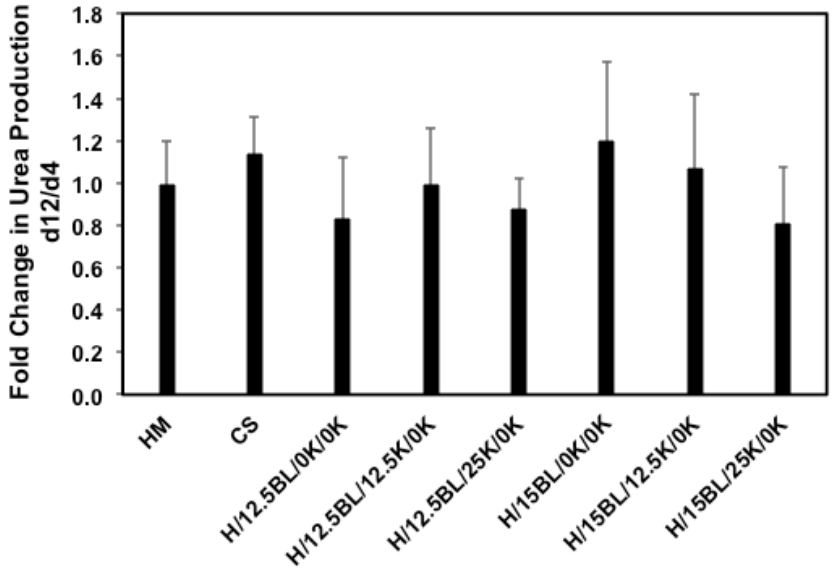

(B)

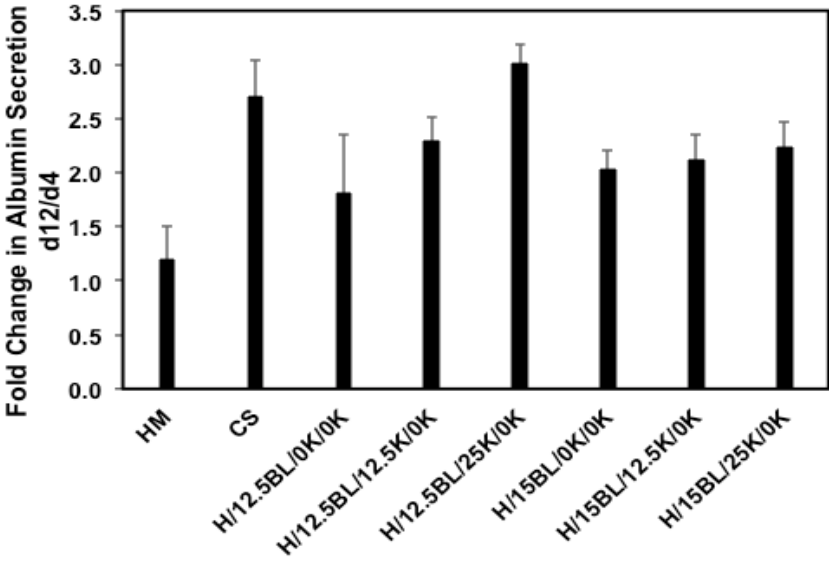

Figure 4.2. Fold change in urea production (A) and albumin secretion (B) between days 4 and 12 for cultures HM, CS, H/12.5BL/0K/0K, H/12.5BL/12.5K/0K, H/12.5BL/25K/0K, H/15BL/0K/0K, H/15BL/12.5K/0K, and H/12.5BL/25K/0K.

4.3.3 Assessing the Phenotype of Hepatic Cells

Immunostaining was used to monitor the maintenance of phenotype for LSECs and KCs on days 4 and 12 in all cultures. The phenotype of LSECs was validated through the

binding of SE-1 antibody to the cell surface marker CD32b (28, 29). For KCs, the ED-2 antibody that binds to the cell surface marker CD163 was used as a marker (237, 238). HM and CS cultures did not exhibit fluorescence indicating the absence of LSECs and KCs on days 4 and 12 (**Figure 4.3**). Monolayers of LSECs exhibited weak fluorescence only on day 4 and none on day 12 (**Figure 4.4A and B**) matching previous reports (71, 174). A similar trend was observed in 2D co-cultures of hepatocytes with LSECs (**H/0BL/25K/0K**) (**Figure 4.4E and F**). In contrast, LSECs in the 3D cultures (**H/12.5BL/25K/0K** and **H/12.5BL/25K/50K**), not only maintained SE-1 expression over the 12 day culture period but also exhibited significant proliferation (**Figure 4.4I and J, Figure 4.4K and L**). KCs exhibited CD163 cell surface markers in 2D (**Figure 4.4G and H**) and 3D (**Figure 4.4K and L**) multi-cellular cultures over the 12 day period, although, their rates of proliferation varied significantly.

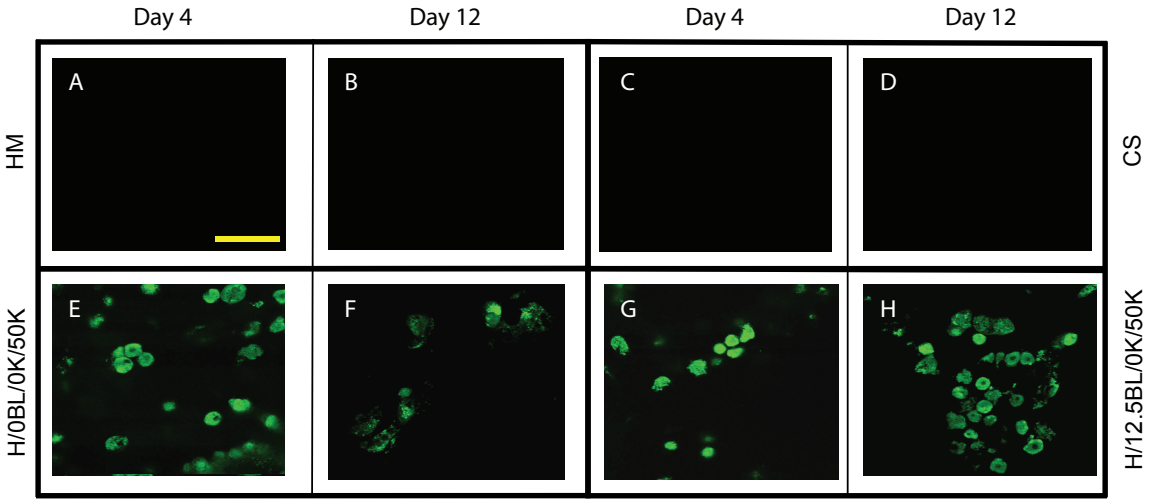

Figure 4.3. Immunofluorescence to assess the phenotype of LSECs (red) and KCs (green). Merged fluorescence images obtained on day 4 in cultures (A) HM, (C) CS, (E) H/0BL/0K/50K, (G) H/12.5BL/0K/50K. Merged fluorescence images obtained on day 12 in cultures (B) HM, (D) CS, (F) H/0BL/0K/50K, (H) and H/12.5BL/0K/50K. Scale bar =50 µm.

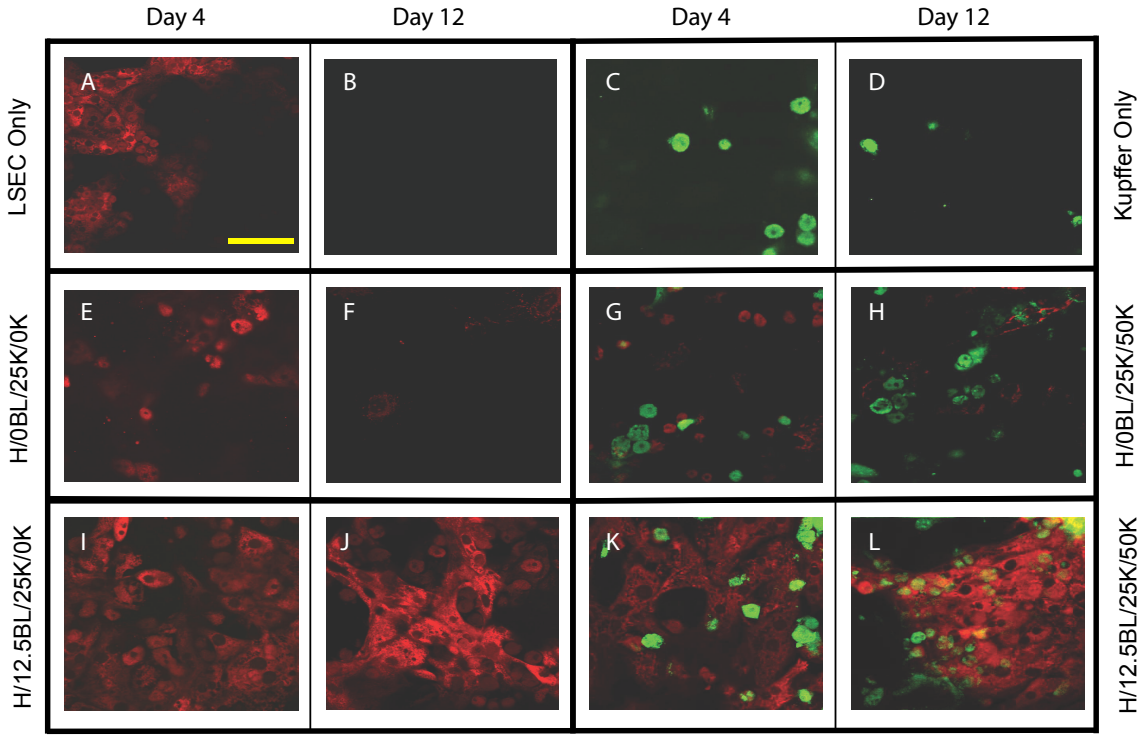

Figure 4.4. Immunofluorescence to assess the phenotype of LSECs (red) and KCs (green). Merged fluorescence images obtained on day 4 in cultures (2A) LSEC monolayer, (2C) KC monolayer, (2E) H/0BL/25K/0K, (2G) H/0BL/25K/50K, (2I) H/12.5BL/25K/0K, (2K) and H/12.5BL/25K/50K. Merged fluorescence images obtained on day 12 in cultures (2B) LSEC monolayer, (2D) KC monolayer, (2F) H/0BL/25K/0K, (2H) H/0BL/25K/50K, (2J) H/12.5BL/25K/0K, (2L) and H/12.5BL/25K/50K. Scale bar = 50 µm.

4.3.4 Investigating the Mode of Inter-cellular Signaling

The potential migration of LSECs and KCs through the PEM into the hepatocyte layer was measured to determine if hepatic cells were communicating via direct contact or through soluble signals. On day 12, the PEM was removed and the number of LSECs and KCs were counted by immunofluorescence imaging of Cd32b (LSECs) and ED-1 (KCs). Fluorescent imaging revealed <1% of LSECs or KCs in the layer of hepatocytes (**Table 4.3**). These data demonstrate that the PEM serves as a barrier and signaling through soluble molecules is dominant in this model. Although hepatic stellate cells were not included in this model, their number in the hepatocyte layer was counted since they could be present in small numbers in the non-parenchymal fraction. Based upon Oil Red

O staining, stellate cells accounted for 0.59 – 0.64% in **H/12.5BL/25K/0K** and **H/12.5BL/25K/50K** cultures.

Table 4.3. Percent of contaminating LSECs, KCs, and HSCs in the hepatocyte layer of the three-dimensional multicellular cultures (n > 14 images per culture).

	LSEC	**KC**	**HSC**
H/12.5BL/25K/0K	0.62%	-	0.59%
H/12.5BL/25K/50K	0.67%	0.56%	0.64%

4.3.5 Measuring Hepatic Functions

Urea production, albumin secretion and CYP1A1 activity were investigated to determine changes in hepatic function between 2D and 3D cultures. Overall, urea production remained stable in all cultures over the culture period (**Figure 4.5 A**). Albumin secretion remained stable in HMs and increased approximately two-fold in CS cultures (**Figure 4.5 B**). All three 3D liver models exhibited higher albumin secretion in comparison to 2D cultures. Albumin secretion increased 3.1 and 3.5-fold in **H/12.BL/25K/0K** and **H/12.5BL/25K/50K**, cultures respectively.

(A)

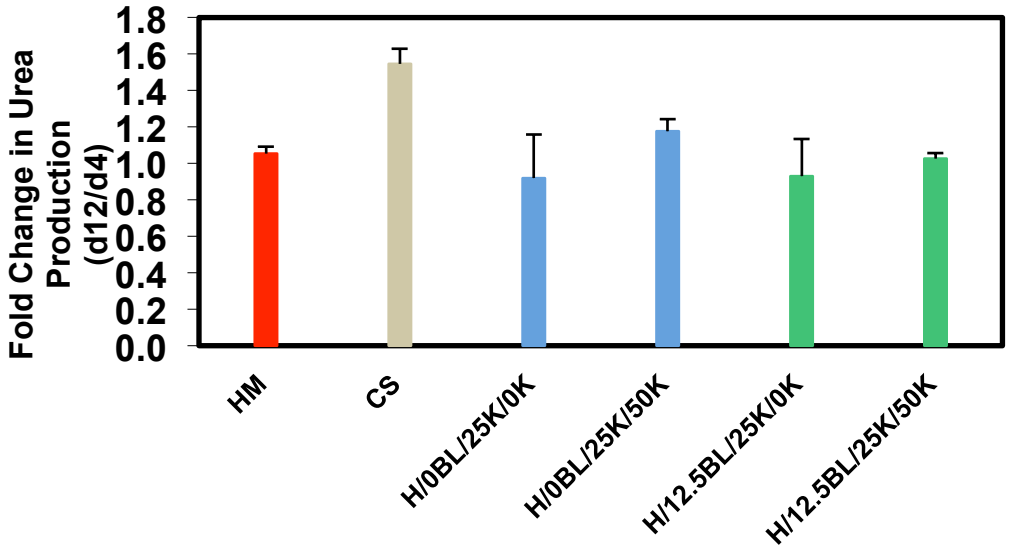

(B)

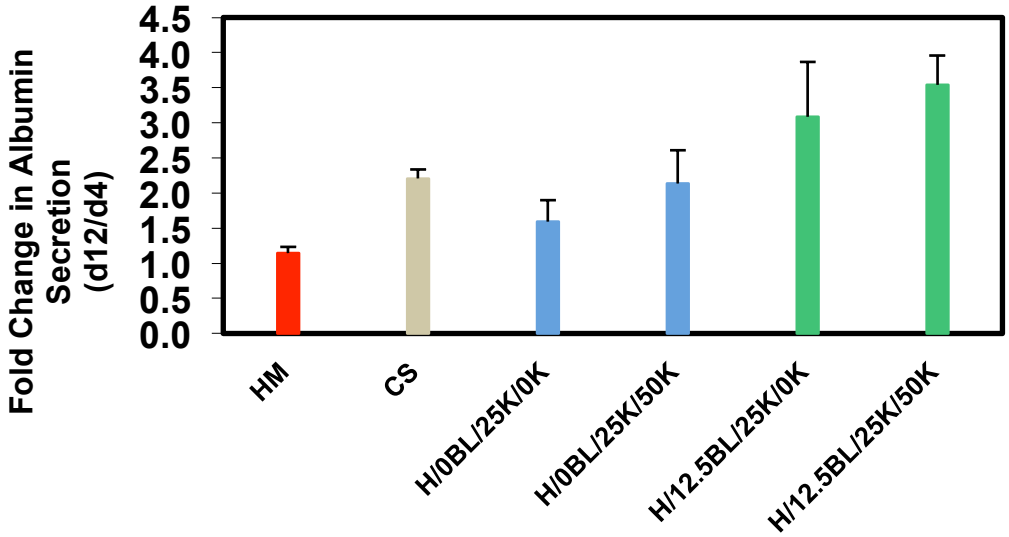

Figure 4.5. Fold change in urea production (A) and albumin secretion (B) between days 4 and 12 of culture for HM, CS, H/0BL/25K/0K, H/0BL/25K/50K, H/12.5BL/25K/0K, and H/12.5BL/25K/50K (n = 3).

The detoxification capability, such as the metabolism of toxins, is an important hepatic function (171, 177, 239). Cytochrome P450 1A1 is a hepatic enzyme responsible for the metabolism of several common toxicants (177). For HM and CS cultures, CYP1A1 isoenzyme activity increased 1.9 and 3.2 fold respectively from day 4 to day 12 (**Figure**

4.6). In the 3D cultures, CYP1A1 isoenzyme activity was similar to trends reported in vivo. For example, when in 3D cultures of hepatocytes and LSECs (**H/12.5BL/25K/0K**) the isoenzyme activity increased approximately 15.4-fold. However, when both LSECs and KCs (**H/12.5BL/25K/50K**) were present, the activity decreased to approximately 6.5-fold. This decrease was attributed to the secretion of the cytokine IL-6 by KCs since this cytokine has been shown to down regulate CYP function (34, 240).

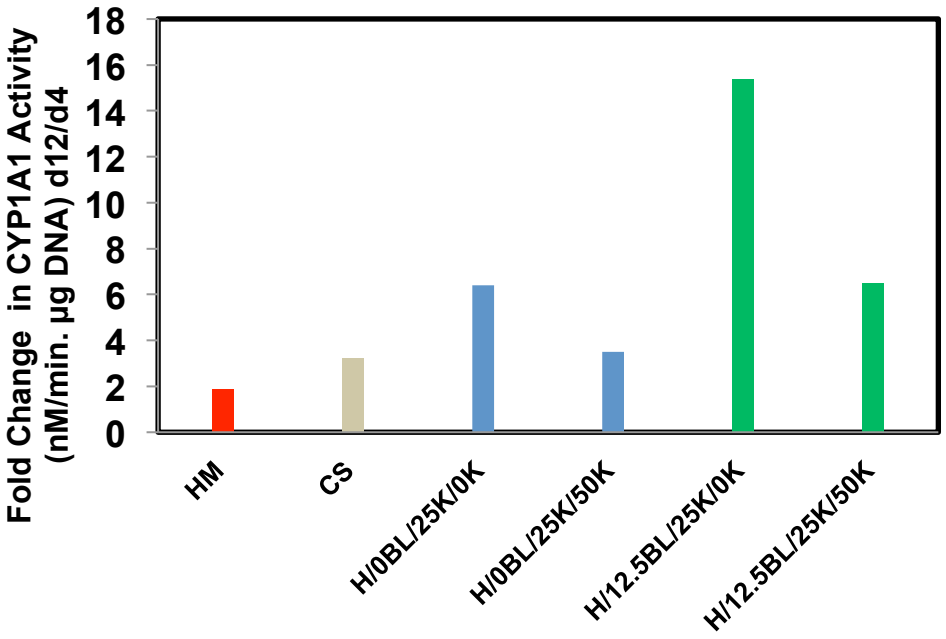

Figure 4.6. Fold change in CYP1A1 isoenzyme activity between days 4 and 12 of culture for HM, CS, H/0BL/25K/0K, H/0BL/25K/50K, H/12.5BL/25K/0K, and H/12.5BL/25K/50K (n = 3).

The increase in CYP1A1 activity from day 4 to 12 was significant in the **H/12.5BL/25K/0K** and **H/12.5BL/25K/50K** cultures with *p*-values of 0.02 and 0.001, respectively.

4.3.6 Proliferation of Hepatic Cells and Maintenance of In Vivo Cellular Ratios

Significant differences were observed between 2D and 3D systems when the numbers of each hepatic cell type were counted over a period of 16 days. 2D co-cultures (**H/0BL/25K/0K and H/0BL/25K/50K**) exhibited hepatocyte death, in contrast, the 3D cultures (**H/12.5BL/25K/0K and H/12.5BL/25K/50K**) exhibited proliferation of

hepatocytes. By day 12 in the 2D co-cultures, the hepatocytes decreased by 14-16% and cells continued to die up to day 16 (**Table 4.4A)**. A decrease in the number of hepatocytes was also observed in HM (~27%) and CS (~5%) cultures. **H/12.5BL/25K/0K and H/12.5BL/25K/50K** cultures exhibited up to a 60% increase by day 16. These trends suggest that intercellular signaling mediated by soluble factors in the 3D models rather than direct cell-cell contact (2D co-cultures) was critical in inducing hepatocyte proliferation. Another interesting trend was that proliferation of all three cell types while maintaining phenotype was only observed in the 3D liver models (**Table 4.4B)**. In **H/12.5BL/25K/0K and H/12.5BL/25K/50K** cultures, the ratio of hepatocytes/LSECs was 6.6 and 6.7 on day 16, the *in vivo* ratio is estimated to be 6:1 (241). In the 2D models, this ratio ranged between 4.3 and 5.1. Although, this indicates that endothelial cells are proliferating in the 2D models, by day 12, these cells no longer exhibited CD32b, suggesting that their phenotype is altered. The *in vivo* ratio of hepatocytes:KCs is estimated to be 11:1 for a healthy liver (241). In **H/0BL/25K/50K and H/12.5BL/25K/50K** cellular models, this ratio was found to be 12.8 and 11.1 respectively. However, by day 16, the number of KCs in the **H/0BL/25K/50K** had increased relative to hepatocytes (7.9:1) suggesting that the culture was progressing towards inflammation. The ratio of hepatocytes:KCs in an inflamed liver is reported to be 4: 1 (34). In contrast, this ratio was 12.4 in **H/12.5BL/25K/50K** cultures indicative of a healthy hepatic cellular composition.

Table 4.4. Percent change in (A) hepatocytes present in the cultures between days 4 and 12 and days 4 and 16. (B) Ratio of hepatocytes to non-parenchymal cells on days 4 and 16.

(A)

Culture	% Change, Day 4 to 12	% Change, Day 4 to 16
HM	-	-29.7
CS	-	-4.6
H/0BL/25K/0K	-9.5	-21.0
H/0BL/0K/50K	-	-20.0
H/0BL/25K/50K	-16.7	-23.6
H/12.5BL/25K/0K	29.7	20.1
H/12.5BL/0K/50K	-	34.8
H/12.5BL/25K/50K	49.4	60.6

(B)

Culture	Hepatocytes:LSECs Day 4	Hepatocytes:LSECs Day 16
H/0BL/25K/0K	33.4	5.1
H/0BL/25K/50K	36.5	4.3
H/12.5BL/25K/0K	28	6.6
H/12.5BL/25K/50K	25	6.7
	Hepatocytes:KCs Day 4	**Hepatocytes:KCs Day 16**
H/0BL/25K/50K	12.8	7.9
H/12.5BL/25K/50K	11.1	12.4

4.3.7 Transcriptional Signatures Corresponding to Hepatocyte Proliferation and Phenotype in H/12.5BL/25K/50K Liver Mimics

Enhanced hepatocyte proliferation in **H/12.BL/25K/0K** and **H/12.5BL/25K/50K** may result from the response of hepatocytes to exocrine signals secreted by the other cell types. To improve our understanding of these phenomena, genome-wide gene expression data were collected in hepatocytes using DNA microarrays on day 12 in each of culture systems. The discussion below focuses on the comparison of **H/12.5BL/25K/50K** to **H/12.5BL/25K/0K** using GSEA (232) to detect biological pathways, physiological processes, and Gene Ontology (GO) terms that were enriched at the 0.05 significance level in the list of genes differentially expressed in this contrast **(Figure 4.7**).

Color Legend for up-regulated gene sets							Color Legend for down-regulated gene sets					
q-value	0.0	0.001	0.01	0.05	0.2	1	1	0.2	0.05	0.01	0.001	0.0
Color												

Rank	H/12.5BL /25K/50K_d12 versus H/12.5BL /25K/0K_d12	Function
1		PEPTIDE_RECEPTOR_ACTIVITY
2		EXTRACELLULAR_MATRIX
3		PROTEINACEOUS_EXTRACELLULAR_MATRIX
4		REACTOME_AMINE_LIGAND_BINDING_RECEPTORS
5		RHODOPSIN_LIKE_RECEPTOR_ACTIVITY
6		AMINE_RECEPTOR_ACTIVITY
7		VOLTAGE_GATED_POTASSIUM_CHANNEL_COMPLEX
8		EXTRACELLULAR_REGION_PART
9		VOLTAGE_GATED_POTASSIUM_CHANNEL_ACTIVITY
10		EXTRACELLULAR_REGION
11		EXTRACELLULAR_SPACE
12		NETPATH_IL4_UP
13		NEUROPEPTIDE_RECEPTOR_ACTIVITY
14		GLUTAMATE_RECEPTOR_ACTIVITY
15		REACTOME_PHASE_1_FUNCTIONALIZATION_OF_COMPOUNDS
16		G_PROTEIN_COUPLED_RECEPTOR_ACTIVITY
17		NEUROPEPTIDE_BINDING
18		CELL_SURFACE
19		EXTRACELLULAR_MATRIX_PART
20		SECOND_MESSENGER_MEDIATED_SIGNALING
21		POTASSIUM_CHANNEL_ACTIVITY
22		CELL_MIGRATION
23		NETPATH_TGF_BETA_RECEPTOR_DOWN
24		NETPATH_LEPTIN_DOWN
25		G_PROTEIN_SIGNALING_COUPLED_TO_IP3_SECOND_MESSENGERPHOSPHOLIPASE_C_ACTIVATING
26		REACTOME_PEPTIDE_LIGAND_BINDING_RECEPTORS
27		REACTOME_NCAM1_INTERACTIONS
28		ACETYLCHOLINE_BINDING
29		KEGG_COMPLEMENT_AND_COAGULATION_CASCADES
30		AMINE_BINDING

Figure 4.7. The top table depicts the color legend for up-regulated and down-regulated gene sets and their respective q-value. The bottom table shows the top 30 significant gene sets in H/12.5BL/25K/0K to H/12.5BL/25K/0K contrast on day 12.

4.3.8 Hepatocytes Express Extracellular Matrix Genes

The gene set "Proteinaceous extracellular matrix" (GO:0005578) was highly up-regulated (*p*-value 0, rank 1). This matrix is a layer composed primarily of proteins such as collagen and proteoglycans that forms a sheet covering cells. The proteins in the matrix are themselves secreted by nearby cells. Hepatocytes are known to synthesize many extracellular matrix (ECM) proteins (242). Leading edge genes annotated to this GO term "proteinaceous extracellular matrix" include over seven types of collagen, nidogen 2

(NID2), laminins, lumican (LUM), transforming growth factor beta 1 (TGF-β1), and members of the fibulin family including Fibulins 2 and 5. Nid2 is a member of the nidogen family of proteins; it binds collagens I and IV and laminin and may be involved in maintaining the structure of the basement membrane.

The Reactome pathway "NCAM1 interactions" (*p*-value 1.7 x 10^{-3}, rank 27) was also up-regulated. The neural cell adhesion molecule, NCAM1 is a surface glycoprotein belonging to the immunoglobulin super family (243). It performs various functions, including mediating cell adhesion and signal transduction (244). CD56, an isoform of NCAM, stains bile ducts in regeneration (245) and in liver development (246, 247). It has been suggested that CD56 might have a function in the normal development of intrahepatic bile ducts, probably by regulating cell–cell and cell–matrix interactions. NCAM1 is itself not highly up-regulated in the comparison between **H/12.5BL/25K/50K** and **H/12.5BL/25K/0K**. However, the leading edge of the "NCAM1 interactions" pathway is made up of several types of collagens, several of which are also members of the leading edge of "Proteinaceous extracellular matrix" gene set.

4.3.9 Hepatocytes Express Genes Involved in Cell Migration

The gene set corresponding to the GO term "Cell migration" (GO:0016477, *p*-value 6.8 x 10^{-4}, rank 22) is highly up-regulated in hepatocytes in **H/12.5BL/25K/50K**. Of particular interest in this leading edge is the gene cadherin 13 (Cdh13, also known as T-cadherin). The cadherin family comprises a large number of cell adhesion molecules. It is known that co-cultivation of primary rat hepatocytes with Chinese hamster ovary cells engineered to express Cdh13 induced hepatocellular function (248). Our results suggest that hepatocytes in **H/12.5BL/25K/50K** themselves express Cdh13, thereby promoting hepatic phenotype in a paracrine manner. However, Cdh13 is not known to be expressed in normal liver simples (249) or in freshly isolated hepatocytes (248), although it is expressed *in vivo* in hepatocellular carcinomas (249) and *in vitro* after stimulation with soluble factors such as FGF-2 (248). It is possible that unknown factors induce the expression of Cdh13 in hepatocytes in **H/12.5BL/25K/50K** over the culture period. In fact, the mechanisms underlying transcriptional control of Cdh13 are poorly understood

(250). Western immunoblotting using Cdh13 antibody verified the presence of the pre-protein with a corresponding molecular weight of 130 kDa in the **H/12.5BL/25K/50K** on day 12 (**Figure 4.8**).

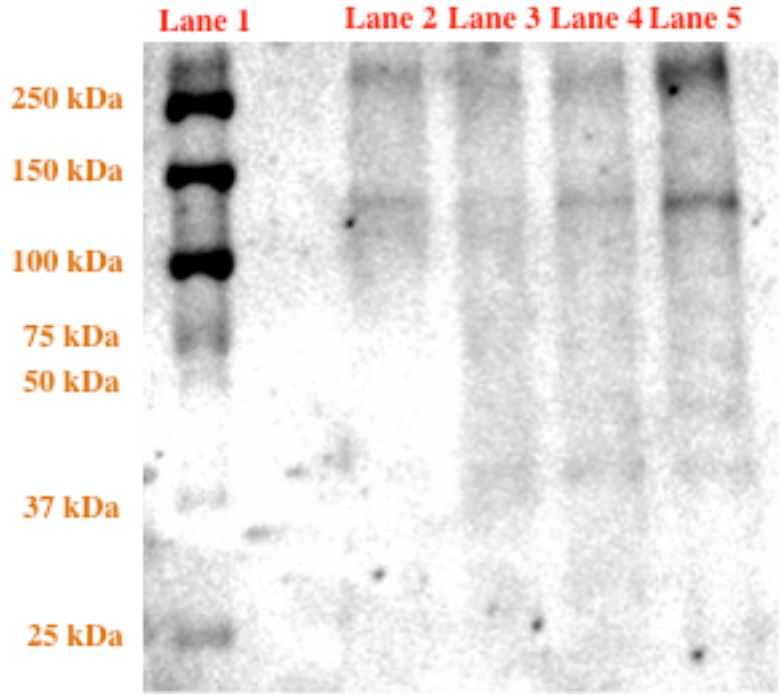

Figure 4.8. Western immunoblot of Cdh13. Lane 1: molecular weight marker with range 250 to 25 kDa, Lane 2: HM, Lane 3: CS, Lane 4: H/12.5BL/25K/0K, and Lane 5: H/12.5BL/25K/50K.

4.3.10 Hepatocytes Express Several Genes in the Cytochrome P450 Family

The Reactome pathway for Phase 1 functionalization of compounds is enriched with *p*-value 2.7 x 10^{-4} and rank 15. Functionalization, the first phase of metabolism, introduces or exposes functional groups on a toxin, which subsequently react with phase 2 species to complete the metabolic process. The leading edge of this gene set contains several members of the cytochrome P450 family including CYP1A2, CYP1B1, CYP2E1, CYP8B1, and CYP26B1. The leading edge also includes the genes flavin containing monooxygenase 2 (FMO2), alcohol dehydrogenase 7 (ADH7), monoamine oxidase A (MAOA), and synthases of prostaglandin-endoperoxide (PTGS1) and I2 (PTGIS).

4.4 DISCUSSION AND CONCLUSIONS

The hepatic microenvironment is a complex structure comprised of multiple cell types and well-defined cellular ratios. Although some liver functions can be elicited by CS and co-cultures, these systems either lack non-parenchymal cells or do not maintain physiological cellular ratios. To the best of our knowledge, we are not aware of any liver model that mimics the Space of Disse, incorporates more than two hepatic cell types, and simultaneously maintains their phenotypes and cellular ratios. In this study, detachable PEMs whose properties were tuned to those of the Space of Disse played an important role in maintaining a physical barrier between hepatic parenchymal and non-parenchymal cells while promoting cellular interactions via soluble molecules. In addition to maintaining cellular function, proliferation of hepatocytes while maintaining cell ratios found *in vivo* was observed only in 3D cultures containing hepatocytes, LSECs and KCs.

The intricate patterns of inter-cellular signaling in the liver arising due to the spatial arrangement of hepatic cells cannot be recapitulated by monolayers or co-cultures. The analysis of DNA microarray data suggested that inter-cellular signaling was responsible for several key observations in the present study. For example, the Netpath gene set was notable: "Netpath IL4 up" (rank 12, *p*-value 2×10^{-4}). The genes in "Netpath IL4 up" are transcriptionally up-regulated when the IL4 pathway is stimulated. The up-regulation of this gene set indirectly suggests that the IL4 pathway is active in hepatocytes in **H/12.5BL/25K/50K** but not in **H/12.5BL/25K/0K** cultures. Note that the "Netpath IL4" gene set itself is not considered to be enriched by GSEA (*p*-value 1), perhaps because proteins in the IL4 pathway may not be differentially expressed when the IL4 pathway is stimulated. Analysis using FuncAssociate revealed that the genes in the leading edge of "Netpath IL4 up" were themselves enriched in the closely related GO terms "positive regulation of endothelial cell proliferation" (BMP2, BMP4, CCL2, F3, WNT5A) and "positive regulation of cell proliferation" (BMP2, BMP4, CCL2, F3, ID3, LIFR, RIPK2, TLR4, WNT5A). Hepatocytes have shown to express wingless-type MMTV integration site family, member 5A (WNT5A) in mice (251), and *Bone morphogenetic proteins 2 and 4 (*BMP2 and BMP4) in human liver and hepatoma-derived Hep3B cells (252).

Although no previous studies implicate these proteins in the proliferation of LSECs, each of these proteins is known to promote the proliferation of other endothelial cell types (253), (254), (255). These data suggest that an intricate signaling pathway involving all three cell types may be activated in **H/12.5BL/25K/50K** cultures. KCs may also initiate this pathway by secreting IL4, causing the activation of the IL4 pathway in hepatocytes, up-regulating the expression of numerous genes, including those whose protein products may cause the proliferation of LSECs. Although LSECs proliferate in all cultures, only the transcriptional data in **H/12.5BL/25K/50K** cultures indicate that other hepatic cell types may play a role. These pathways merit further investigation and will be the focus of future studies.

Chapter 5. CONCLUSIONS AND FUTURE WORK

5.1 CONCLUSIONS

The research presented primarily focused on the following: (1) assembling detachable polyelectrolyte multilayers (PEMs), (2) optimizing assembly conditions to obtain PEMs to mimic the Space of Disse, and (3) incorporating the PEMs into the 3D liver mimic with hepatocytes, liver sinusoidal endothelial cells (LSECs), and Kupffer cells. In addition to the primary research objectives, the properties of PEMs assembled directly on hepatocytes (Chapter 2) were measured using a QCM-D.

In Chapter 2, the design and assembly of 3D liver mimics was discussed. The 3D liver mimics were assembled with hepatocytes, human LSECs, and a nano-scale hyaluronic acid and chitosan PEM. The **specific contribution** to this project was determining the mechanical properties of the 5 and 15 layer PEs using a QCM-D. The height of the PEMs ranged from 30 to 55 nm and exhibited a shear modulus of approximately 100 kPa. Additionally, the shear viscosity of the PEMs was approximately two times that of water, indicating that the PEMs were highly hydrated.

In Chapter 3, the design of detachable chitosan and HA PEMs was discussed. PEMs comprised of 50 bilayers, assembled with 1 mM PE concentrations and 20 min exposure were detachable and robust. The detachable PEMs were essentially transparent under hydrated conditions and had a smooth surface with a peak to valley height of less than 10 nm. The thickness of the 50 bilayer PEM was approximately 3.5 μm under dry conditions and increased 2-fold under hydration. The PEMs were stable in aqueous media for at least 7 days with greater than 95% retention of weight. The mechanical properties were measured using a nanoindenter and found to range from 90 MPa to 480 MPa for unmodified and crosslinked PEMs, respectively. NIH 3T3 BALB/c fibroblasts proliferated 5-fold over a 5-day culture period to confluence and exhibited a well-defined actin cytoskeleton organization. These results demonstrated the ability to assemble detachable PEMs that are biocompatible.

In Chapter 4, the design of 3D liver mimics with detachable PEMs was discussed. Before assembling the 3D liver mimics, the PEM assembly properties were modified to make detachable PEMs at lower bilayer numbers than in Chapter 3. PEMs assembled at 40 min PE deposition and 5 mM PE concentration were robust and detachable at 12.5 bilayers. The thickness of the 12.5 bilayer PEMs was approximately 700 nm under hydrated conditions, well within the range for mimicking the Space of Disse. The PEMs were stable in aqueous medium for up to 10 days (greater than 85% retention of weight) and had a hydrated Young's modulus of approximately 40 kPa (within the range of moduli for the bulk liver, 40 to 200 kPa). PEMs were incorporated into the 3D liver mimic along with primary rat hepatocytes, primary rat LSECs, and primary rat Kupffer cells. The multicellular 3D liver mimics including hepatocytes, LSECs, and Kupffer cells exhibited superior urea production and albumin secretion over a 12 day culture period compared to HM and CS. Both LSECs and Kupffer cells retained phenotype as exhibited by SE-1 and ED-2 expression over 12 days, respectively. Gene expression analysis revealed upregulated gene sets relating to cellular proliferation and extracellular matrix in the hepatocyte fractions of the 3D liver mimics.

5.2 FUTURE WORK

We have designed functional 3D liver mimics using detachable HA and chitosan PEMs, hepatocytes, LSECs, and Kupffer cells. While the detachable PEM mimicked the Space of Disse in several aspects, there are still some features that need to be incorporated. Although, the three most abundant cells of the liver were incorporated, the inclusion of hepatic stellate cells would result in a liver model that completely mimicked the cellular composition *in vivo*. The future areas of this work focus on: 1) More closely mimicking the Space of Disse *in vitro* by modulating the properties of the PEM, 2) introducing more cell types to the 3D liver mimic, and 3) completing gene expression profiling on non-parenchymal cells.

5.2.1 Introducing Porosity into HA and Chitosan PEMs

LSECs lining the hepatic sinusoids have fenestrae that create a porous structure on top of the Space of Disse. The fenestrae act as a molecular sieve that permits diffusion of small molecules and nutrients from the blood to the parenchymal cells. The pore sizes can range from 100 to 200 nm and changes in response to incoming pathogens, making the porosity dynamic. The properties of the PEM mimicking the Space of Disse, specifically the porosity, can be modified to more closely mimic the LSEC fenestrae. Previously, we used acidic solutions to create pores on the PEM surface that resulted in diameters ranging from 200 to 400 nm (**Figure 5.1**). The process resulted in non-uniform pore distribution around the surface and wide range of pore diameters. Future studies will focus on a wide range of strategies to introduce porosity into PEMs.

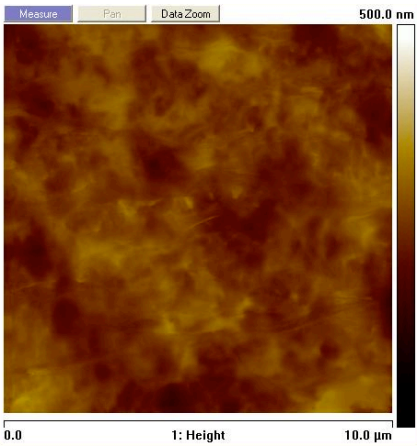

Figure 5.1 AFM micrograph of chitosan/HA PEMs exposed to pH 3.0 acidic solutions.

5.2.2 Introducing Hepatic Stellate Cells into the 3D Liver Mimic

In Chapter 4, Kupffer cells were introduced into the 3D liver mimic in addition to hepatocytes and LSECs. Introduction of Kupffer cells lead to increased hepatic functions such as urea production, albumin secretion, and CYP1A1 enzyme activity. Additionally, gene expression profiling revealed the up-regulation of proliferative proteins in the hepatocytes cultured in a 3D liver mimic with LSECs and Kupffer cells. These results suggest that the addition of other cell types to the mimic resulted in a more robust model for the hepatic microenvironment. However, the model lacks another key cell type found in the liver, hepatic stellate cells (HSCs). HSCs are the fat-storing cells of the liver and are found in either quiescent or activated states as described in Chapter 1. HSCs are the fourth most abundant native liver cell type and are crucial in maintaining liver homeostasis. To more completely mimic the hepatic microenvironment, HSCs will be incorporated into the 3D liver mimic as the fourth cell type. The addition of HSCs will create a more comprehensive model capturing all the possible cell types found in the liver. Hepatocytes, HSCs, LSECs, and Kupffer cells will be incorporated in a layered architecture similar to that found *in vivo*.

5.2.3 Gene Expression Profiling on Non-Parenchymal Cells in the 3D Liver Mimic

In Chapter 4, gene expression profiling was conducted only on hepatocyte fractions isolated from the 3D liver mimics. The gene expression profiles revealed many interesting gene sets that were upregulated in the **H/12.5BL/25K/50K** liver mimics compared to **H/12.5BL/25K/0K**, **HM** and **CS** cultures. These trends clearly suggest that the non-parenchymal cells play a role in mediating heterotypic cell-cell interactions. Gene expression analysis on LSECs and KCs would provide information to till the gaps in our current knowledge. Specifically, such studies can shed light on information on exocrine signals that are received and sent between cells and the subsequent pathways they activate.

REFERENCES

1. Michalopoulos GK, DeFrances MC. Liver regeneration. *Science*. 1997; **276**: 60-6.
2. Arias IM, Boyer JL, Chisari FV, Fausto M, Schachter D, Shafrtx DA. The liver: biology and pathobiology. 4 ed: Lippincott Williams and Wilkins; 2001.
3. LeCluyse EL, Bullock PL, Parkinson A. Strategies for restoration and maintenance of normal hepatic structure and function in long-term cultures of rat hepatocytes. *Adv Drug Delivery Rev*. 1996; **22**: 133-86.
4. Evaluation of Liver Function. Waife SO, Platcow EL, Hammond CE, editors. Indianapolis, Indiana: The Lilly Research Laboratories; 1974.
5. Jungermann K, Kietzmann T. Zonation of parenchymal and nonparenchymal metabolism in liver. *Annu Rev Nutr*. 1996; **16**: 179-203.
6. Jungermann K, Kietzmann T. Oxygen: Modulator of metabolic zonation and disease of the liver. *Hepatology*. 2000; **31**: 255-60.
7. Katz NR. Metabolic Heterogeneity of Hepatocytes across the Liver Acinus. *J Nutr*. 1992; **122**: 843-9.
8. Allen JW, Bhatia SN. Formation of steady-state oxygen gradients in vitro - Application to liver zonation. *Biotechnol Bioeng*. 2003; **82**: 253-62.
9. Wisse E, Braet F, Luo D, De Zanger R, Jans D, Crabbe E, Vermoesen A. Structure and function of sinusoidal lining cells in the liver. *Toxicol Pathol*. 1996; **24**: 100-11.
10. Smedsrod B, De Bleser PJ, Braet F, Lovisetti P, Vanderkerken K, Wisse E, Geerts A. Cell biology of liver endothelial and Kupffer cells. *Gut*. 1994; **35**: 1509-16.
11. Racanelli V, Rehermann B. The liver as an immunological organ. *Hepatology*. 2006; **43**: S54-62.
12. Sato M, Suzuki S, Senoo H. Hepatic stellate cells: unique characteristics in cell biology and phenotype. *Cell Struct Funct*. 2003; **28**: 105-12.
13. Blomhoff R, Wake K. Perisinusoidal stellate cells of the liver: important roles in retinol metabolism and fibrosis. *FASEB J*. 1991; **5**: 271-7.
14. March S, Graupera M, Rosa Sarrias M, Lozano F, Pizcueta P, Bosch J, Engel P. Identification and functional characterization of the hepatic stellate cell CD38 cell surface molecule. *Am J Pathol*. 2007; **170**: 176-87.

15. Moghe PV, Berthiaume F, Ezzell RM, Toner M, Tompkins RG, Yarmush ML. Culture matrix configuration and composition in the maintenance of hepatocyte polarity and function. *Biomaterials*. 1996; **17**: 373-85.

16. Dunn JC, Yarmush ML, Koebe HG, Tompkins RG. Hepatocyte function and extracellular matrix geometry: long-term culture in a sandwich configuration. *FASEB J*. 1989; **3**: 174-7.

17. Dunn JC, Tompkins RG, Yarmush ML. Long-term in vitro function of adult hepatocytes in a collagen sandwich configuration. *Biotechnol Prog*. 1991; **7**: 237-45.

18. Griffith LG, Wu B, Cima MJ, Powers MJ, Chaignaud B, Vacanti JP. In vitro organogenesis of liver tissue. *Ann N Y Acad Sci*. 1997; **831**: 382-97.

19. Smedsrod B. Clearance function of scavenger endothelial cells. *Comp Hepatol*. 2004; **3 Suppl 1**: S22.

20. Elvevold K, Smedsrod B, Martinez I. The liver sinusoidal endothelial cell: a cell type of controversial and confusing identity. *Am J Physiol Gastrointest Liver Physiol*. 2008; **294**: G391-400.

21. Elvevold KH, Nedredal GI, Revhaug A, Smedsrod B. Scavenger properties of cultivated pig liver endothelial cells. *Comp Hepatol*. 2004; **3**: 4.

22. Hellevik T, Bondevik A, Smedsrod B. Intracellular fate of endocytosed collagen in rat liver endothelial cells. *Exp Cell Res*. 1996; **223**: 39-49.

23. McCourt PA, Smedsrod BH, Melkko J, Johansson S. Characterization of a hyaluronan receptor on rat sinusoidal liver endothelial cells and its functional relationship to scavenger receptors. *Hepatology*. 1999; **30**: 1276-86.

24. Nedredal GI, Elvevold KH, Ytrebo LM, Olsen R, Revhaug A, Smedsrod B. Liver sinusoidal endothelial cells represents an important blood clearance system in pigs. *Comp Hepatol*. 2003; **2**: 1.

25. Smedsrod B, Melkko J, Araki N, Sano H, Horiuchi S. Advanced glycation end products are eliminated by scavenger-receptor-mediated endocytosis in hepatic sinusoidal Kupffer and endothelial cells. *Biochem J*. 1997; **322 (Pt 2)**: 567-73.

26. Smedsrod B, Pertoft H, Gustafson S, Laurent TC. Scavenger functions of the liver endothelial cell. *Biochem J*. 1990; **266**: 313-27.

27. Daneker GW, Lund SA, Caughman SW, Swerlick RA, Fischer AH, Staley CA, Ades EW. Culture and characterization of sinusoidal endothelial cells isolated from human liver. *In Vitro Cell Dev Biol Anim*. 1998; **34**: 370-7.

28. March S, Hui EE, Underhill GH, Khetani S, Bhatia SN. Microenvironmental Regulation of the Sinusoidal Endothelial Cell Phenotype In Vitro. *Hepatology*. 2009; **50**: 920-8.

29. Ohmura T, Enomoto K, Satoh H, Sawada N, Mori M. Establishment of a Novel Monoclonal-Antibody, Se-1, Which Specifically Reacts with Rat Hepatic Sinusoidal Endothelial-Cells. *J Histochem Cytochem*. 1993; **41**: 1253-7.

30. Roberts RA, Ganey PE, Ju C, Kamendulis LM, Rusyn I, Klaunig JE. Role of the Kupffer cell in mediating hepatic toxicity and carcinogenesis. *Toxicol Sci*. 2007; **96**: 2-15.

31. Ishibashi H, Nakamura M, Komori A, Migita K, Shimoda S. Liver architecture, cell function, and disease. *Semin Immunopathol*. 2009; **31**: 399-409.

32. Peng Y, Murr MM. Establishment of immortalized rat Kupffer cell lines. *Cytokine*. 2007; **37**: 185-91.

33. Yerkovich ST, Rigby PJ, Fournier PA, Olynyk JK, Yeoh GC. Kupffer cell cytokines interleukin-1beta and interleukin-10 combine to inhibit phosphoenolpyruvate carboxykinase and gluconeogenesis in cultured hepatocytes. *Int J Biochem Cell Biol*. 2004; **36**: 1462-72.

34. Sunman JA, Hawke RL, LeCluyse EL, Kashuba AD. Kupffer cell-mediated IL-2 suppression of CYP3A activity in human hepatocytes. *Drug Metab and Dispos*. 2004; **32**: 359-63.

35. Ding H, Tong J, Wu SC, Yin DK, Yuan XF, Wu JY, Chen J, Shi GG. Modulation of Kupffer cells on hepatic drug metabolism. *W J Gastroenterology : WJG*. 2004; **10**: 1325-8.

36. Blaner WS, O'Byrne SM, Wongsiriroj N, Kluwe J, D'Ambrosio DM, Jiang H, Schwabe RF, Hillman EM, Piantedosi R, Libien J. Hepatic stellate cell lipid droplets: a specialized lipid droplet for retinoid storage. *Biochim Biophys Acta*. 2009; **1791**: 467-73.

37. Bhatia SN, Yarmush ML, Toner M. Controlling cell interactions by micropatterning in co-cultures: hepatocytes and 3T3 fibroblasts. *J Biomed Mater Res*. 1997; **34**: 189-99.

38. Mesnil M, Fraslin JM, Piccoli C, Yamasaki H, Guguen-Guillouzo C. Cell contact but not junctional communication (dye coupling) with biliary epithelial cells is required for hepatocytes to maintain differentiated functions. *Exp Cell Res*. 1987; **173**: 524-33.

39. Morin O, Normand C. Long-term maintenance of hepatocyte functional activity in co-culture: requirements for sinusoidal endothelial cells and dexamethasone. *J Cell Physiol*. 1986; **129**: 103-10.

40. Nahmias Y, Schwartz RE, Hu WS, Verfaillie CM, Odde DJ. Endothelium-mediated hepatocyte recruitment in the establishment of liver-like tissue in vitro. *Tissue Eng*. 2006; **12**: 1627-38.

41. Zinchenko YS, Coger RN. Engineering micropatterned surfaces for the coculture of hepatocytes and Kupffer cells. *J Biomed Mater Res A*. 2005; **75**: 242-8.

42. Zinchenko YS, Schrum LW, Clemens M, Coger RN. Hepatocyte and kupffer cells co-cultured on micropatterned surfaces to optimize hepatocyte function. *Tissue Eng*. 2006; **12**: 751-61.

43. Shimaoka S, Nakamura T, Ichihara A. Stimulation of growth of primary cultured adult rat hepatocytes without growth factors by coculture with nonparenchymal liver cells. *Exp Cell Res*. 1987; **172**: 228-42.

44. Kuri-Harcuch W, Mendoza-Figueroa T. Cultivation of adult rat hepatocytes on 3T3 cells: expression of various liver differentiated functions. *Differentiation*. 1989; **41**: 148-57.

45. Bhatia SN, Balis UJ, Yarmush ML, Toner M. Effect of cell-cell interactions in preservation of cellular phenotype: cocultivation of hepatocytes and nonparenchymal cells. *FASEB J*. 1999; **13**: 1883-900.

46. Lee J, Morgan JR, Tompkins RG, Yarmush ML. Proline-mediated enhancement of hepatocyte function in a collagen gel sandwich culture configuration. *FASEB J*. 1993; **7**: 586-91.

47. Dunn JC, Tompkins RG, Yarmush ML. Hepatocytes in collagen sandwich: evidence for transcriptional and translational regulation. *The Journal of cell biology*. 1992; **116**: 1043-53.

48. Giri S, Acikgoz A, Pathak P, Gutschker S, Kursten A, Nieber K, Bader A. Three dimensional cultures of rat liver cells using a natural self-assembling nanoscaffold in a clinically relevant bioreactor for bioartificial liver construction. *J Cell Physiol*. 2012; **227**: 313-27.

49. Kasuya J, Sudo R, Tamogami R, Masuda G, Mitaka T, Ikeda M, Tanishita K. Reconstruction of 3D stacked hepatocyte tissues using degradable, microporous poly(d,l-lactide-co-glycolide) membranes. *Biomaterials*. 2012; **33**: 2693-700.

50. Lang R, Stern MM, Smith L, Liu Y, Bharadwaj S, Liu G, Baptista PM, Bergman CR, Soker S, Yoo JJ, Atala A, Zhang Y. Three-dimensional culture of hepatocytes on porcine liver tissue-derived extracellular matrix. *Biomaterials*. 2011; **32**: 7042-52.

51. Bierwolf J, Lutgehetmann M, Feng K, Erbes J, Deichmann S, Toronyi E, Stieglitz C, Nashan B, Ma PX, Pollok JM. Primary rat hepatocyte culture on 3D nanofibrous polymer scaffolds for toxicology and pharmaceutical research. *Biotechnol Bioeng*. 2011; **108**: 141-50.

52. Goulet F, Normand C, Morin O. Cellular interactions promote tissue-specific function, biomatrix deposition and junctional communication of primary cultured hepatocytes. *Hepatology*. 1988; **8**: 1010-8.

53. Guguen-Guillouzo C, Clement B, Lescoat G, Glaise D, Guillouzo A. Modulation of human fetal hepatocyte survival and differentiation by interactions with a rat liver epithelial cell line. *Dev Biol*. 1984; **105**: 211-20.

54. Lerche C, Fautrel A, Shaw PM, Glaise D, Ballet F, Guillouzo A, Corcos L. Regulation of the major detoxication functions by phenobarbital and 3-methylcholanthrene in co-cultures of rat hepatocytes and liver epithelial cells. *Eur J Biochem*. 1997; **244**: 98-106.

55. Rojkind M, Novikoff PM, Greenwel P, Rubin J, Rojas-Valencia L, de Carvalho AC, Stockert R, Spray D, Hertzberg EL, Wolkoff AW. Characterization and functional studies on rat liver fat-storing cell line and freshly isolated hepatocyte coculture system. *Am J Pathol*. 1995; **146**: 1508-20.

56. Hirose M, Yamato M, Kwon OH, Harimoto M, Kushida A, Shimizu T, Kikuchi A, Okano T. Temperature-Responsive surface for novel co-culture systems of hepatocytes with endothelial cells: 2-D patterned and double layered co-cultures. *Yonsei Med J*. 2000; **41**: 803-13.

57. Harimoto M, Yamato M, Hirose M, Takahashi C, Isoi Y, Kikuchi A, Okano T. Novel approach for achieving double-layered cell sheets co-culture: overlaying endothelial cell sheets onto monolayer hepatocytes utilizing temperature-responsive culture dishes. *J Biomed Mater Res*. 2002; **62**: 464-70.

58. Ohashi K, Yokoyama T, Yamato M, Kuge H, Kanehiro H, Tsutsumi M, Amanuma T, Iwata H, Yang J, Okano T, Nakajima Y. Engineering functional two- and three-dimensional liver systems in vivo using hepatic tissue sheets. *Nat Med*. 2007; **13**: 880-5.

59. Ito A, Ino K, Hayashida M, Kobayashi T, Matsunuma H, Kagami H, Ueda M, Honda H. Novel methodology for fabrication of tissue-engineered tubular constructs using magnetite nanoparticles and magnetic force. *Tissue Eng*. 2005; **11**: 1553-61.

60. Ito A, Takizawa Y, Honda H, Hata K, Kagami H, Ueda M, Kobayashi T. Tissue engineering using magnetite nanoparticles and magnetic force: heterotypic layers of cocultured hepatocytes and endothelial cells. *Tissue Eng*. 2004; **10**: 833-40.

61. Guzzardi MA, Domenici C, Ahluwalia A. Metabolic Control Through Hepatocyte and Adipose Tissue Cross-Talk in a Multicompartmental Modular Bioreactor. *Tissue Engineering Part A*. 2011; **17**: 1635-42.

62. Decher G, Hong JD, Schmitt J. Buildup of Ultrathin Multilayer Films by a Self-Assembly Process .3. Consecutively Alternating Adsorption of Anionic and Cationic Polyelectrolytes on Charged Surfaces. *Thin Solid Films*. 1992; **210**: 831-5.

63. Decher G, Lvov Y, Schmitt J. Proof of Multilayer Structural Organization in Self-Assembled Polycation Polyanion Molecular Films. *Thin Solid Films*. 1994; **244**: 772-7.

64. Decher G. Fuzzy nanoassemblies: Toward layered polymeric multicomposites. *Science*. 1997; **277**: 1232-7.

65. Kim BS, Park SW, Hammond PT. Hydrogen-bonding layer-by-layer assembled biodegradable polymeric micelles as drug delivery vehicles from surfaces. *ACS Nano*. 2008; **2**: 386-92.

66. Rydzek G, Thomann JS, Ben Ameur N, Jierry L, Mesini P, Ponche A, Contal C, El Haitami AE, Voegel JC, Senger B, Schaaf P, Frisch B, Boulmedais F. Polymer Multilayer Films Obtained by Electrochemically Catalyzed Click Chemistry. *Langmuir*. 2010; **26**: 2816-24.

67. Such GK, Quinn JF, Quinn A, Tjipto E, Caruso F. Assembly of ultrathin polymer multilayer films by click chemistry. *J Am Chem Soc*. 2006; **128**: 9318-9.

68. Kim BS, Smith RC, Poon Z, Hammond PT. MAD (Multiagent Delivery) Nanolayer: Delivering Multiple Therapeutics from Hierarchically Assembled Surface Coatings. *Langmuir*. 2009; **25**: 14086-92.

69. Wong SY, Li Q, Veselinovic J, Kim BS, Klibanov AM, Hammond PT. Bactericidal and virucidal ultrathin films assembled layer by layer from polycationic N-alkylated polyethylenimines and polyanions. *Biomaterials*. 2010; **31**: 4079-87.

70. Kim Y, Larkin AL, Davis RM, Rajagopalan P. The Design of In Vitro Liver Sinusoid Mimics Using Chitosan-Hyaluronic Acid Polyelectrolyte Multilayers. *Tissue Eng Part A*. 2010; **16**: 2731-41.

71. Kim Y, Rajagopalan P. 3D hepatic cultures simultaneously maintain primary hepatocyte and liver sinusoidal endothelial cell phenotypes. *PLoS ONE*. 2010; **5**: e15456.

72. Rajagopalan P, Shen CJ, Berthiaume F, Tilles AW, Toner M, Yarmush ML. Polyelectrolyte nano-scaffolds for the design of layered cellular Architectures. *Tissue Eng*. 2006; **12**: 1553-63.

73. Detzel CJ, Larkin AL, Rajagopalan P. Polyelectrolyte Multilayers in Tissue Engineering. *Tissue Eng Part B, Reviews*. 2011.

74. Mendelsohn JD, Yang SY, Hiller J, Hochbaum AI, Rubner MF. Rational design of cytophilic and cytophobic polyelectrolyte multilayer thin films. *Biomacromolecules*. 2003; **4**: 96-106.

75. Dubas ST, Schlenoff JB. Polyelectrolyte multilayers containing a weak polyacid: Construction and deconstruction. *Macromolecules*. 2001; **34**: 3736-40.

76. Dubas ST, Schlenoff JB. Factors controlling the growth of polyelectrolyte multilayers. *Macromolecules*. 1999; **32**: 8153-60.

77. Schlenoff JB, Dubas ST. Mechanism of polyelectrolyte multilayer growth: Charge overcompensation and distribution. *Macromolecules*. 2001; **34**: 592-8.

78. Richert L, Boulmedais F, Lavalle P, Mutterer J, Ferreux E, Decher G, Schaaf P, Voegel JC, Picart C. Improvement of stability and cell adhesion properties of polyelectrolyte multilayer films by chemical cross-linking. *Biomacromolecules*. 2004; **5**: 284-94.

79. Richert L, Engler AJ, Discher DE, Picart C. Elasticity of native and cross-linked polyelectrolyte multilayer films. *Biomacromolecules*. 2004; **5**: 1908-16.

80. Richert L, Lavalle P, Vautier D, Senger B, Stoltz JF, Schaaf P, Voegel JC, Picart C. Cell interactions with polyelectrolyte multilayer films. *Biomacromolecules*. 2002; **3**: 1170-8.

81. Richert L, Schneider A, Vautier D, Vodouhe C, Jessel N, Payan E, Schaaf P, Voegel JC, Picart C. Imaging cell interactions with native and crosslinked polyelectrolyte multilayers. *Cell Biochem Biophys*. 2006; **44**: 273-85.

82. Schneider A, Richert L, Francius G, Voegel JC, Picart C. Elasticity, biodegradability and cell adhesive properties of chitosan/hyaluronan multilayer films. *Biomed Mat*. 2007; **2**: S45-S51.

83. Larkin AL, Davis RM, Rajagopalan P. Biocompatible, Detachable, and Free-Standing Polyelectrolyte Multilayer Films. *Biomacromolecules*. 2010; **11**: 2788-96.

84. Amaral IF, Granja PL, Barbosa MA. Chemical modification of chitosan by phosphorylation: an XPS, FT-IR and SEM study. *J Biomat Sci-Poly Ed*. 2005; **16**: 1575-93.

85. Chung TW, Yang J, Akaike T, Cho KY, Nah JW, Kim SI, Cho CS. Preparation of alginate/galactosylated chitosan scaffold for hepatocyte attachment. *Biomaterials*. 2002; **23**: 2827-34.

86. Kujawa P, Schmauch G, Viitala T, Badia A, Winnik FM. Construction of viscoelastic biocompatible films via the layer-by-layer assembly of hyaluronan and phosphorylcholine-modified chitosan. *Biomacromolecules*. 2007; **8**: 3169-76.

87. Lin QK, Ren KF, Ji J. Hyaluronic acid and chitosan-DNA complex multilayered thin film as surface-mediated nonviral gene delivery system. *Colloids Surf B Biointerfaces*. 2009; **74**: 298-303.

88. Schlenoff JB, Ly H, Li M. Charge and mass balance in polyelectrolyte multilayers. *J Am Chem Soc*. 1998; **120**: 7626-34.

89. Wistrand I, Lingstrom R, Wagberg L. Preparation of electrically conducting cellulose fibres utilizing polyelectrolyte multilayers of poly(3,4-ethylenedioxythiophene): poly(styrene sulphonate) and poly(allyl amine). *Eur Polym J*. 2007; **43**: 4075-91.

90. Caruso F, Lichtenfeld H, Giersig M, Mohwald H. Electrostatic self-assembly of silica nanoparticle - Polyelectrolyte multilayers on polystyrene latex particles. *J Am Chem Soc*. 1998; **120**: 8523-4.

91. Izquierdo A, Ono SS, Voegel JC, Schaaf P, Decher G. Dipping versus spraying: Exploring the deposition conditions for speeding up layer-by-layer assembly. *Langmuir*. 2005; **21**: 7558-67.

92. Shim BS, Podsiadlo P, Lilly DG, Agarwal A, Leet J, Tang Z, Ho S, Ingle P, Paterson D, Lu W, Kotov NA. Nanostructured thin films made by diewetting method of layer-by-layer assembly. *Nano Lett*. 2007; **7**: 3266-73.

93. Thierry B, Winnik FM, Merhi Y, Silver J, Tabrizian M. Bioactive coatings of endovascular stents based on polyelectrolyte multilayers. *Biomacromolecules*. 2003; **4**: 1564-71.

94. Zhang J, Senger B, Vautier D, Picart C, Schaaf P, Voegel JC, Lavalle P. Natural polyelectrolyte films based on layer-by layer deposition of collagen and hyaluronic acid. *Biomaterials*. 2005; **26**: 3353-61.

95. Shiratori SS, Rubner MF. pH-dependent thickness behavior of sequentially adsorbed layers of weak polyelectrolytes. *Macromolecules*. 2000; **33**: 4213-9.

96. Garg A, Heflin JR, Gibson HW, Davis RM. Study of film structure and adsorption kinetics of polyelectrolyte multilayer films: Effect of pH and polymer concentration. *Langmuir*. 2008; **24**: 10887-94.

97. Hoshi T, Saiki H, Kuwazawa S, Tsuchiya C, Chen Q, Anzai J. Selective permeation of hydrogen peroxide through polyelectrolyte multilayer films and its use for amperometric biosensors. *Anal Chem*. 2001; **73**: 5310-5.

98. Elbert DL, Herbert CB, Hubbell JA. Thin polymer layers formed by polyelectrolyte multilayer techniques on biological surfaces. *Langmuir*. 1999; **15**: 5355-62.

99. Richert L, Lavalle P, Payan E, Shu XZ, Prestwich GD, Stoltz JF, Schaaf P, Voegel JC, Picart C. Layer by layer buildup of polysaccharide films: Physical chemistry and cellular adhesion aspects. *Langmuir*. 2004; **20**: 448-58.

100. Antipov AA, Sukhorukov GB, Donath E, Mohwald H. Sustained release properties of polyelectrolyte multilayer capsules. *J Phys Chem B*. 2001; **105**: 2281-4.

101. Caruso F, Mohwald H. Protein multilayer formation on colloids through a stepwise self-assembly technique. *J Am Chem Soc*. 1999; **121**: 6039-46.

102. Lvov YM, Lu ZQ, Schenkman JB, Zu XL, Rusling JF. Direct electrochemistry of myoglobin and cytochrome p450(cam) in alternate layer-by-layer films with DNA and other polyions. *J Am Chem Soc*. 1998; **120**: 4073-80.

103. Picart C, Mutterer J, Richert L, Luo Y, Prestwich GD, Schaaf P, Voegel JC, Lavalle P. Molecular basis for the explanation of the exponential growth of polyelectrolyte multilayers. *Proc Natl Acad Sci U S A*. 2002; **99**: 12531-5.

104. Richert L, Arntz Y, Schaaf P, Voegel JC, Picart C. pH dependent growth of poly(L-lysine)/poly(L-glutamic) acid multilayer films and their cell adhesion properties. *Surf Sci*. 2004; **570**: 13-29.

105. Schultz P, Vautier D, Richert L, Jessel N, Haikel Y, Schaaf P, Voegel JC, Ogier J, Debry C. Polyelectrolyte multilayers functionalized by a synthetic analogue of an anti-inflammatory peptide, alpha-MSH, for coating a tracheal prosthesis. *Biomaterials*. 2005; **26**: 2621-30.

106. Hammond PT. Form and function in multilayer assembly: New applications at the nanoscale. *Adv Mater*. 2004; **16**: 1271-93.

107. Boudou T, Crouzier T, Ren KF, Blin G, Picart C. Multiple Functionalities of Polyelectrolyte Multilayer Films: New Biomedical Applications. *Adv Mater*. 2010; **22**: 441-67.

108. Riegler H, Essler F. Polyelectrolytes. 2. Intrinsic or extrinsic charge compensation? Quantitative charge analysis of PAH/PSS multilayers. *Langmuir*. 2002; **18**: 6694-8.

109. Nolte AJ, Takane N, Hindman E, Gaynor W, Rubner MF, Cohen RE. Thin film thickness gradients and spatial patterning via salt etching of polyelectrolyte multilayers. *Macromolecules*. 2007; **40**: 5479-86.

110. Lavalle P, Gergely C, Cuisinier FJG, Decher G, Schaaf P, Voegel JC, Picart C. Comparison of the structure of polyelectrolyte multilayer films exhibiting a linear and an exponential growth regime: An in situ atomic force microscopy study. *Macromolecules*. 2002; **35**: 4458-65.

111. Porcel C, Lavalle P, Decher G, Senger B, Voegel JC, Schaaf P. Influence of the polyelectrolyte molecular weight on exponentially growing multilayer films in the linear regime. *Langmuir*. 2007; **23**: 1898-904.

112. Haynie DT, Zhang L, Rudra JS, Zhao WH, Zhong Y, Palath N. Polypeptide multilayer films. *Biomacromolecules*. 2005; **6**: 2895-913.

113. Picart C, Lavalle P, Hubert P, Cuisinier FJG, Decher G, Schaaf P, Voegel JC. Buildup mechanism for poly(L-lysine)/hyaluronic acid films onto a solid surface. *Langmuir*. 2001; **17**: 7414-24.

114. Garza JM, Jessel N, Ladam G, Dupray V, Muller S, Stoltz JF, Schaaf P, Voegel JC, Lavalle P. Polyelectrolyte multilayers and degradable polymer layers as multicompartment films. *Langmuir*. 2005; **21**: 12372-7.

115. Schoeler B, Delorme N, Doench I, Sukhorukov GB, Fery A, Glinel K. Polyelectrolyte films based on polysaccharides of different conformations: Effects on multilayer structure and mechanical properties. *Biomacromolecules*. 2006; **7**: 2065-71.

116. Tang ZY, Kotov NA, Magonov S, Ozturk B. Nanostructured artificial nacre. *Nat Mater*. 2003; **2**: 413-U8.

117. Gheith MK, Sinani VA, Wicksted JP, Matts RL, Kotov NA. Single-walled carbon nanotube polyelectrolyte multilayers and freestanding films as a biocompatible platformfor neuroprosthetic implants. *Adv Mater*. 2005; **17**: 2663-70.

118. Tang Z, Wang Y, Podsiadlo P, Kotov N. Biomedical Applications of Layer-by-Layer Assembly: From Biomimetics to Tissue Engineering. *Adv Mater*. 2006; **18**: 3203-24.

119. Mermut O, Lefebvre J, Gray DG, Barrett CJ. Structural and mechanical properties of polyelectrolyte multilayer films studied by AFM. *Macromolecules*. 2003; **36**: 8819-24.

120. Thompson MT, Berg MC, Tobias IS, Rubner MF, Van Vliet KJ. Tuning compliance of nanoscale polyelectrolyte multilayers to modulate cell adhesion. *Biomaterials*. 2005; **26**: 6836-45.

121. Berg MC, Yang SY, Hammond PT, Rubner MF. Controlling mammalian cell interactions on patterned polyelectrolyte multilayer surfaces. *Langmuir*. 2004; **20**: 1362-8.

122. Mendelsohn JD, Barrett CJ, Chan VV, Pal AJ, Mayes AM, Rubner MF. Fabrication of microporous thin films from polyelectrolyte multilayers. *Langmuir*. 2000; **16**: 5017-23.

123. Lubig R, Kusch P, Roper K, Zahn H. On the Mechanism of Protein Crosslinking with Glutaraldehyde. *Monatsh Chem*. 1981; **112**: 1313-23.

124. Hermanson GT. Bioconjugate Techniques. 1st ed. San Diego, CA: Academic Press; 1996.

125. Ren KF, Crouzier T, Roy C, Picart C. Polyelectrolyte multilayer films of controlled stiffness modulate myoblast cell differentiation. *Adv Funct Mater*. 2008; **18**: 1378-89.

126. Tong WJ, Gao CY, Mohwald H. Manipulating the properties of polyelectrolyte microcapsules by glutaraldehyde cross-linking. *Chem Mater*. 2005; **17**: 4610-6.

127. Moussallem MD, Olenych SG, Scott SL, Keller TCS, Schlenoff JB. Smooth Muscle Cell Phenotype Modulation and Contraction on Native and Cross-Linked Polyelectrolyte Multilayers. *Biomacromolecules*. 2009; **10**: 3062-8.

128. Lvov Y, Decher G, Sukhorukov G. Assembly of Thin-Films by Means of Successive Deposition of Alternate Layers of DNA and Poly(Allylamine). *Macromolecules*. 1993; **26**: 5396-9.

129. Brunot C, Ponsonnet L, Lagneau C, Farge P, Picart C, Grosgogeat B. Cytotoxicity of polyethyleneimine (PEI), precursor base layer of polyelectrolyte multilayer films. *Biomaterials*. 2007; **28**: 632-40.

130. Fischer D, Li YX, Ahlemeyer B, Krieglstein J, Kissel T. In vitro cytotoxicity testing of polycations: influence of polymer structure on cell viability and hemolysis. *Biomaterials*. 2003; **24**: 1121-31.

131. Choksakulnimitr S, Masuda S, Tokuda H, Takakura Y, Hashida M. In-Vitro Cytotoxicity of Macromolecules in Different Cell-Culture Systems. *J Control Release*. 1995; **34**: 233-41.

132. Stevens MM, George JH. Exploring and engineering the cell surface interface. *Science*. 2005; **310**: 1135-8.

133. Abrams GA, Schaus SS, Goodman SL, Nealey PF, Murphy CJ. Nanoscale topography of the corneal epithelial basement membrane and Descemet's membrane of the human. *Cornea*. 2000; **19**: 57-64.

134. Beuerman RW, Pedroza L. Ultrastructure of the human cornea. *Microsc Res Tech*. 1996; **33**: 320-35.

135. Griffith LG, Swartz MA. Capturing complex 3D tissue physiology in vitro. *Nat Rev Mol Cell Biol*. 2006; **7**: 211-24.

136. Hiller J, Mendelsohn JD, Rubner MF. Reversibly erasable nanoporous anti-reflection coatings from polyelectrolyte multilayers. *Nat Mater*. 2002; **1**: 59-63.

137. Hajicharalambous CS, Lichter J, Hix WT, Swierczewska M, Rubner MF, Rajagopalan P. Nano- and sub-micron porous polyelectrolyte multilayer assemblies: Biomimetic surfaces for human corneal epithelial cells. *Biomaterials*. 2009; **30**: 4029-36.

138. Kidambi S, Lee I, Chan C. Controlling primary hepatocyte adhesion and spreading on protein-free polyelectrolyte multilayer films. *J Am Chem Soc*. 2004; **126**: 16286-7.

139. Chen AA, Khetani SR, Lee S, Bhatia SN, Van Vliet KJ. Modulation of hepatocyte phenotype in vitro via chemomechanical tuning of polyelectrolyte multilayers. *Biomaterials*. 2009; **30**: 1113-20.

140. Kidambi S, Sheng L, Yarmush ML, Toner M, Lee I, Chan C. Patterned co-culture of primary hepatocytes and fibroblasts using polyelectrolyte multilayer templates. *Macromol Biosci*. 2007; **7**: 344-53.

141. Park IK, Yang J, Jeong HJ, Bom HS, Harada I, Akaike T, Kim S, Cho CS. Galactosylated chitosan as a synthetic extracellular matrix for hepatocytes attachment. *Biomaterials*. 2003; **24**: 2331-7.

142. Park IK, Kim TH, Park YH, Shin BA, Choi ES, Chowdhury EH, Akaike T, Cho CS. Galactosylated chitosan-graft-poly(ethylene glycol) as hepatocyte-targeting DNA carrier. *J Control Release*. 2001; **76**: 349-62.

143. Joddar B, Ramamurthi A. Elastogenic effects of exogenous hyaluronan oligosaccharides on vascular smooth muscle cells. *Biomaterials*. 2006; **27**: 5698-707.

144. Remuzzi A, Mantero S, Colombo M, Morigi M, Binda E, Camozzi D, Imberti B. Vascular smooth muscle cells on hyaluronic acid: Culture and mechanical characterization of an engineered vascular construct. *Tissue Eng*. 2004; **10**: 699-710.

145. Zhu N, Liggitt D, Liu Y, Debs R. Systemic Gene-Expression after Intravenous DNA Delivery into Adult Mice. *Science*. 1993; **261**: 209-11.

146. van 't Veer LJ, Dai H, van de Vijver MJ, He YD, Hart AA, Mao M, Peterse HL, van der Kooy K, Marton MJ, Witteveen AT, Schreiber GJ, Kerkhoven RM, Roberts C, Linsley PS, Bernards R, Friend SH. Gene expression profiling predicts clinical outcome of breast cancer. *Nature*. 2002; **415**: 530-6.

147. Kim Y, Lasher CD, Milford LM, Murali TM, Rajagopalan P. A comparative study of genome-wide transcriptional profiles of primary hepatocytes in collagen sandwich and monolayer cultures. *Tissue Eng Part C, Methods*. 2010; **16**: 1449-60.

148. Schena M, Shalon D, Davis RW, Brown PO. Quantitative monitoring of gene expression patterns with a complementary DNA microarray. *Science*. 1995; **270**: 467-70.

149. Schulze A, Downward J. Navigating gene expression using microarrays--a technology review. *Nat Cell Biol*. 2001; **3**: E190-5.

150. Lockhart DJ, Winzeler EA. Genomics, gene expression and DNA arrays. *Nature*. 2000; **405**: 827-36.

151. Baker TK, Carfagna MA, Gao H, Dow ER, Li Q, Searfoss GH, Ryan TP. Temporal gene expression analysis of monolayer cultured rat hepatocytes. *Chem Res Toxicol*. 2001; **14**: 1218-31.

152. Nava A, Mazza E, Furrer M, Villiger P, Reinhart WH. In vivo mechanical characterization of human liver. *Med Image Anal*. 2008; **12**: 203-16.

153. Sandrin L, Fourquet B, Hasquenoph JM, Yon S, Fournier C, Mal F, Christidis C, Ziol M, Poulet B, Kazemi F, Beaugrand M, Palau R. Transient elastography: a new noninvasive method for assessment of hepatic fibrosis. *Ultrasound Med Biol*. 2003; **29**: 1705-13.

154. Sechser A, Osorio J, Freise C, Osorio RW. Artificial liver support devices for fulminant liver failure. *Clin Liver Dis*. 2001; **5**: 415-30.

155. Corlu A, Ilyin G, Cariou S, Lamy I, Loyer P, Guguen-Guillouzo C. The coculture: a system for studying the regulation of liver differentiation/proliferation activity and its control. *Cell Biol Toxicol*. 1997; **13**: 235-42.

156. Khetani SR, Szulgit G, Del Rio JA, Barlow C, Bhatia SN. Exploring interactions between rat hepatocytes and nonparenchymal cells using gene expression profiling. *Hepatology*. 2004; **40**: 545-54.

157. Tilles AW, Baskaran H, Roy P, Yarmush ML, Toner M. Effects of oxygenation and flow on the viability and function of rat hepatocytes cocultured in a microchannel flat-plate bioreactor. *Biotechnol Bioeng*. 2001; **73**: 379-89.

158. Zaret KS. Regulatory phases of early liver development: paradigms of organogenesis. *Nat Rev Genet*. 2002; **3**: 499-512.

159. Cleaver O, Melton DA. Endothelial signaling during development. *Nat Med*. 2003; **9**: 661-8.

160. Matsumoto K, Yoshitomi H, Rossant J, Zaret KS. Liver organogenesis promoted by endothelial cells prior to vascular function. *Science*. 2001; **294**: 559-63.

161. Ross MA, Sander CM, Kleeb TB, Watkins SC, Stolz DB. Spatiotemporal expression of angiogenesis growth factor receptors during the revascularization of regenerating rat liver. *Hepatology*. 2001; **34**: 1135-48.

162. Nahmias Y, Casali M, Barbe L, Berthiaume F, Yarmush ML. Liver endothelial cells promote LDL-R expression and the uptake of HCV-like particles in primary rat and human hepatocytes. *Hepatology*. 2006; **43**: 257-65.

163. Shimizu T, Yamato M, Isoi Y, Akutsu T, Setomaru T, Abe K, Kikuchi A, Umezu M, Okano T. Fabrication of pulsatile cardiac tissue grafts using a novel 3-dimensional cell sheet manipulation technique and temperature-responsive cell culture surfaces. *Circ Res*. 2002; **90**: e40.

164. Wilson WC, Jr., Boland T. Cell and organ printing 1: protein and cell printers. *Anat Rec A Discov Mol Cell Evol Biol*. 2003; **272**: 491-6.

165. Boland T, Mironov V, Gutowska A, Roth EA, Markwald RR. Cell and organ printing 2: fusion of cell aggregates in three-dimensional gels. *Anat Rec A Discov Mol Cell Evol Biol*. 2003; **272**: 497-502.

166. Sauerbrey G. Verwendung von Schwingquarzen zur Wägung Dünner Schichten und zur Mikrowägung. *Zeitschrift für Physik A Hadrons and Nuclei*. 1959; **155**: 206-22.

167. Voinova MV, Rodahl M, Jonson M, Kasemo B. Viscoelastic acoustic response of layered polymer films at fluid-solid interfaces: Continuum mechanics approach. *Phys Scr*. 1999; **59**: 391-6.

168. de Kerchove AJ, Elimelech M. Formation of polysaccharide gel layers in the presence of Ca2+ and K+ ions: Measurements and mechanisms. *Biomacromolecules*. 2007; **8**: 113-21.

169. Munro JC, Frank CW. Polyacrylamide adsorption from aqueous solutions on gold and silver surfaces monitored by the quartz crystal microbalance. *Macromolecules*. 2004; **37**: 925-38.

170. Behnia K, Bhatia S, Jastromb N, Balis U, Sullivan S, Yarmush M, Toner M. Xenobiotic metabolism by cultured primary porcine hepatocytes. *Tissue Eng*. 2000; **6**: 467-79.

171. Khetani SR, Bhatia SN. Microscale culture of human liver cells for drug development. *Nat Biotechnol*. 2008; **26**: 120-6.

172. Liu X, LeCluyse EL, Brouwer KR, Gan LS, Lemasters JJ, Stieger B, Meier PJ, Brouwer KL. Biliary excretion in primary rat hepatocytes cultured in a collagen-sandwich configuration. *Am J Physiol*. 1999; **277**: G12-21.

173. Seternes T, Sorensen K, Smedsrod B. Scavenger endothelial cells of vertebrates: a nonperipheral leukocyte system for high-capacity elimination of waste macromolecules. *Proc Natl Acad Sci U S A*. 2002; **99**: 7594-7.

174. Hwa AJ, Fry RC, Sivaraman A, So PT, Samson LD, Stolz DB, Griffith LG. Rat liver sinusoidal endothelial cells survive without exogenous VEGF in 3D perfused co-cultures with hepatocytes. *FASEB J*. 2007; **21**: 2564-79.

175. Pa JH, Yu TL. Light scattering study of chitosan in acetic acid aqueous solutions. *Macromol Chem Phys*. 2001; **202**: 985-91.

176. Lee SB, Lee YM, Song KW, Park MH. Preparation and properties of polyelectrolyte complex sponges composed of hyaluronic acid and chitosan and their biological behaviors. *J Appl Polym Sci*. 2003; **90**: 925-32.

177. Omiecinski CJ, Remmel RP, Hosagrahara VP. Concise review of the cytochrome P450s and their roles in toxicology. *Toxicol Sci*. 1999; **48**: 151-6.

178. Thummel KE, Wilkinson GR. In vitro and in vivo drug interactions involving human CYP3A. *Annu Rev Pharmacol Toxicol*. 1998; **38**: 389-430.

179. Rendic S, DiCarlo FJ. Human cytochrome P450 enzymes: A status report summarizing their reactions, substrates, inducers, and inhibitors. *Drug Metab Rev*. 1997; **29**: 413-580.

180. Rahman A, Korzekwa KR, Grogan J, Gonzalez FJ, Harris JW. Selective Biotransformation of Taxol to 6-Alpha-Hydroxytaxol by Human Cytochrome-P450 2c8. *Cancer Res*. 1994; **54**: 5543-6.

181. Shimizu T, Yamato M, Kikuchi A, Okano T. Cell sheet engineering for myocardial tissue reconstruction. *Biomaterials*. 2003; **24**: 2309-16.

182. Yang SY, Rubner MF. Micropatterning of polymer thin films with pH-sensitive and cross-linkable hydrogen-bonded polyelectrolyte multilayers. *J Am Chem Soc*. 2002; **124**: 2100-1.

183. Lvov YM, Sukhorukov GB. Protein architecture: Assembly of ordered films by means alternated adsorption of opposite charged macromolecules. *Biol Membr*. 1997; **14**: 229-50.

184. Shimomura H, Gemici Z, Cohen RE, Rubner MF. Layer-by-Layer-Assembled High-Performance Broadband Antireflection Coatings. *ACS Appl Mater Interfaces*. 2010; **2**: 813-20.

185. Ono SS, Decher G. Preparation of ultrathin self-standing polyelectrolyte multilayer membranes at physiological conditions using pH-responsive film segments as sacrificial layers. *Nano Lett*. 2006; **6**: 592-8.

186. Swierczewska M, Hajicharalambous CS, Janorkar AV, Megeed Z, Yarmush ML, Rajagopalan P. Cellular response to nanoscale elastin-like polypeptide polyelectrolyte multilayers. *Acta Biomater*. 2008; **4**: 827-37.

187. Tryoen-Toth P, Vautier D, Haikel Y, Voegel JC, Schaaf P, Chluba J, Ogier J. Viability, adhesion, and bone phenotype of osteoblast-like cells on polyelectrolyte multilayer films. *J Biomed Mater Res*. 2002; **60**: 657-67.

188. Janorkar AV, Rajagopalan P, Yarmush ML, Megeed Z. The use of elastin-like polypeptide-polyelectrolyte complexes to control hepatocyte morphology and function in vitro. *Biomaterials*. 2008; **29**: 625-32.

189. Lichter JA, Van Vliet KJ, Rubner MF. Design of Antibacterial Surfaces and Interfaces: Polyelectrolyte Multilayers as a Multifunctional Platform. *Macromolecules*. 2009; **42**: 8573-86.

190. DeRocher JP, Mao P, Han JY, Rubner MF, Cohen RE. Layer-by-Layer Assembly of Polyelectrolytes in Nanofluidic Devices. *Macromolecules*. 2010; **43**: 2430-7.

191. Shutava TG, Balkundi SS, Vangala P, Steffan JJ, Bigelow RL, Cardelli JA, O'Neal DP, Lvov YM. Layer-by-Layer-Coated Gelatin Nanoparticles as a Vehicle for Delivery of Natural Polyphenols. *ACS Nano*. 2009; **3**: 1877-85.

192. Becker N, Oroudjev E, Mutz S, Cleveland JP, Hansma PK, Hayashi CY, Makarov DE, Hansma HG. Molecular nanosprings in spider capture-silk threads. *Nat Mater*. 2003; **2**: 278-83.

193. Choi HJ, Brooks E, Montemagno CD. Synthesis and characterization of nanoscale biomimetic polymer vesicles and polymer membranes for bioelectronic applications. *Nanotechnology*. 2005; **16**: S143-S9.

194. Jiang CY, Tsukruk VV. Freestanding nanostructures via layer-by-layer assembly. *Adv Mater*. 2006; **18**: 829-40.

195. Koktysh DS, Liang XR, Yun BG, Pastoriza-Santos I, Matts RL, Giersig M, Serra-Rodriguez C, Liz-Marzan LM, Kotov NA. Biomaterials by design: Layer-by-layer assembled ion-selective and biocompatible films of TiO2 nanoshells for neurochemical monitoring. *Adv Funct Mater*. 2002; **12**: 255-65.

196. Endo H, Kado Y, Mitsuishi M, Miyashita T. Fabrication of free-standing hybrid nanosheets organized with polymer Langmuir-Blodgett films and gold nanoparticles. *Macromolecules*. 2006; **39**: 5559-63.

197. Endo H, Mitsuishi M, Miyashita T. Free-standing ultrathin films with universal thickness from nanometer to micrometer by polymer nanosheet assembly. *J Mater Chem*. 2008; **18**: 1302-8.

198. Jiang CY, Markutsya S, Pikus Y, Tsukruk VV. Freely suspended nanocomposite membranes as highly sensitive sensors. *Nat Mater*. 2004; **3**: 721-8.

199. Mallwitz F, Laschewsky A. Direct access to stable, freestanding polymer membranes by layer-by-layer assembly of polyelectrolytes. *Adv Mater*. 2005; **17**: 1296-9.
200. Hua F, Cui TH, Lvov YM. Ultrathin cantilevers based on polymer-ceramic nanocomposite assembled through layer-by-layer adsorption. *Nano Lett*. 2004; **4**: 823-5.
201. Ferri JK, Dong WF, Miller R, Mohwald H. Elastic moduli of asymmetric ultrathin free-standing polyelectrolyte nanocomposites. *Macromolecules*. 2006; **39**: 1532-7.
202. Lutkenhaus JL, Hrabak KD, McEnnis K, Hammond PT. Elastomeric flexible free-standing hydrogen-bonded nanoscale assemblies. *J Am Chem Soc*. 2005; **127**: 17228-34.
203. Jaber JA, Schlenoff JB. Mechanical properties of reversibly cross-linked ultrathin polyelectrolyte complexes. *J Am Chem Soc*. 2006; **128**: 2940-7.
204. Zimnitsky D, Shevchenko VV, Tsukruk VV. Perforated, freely suspended layer-by-layer nanoscale membranes. *Langmuir*. 2008; **24**: 5996-6006.
205. Drury JL, Mooney DJ. Hydrogels for tissue engineering: scaffold design variables and applications. *Biomaterials*. 2003; **24**: 4337-51.
206. Nettles DL, Elder SH, Gilbert JA. Potential use of chitosan as a cell scaffold material for cartilage tissue engineering. *Tissue Eng*. 2002; **8**: 1009-16.
207. Tan W, Krishnaraj R, Desai TA. Evaluation of nanostructured composite collagen-chitosan matrices for tissue engineering. *Tissue Eng*. 2001; **7**: 203-10.
208. Jameela SR, Jayakrishnan A. Glutaraldehyde Cross-Linked Chitosan Microspheres as a Long-Acting Biodegradable Drug-Delivery Vehicle - Studies on the in-Vitro Release of Mitoxantrone and in-Vivo Degradation of Microspheres in Rat Muscle. *Biomaterials*. 1995; **16**: 769-75.
209. Pharr GM, Oliver WC, Brotzen FR. On the Generality of the Relationship among Contact Stiffness, Contact Area, and Elastic-Modulus during Indentation. *J Mater Res*. 1992; **7**: 613-7.
210. Nolte AJ, Rubner MF, Cohen RE. Determining the young's modulus of polyelectrolyte multilayer films via stress-induced mechanical buckling instabilities. *Macromolecules*. 2005; **38**: 5367-70.
211. Fischer-Cripps AC. Nanoindentation. New York: Springer; 2002.

212. Pavoor PV, Bellare A, Strom A, Yang DH, Cohen RE. Mechanical characterization of polyelectrolyte multilayers using quasi-static nanoindentation. *Macromolecules*. 2004; **37**: 4865-71.

213. Vertlib V, Dietiker M, Plotze M, Yezek L, Spolenak R, Puzrin AM. Fast assembly of bio-inspired nanocomposite films. *J Mater Res*. 2008; **23**: 1026-35.

214. Monteiro OAC, Airoldi C. Some studies of crosslinking chitosan-glutaraldehyde interaction in a homogeneous system. *Int J Biol Macromol*. 1999; **26**: 119-28.

215. Sievers TK, Vergin A, Mohwald H, Kurth DG. Thin films of cross-linked metallo-supramolecular coordination polyelectrolytes. *Langmuir*. 2007; **23**: 12179-84.

216. Lutkenhaus JL, McEnnis K, Hammond PT. Nano- and microporous layer-by-layer assemblies containing linear poly(ethylenimine) and poly(acrylic acid). *Macromolecules*. 2008; **41**: 6047-54.

217. Dalby MJ, Riehle MO, Johnstone HJH, Affrossman S, Curtis ASG. Polymer-demixed nanotopography: Control of fibroblast spreading and proliferation. *Tissue Eng*. 2002; **8**: 1099-108.

218. Dalby MJ, Riehle MO, Sutherland DS, Agheli H, Curtis ASG. Changes in fibroblast morphology in response to nano-columns produced by colloidal lithography. *Biomaterials*. 2004; **25**: 5415-22.

219. Griffith M, Osborne R, Munger R, Xiong XJ, Doillon CJ, Laycock NLC, Hakim M, Song Y, Watsky MA. Functional human corneal equivalents constructed from cell lines. *Science*. 1999; **286**: 2169-72.

220. Li Q, Quinn JF, Caruso F. Nanoporous polymer thin films via polyelectrolyte templating. *Adv Mater*. 2005; **17**: 2058-62.

221. Alkrad JA, Mrestani Y, Stroehl D, Wartewig S, Neubert R. Characterization of enzymatically digested hyaluronic acid using NMR, Raman, IR, and UV-Vis spectroscopies. *J Pharm Biomed Anal*. 2003; **31**: 545-50.

222. Hyung W, Ko H, Park J, Lim E, Park SB, Park YJ, Yoon HG, Suh JS, Haam S, Huh YM. Novel hyaluronic acid (HA) coated drug carriers (HCDCs) for human breast cancer treatment. *Biotechnol Bioeng*. 2008; **99**: 442-54.

223. Rajagopalan P, McCarthy TJ. Two-step surface modification of chemically resistant polymers: Blend formation and subsequent chemistry. *Macromolecules*. 1998; **31**: 4791-7.

224. Sellaro TL, Ravindra AK, Stolz DB, Badylak SF. Maintenance of hepatic sinusoidal endothelial cell phenotype in vitro using organ-specific extracellular matrix scaffolds. *Tissue Eng*. 2007; **13**: 2301-10.

225. Wisse E, De Zanger RB, Charels K, Van Der Smissen P, McCuskey RS. The liver sieve: considerations concerning the structure and function of endothelial fenestrae, the sinusoidal wall and the space of Disse. *Hepatology*. 1985; **5**: 683-92.

226. Braet F, Wisse E. Structural and functional aspects of liver sinusoidal endothelial cell fenestrae: a review. *Comparative hepatology*. 2002; **1**: 1-17.

227. Detzel CJ, Kim Y, Rajagopalan P. Engineered Three-Dimensional Liver Mimics Recapitulate Critical Rat-Specific Bile Acid Pathways. *Tissue Eng Part A*. 2010.

228. Tokairin T, Nishikawa Y, Doi Y, Watanabe H, Yoshioka T, Su M, Omori Y, Enomoto K. A highly specific isolation of rat sinusoidal endothelial cells by the immunomagnetic bead method using SE-1 monoclonal antibody. *J Hepatol*. 2002; **36**: 725-33.

229. Miller CJ. simpleaffy: Very simple high level analysis of Affymetrix data.

230. Wu J. IR, MacDonald J., Gentry J. gcrma: Background Adjustment Using Sequence Information.

231. Mootha VK, Lindgren CM, Eriksson KF, Subramanian A, Sihag S, Lehar J, Puigserver P, Carlsson E, Ridderstrale M, Laurila E, Houstis N, Daly MJ, Patterson N, Mesirov JP, Golub TR, Tamayo P, Spiegelman B, Lander ES, Hirschhorn JN, Altshuler D, Groop LC. PGC-1alpha-responsive genes involved in oxidative phosphorylation are coordinately downregulated in human diabetes. *Nat Genet*. 2003; **34**: 267-73.

232. Subramanian A, Tamayo P, Mootha VK, Mukherjee S, Ebert BL, Gillette MA, Paulovich A, Pomeroy SL, Golub TR, Lander ES, Mesirov JP. Gene set enrichment analysis: a knowledge-based approach for interpreting genome-wide expression profiles. *Proc Natl Acad Sci U S A*. 2005; **102**: 15545-50.

233. Ashburner M, Ball CA, Blake JA, Botstein D, Butler H, Cherry JM, Davis AP, Dolinski K, Dwight SS, Eppig JT, Harris MA, Hill DP, Issel-Tarver L, Kasarskis A,

Lewis S, Matese JC, Richardson JE, Ringwald M, Rubin GM, Sherlock G. Gene ontology: tool for the unification of biology. The Gene Ontology Consortium. *Nat Genet*. 2000; **25**: 25-9.

234. Kandasamy K, Mohan SS, Raju R, Keerthikumar S, Kumar GS, Venugopal AK, Telikicherla D, Navarro JD, Mathivanan S, Pecquet C, Gollapudi SK, Tattikota SG, Mohan S, Padhukasahasram H, Subbannayya Y, Goel R, Jacob HK, Zhong J, Sekhar R, Nanjappa V, Balakrishnan L, Subbaiah R, Ramachandra YL, Rahiman BA, Prasad TS, Lin JX, Houtman JC, Desiderio S, Renauld JC, Constantinescu SN, Ohara O, Hirano T, Kubo M, Singh S, Khatri P, Draghici S, Bader GD, Sander C, Leonard WJ, Pandey A. NetPath: a public resource of curated signal transduction pathways. *Genome Biol*. 2010; **11**: R3.

235. Benjamini Y, Hochberg Y. Controlling the false discovery rate: a practical and powerful approach to multiple testing. *Journal of the Royal Statistical Society, Series B (Methodological)*. 1995; **57**: 289-300.

236. Berriz GF, Beaver JE, Cenik C, Tasan M, Roth FP. Next generation software for functional trend analysis. *Bioinformatics*. 2009; **25**: 3043-4.

237. Barbe E, Damoiseaux JG, Dopp EA, Dijkstra CD. Characterization and expression of the antigen present on resident rat macrophages recognized by monoclonal antibody ED2. *Immunobiology*. 1990; **182**: 88-99.

238. Dijkstra CD, Dopp EA, Joling P, Kraal G. The heterogeneity of mononuclear phagocytes in lymphoid organs: distinct macrophage subpopulations in the rat recognized by monoclonal antibodies ED1, ED2 and ED3. *Immunology*. 1985; **54**: 589-99.

239. Rajagopalan P, Berthiaume F, Tilles AW, Toner M, Yarmush ML. Selective enhancement of cytochrome p-450 activity in rat hepatocytes by in vitro heat shock. *Tissue Eng*. 2005; **11**: 1527-34.

240. Pan JM, Xiang Q, Ball S. Use of a novel real-time quantitative reverse transcription-polymerase chain reaction method to study the effects of cytokines on cytochrome P450 mRNA expression in mouse liver. *Drug Metab Dispos*. 2000; **28**: 709-13.

241. Mehal WZ, Azzaroli F, Crispe IN. Immunology of the healthy liver: Old questions and new insights. *Gastroenterology*. 2001; **120**: 250-60.

242. Chojkier M, Lyche KD, Filip M. Increased production of collagen in vivo by hepatocytes and nonparenchymal cells in rats with carbon tetrachloride-induced hepatic fibrosis. *Hepatology*. 1988; **8**: 808-14.

243. McClain DA, Edelman GM. A neural cell adhesion molecule from human brain. *Proc Natl Acad Sci U S A*. 1982; **79**: 6380-4.

244. Walmod PS, Kolkova K, Berezin V, Bock E. Zippers make signals: NCAM-mediated molecular interactions and signal transduction. *Neurochem Res*. 2004; **29**: 2015-35.

245. Van Den Heuvel MC, Slooff MJ, Visser L, Muller M, De Jong KP, Poppema S, Gouw AS. Expression of anti-OV6 antibody and anti-N-CAM antibody along the biliary line of normal and diseased human livers. *Hepatology*. 2001; **33**: 1387-93.

246. Fabris L, Strazzabosco M, Crosby HA, Ballardini G, Hubscher SG, Kelly DA, Neuberger JM, Strain AJ, Joplin R. Characterization and isolation of ductular cells coexpressing neural cell adhesion molecule and Bcl-2 from primary cholangiopathies and ductal plate malformations. *Am J Pathol*. 2000; **156**: 1599-612.

247. Libbrecht L, Cassiman D, Desmet V, Roskams T. Expression of neural cell adhesion molecule in human liver development and in congenital and acquired liver diseases. *Histochem Cell Biol*. 2001; **116**: 233-9.

248. Khetani SR, Chen AA, Ranscht B, Bhatia SN. T-cadherin modulates hepatocyte functions in vitro. *FASEB J*. 2008; **22**: 3768-75.

249. Adachi Y, Takeuchi T, Sonobe H, Ohtsuki Y. An adiponectin receptor, T-cadherin, was selectively expressed in intratumoral capillary endothelial cells in hepatocellular carcinoma: possible cross talk between T-cadherin and FGF-2 pathways. *Virchows Arch*. 2006; **448**: 311-8.

250. Breitfeld J, Stumvoll M, Kovacs P. Genetics of adiponectin. *Biochimie*.

251. Zeng G, Awan F, Otruba W, Muller P, Apte U, Tan X, Gandhi C, Demetris AJ, Monga SP. Wnt'er in liver: expression of Wnt and frizzled genes in mouse. *Hepatology*. 2007; **45**: 195-204.

252. Xia Y, Babitt JL, Sidis Y, Chung RT, Lin HY. Hemojuvelin regulates hepcidin expression via a selective subset of BMP ligands and receptors independently of neogenin. *Blood*. 2008; **111**: 5195-204.

253. Langenfeld EM, Langenfeld J. Bone morphogenetic protein-2 stimulates angiogenesis in developing tumors. *Mol Cancer Res*. 2004; **2**: 141-9.

254. Suzuki Y, Montagne K, Nishihara A, Watabe T, Miyazono K. BMPs promote proliferation and migration of endothelial cells via stimulation of VEGF-A/VEGFR2 and angiopoietin-1/Tie2 signalling. *J Biochem*. 2008; **143**: 199-206.

255. Masckauchan TN, Agalliu D, Vorontchikhina M, Ahn A, Parmalee NL, Li CM, Khoo A, Tycko B, Brown AM, Kitajewski J. Wnt5a signaling induces proliferation and survival of endothelial cells in vitro and expression of MMP-1 and Tie-2. *Mol Biol Cell*. 2006; **17**: 5163-72.